Title
Expanding the Atomistic Study of the Optical and Electronic Properties of Nanomaterials

Author
Weinberg, Daniel

Publication Date
2023

Peer reviewed|Thesis/dissertation

Expanding the Atomistic Study of the Optical and Electronic Properties of Nanomaterials

by

Daniel Weinberg

A dissertation submitted in partial satisfaction of the

requirements for the degree of

Doctor of Philosophy

in

Chemistry

in the

Graduate Division

of the

University of California, Berkeley

Committee in charge:

Professor Eran Rabani, Chair
Professor David Limmer
Professor Jeffrey Neaton

Summer 2023

Expanding the Atomistic Study of the Optical and Electronic Properties of Nanomaterials

Abstract

Expanding the Atomistic Study of the Optical and Electronic Properties of Nanomaterials

by

Daniel Weinberg

Doctor of Philosophy in Chemistry

University of California, Berkeley

Professor Eran Rabani, Chair

The optical and electronic properties of semiconductor nanomaterials have long attracted significant interest due to the strong absorption and tunable spectra caused by quantum confinement. These materials have potential applications ranging from solar energy conversion and lighting to single photon sources and quantum computing. However, to realize any of these applications the role of the atomistic detail of these materials cannot be ignored. Understanding role of defects, traps, and structural distortion on the excited states of these materials remains a great challenge for modern computational science. Semiemperical pseudopotential models represent the leading way to understand the complexity of nanoscale systems in atomistic detail. In this dissertation we expand the applicability of these models to new materials where additional effects, like strong spin-orbit coupling must be considered. We also use these methods to help examine the dynamics of excited states in these nanomaterials, revealing the crucial roles of defects, distortions, and traps.

We develop a formulation of the semiempirical pseudopotential method that includes the effects of spin-orbit coupling and other nonlocal terms in the potential. By using a separable form of these non-local terms we maintain a favorable computational scaling and thus keep the ability to investigate nanomaterials of experimentally relevant sizes. We apply this method to lead halide perovskite nanocrystals (NCs), promising materials for solar energy conversion that are known for their strong spin-orbit coupling. The atomistic study of these systems allows for an understanding of how distortion of the NC structure impacted the exciton fine structure, determining that contrary to some suggestions the ground state exciton is a dark state.

The results of atomistic electronic structure methods also aid in developing kinetic models of excited state species in various nanomaterials. The dynamics of the transfer of holes from multi-excitonic II-VI NCs is explored as a competition between transfer, trapping, and non-radiative Auger recombination (AR). Pseudopotential calculations provide crucial insight in the AR rates and how those are impacted by the presence of trapped species. A similar

kinetic model describing carrier recombination in few-layer black phosphorous is informed by density functional theory calculations of surface oxygen defects.

This dissertation shows both the expansion of the semiemperical pseudopotential method and the application of the method to inform studies of material properties and design principles. The combination of theoretical development and experimental collaboration shows the utility of these models to solve practical problems of broad scientific import. By expanding the applicability of these methods to new materials, these detail atomistic calculations can now be applied to even more experimentally relevant systems.

To Martha and Andy and Matthew;
I couldn't ask for a more wonderful family.

They enter the new world naked,
cold, uncertain of all
save that they enter. All about them
the cold, familiar wind—

Now the grass, tomorrow
the stiff curl of wildcarrot leaf
One by one objects are defined—
It quickens: clarity, outline of leaf

But now the stark dignity of
entrance—Still, the profound change
has come upon them: rooted, they
grip down and begin to awaken

—William Carlos Williams, *Spring and All*

Contents

Acknowledgments

I would like to take a moment to acknowledge all the people without whom the last four years would have been impossible. The support and community I have received throughout my scientific journey and here at Berkeley has been immense and played a crucial role in making this work a reality.

First I would like to thank Eran Rabani for his advice and mentorship. Thank you for being such a source of scientific inspiration; you have taught me so much about chemistry, research, and how to be a scientist. You have shown me how ask deep and insightful questions and then prepare and present scientific answers to them. I am so grateful to have been part of your group and I hope we can continue to build our scientific relationship as I move on from Berkeley.

The entirety of the Rabani group has been such an incredible source of support, collaboration, and fun. Thank you for welcoming me to Berkeley and then keeping me sane through the heart of the pandemic lockdowns with groups zoom lunches. Thank you to Dipti Jasrasaria for being an amazing mentor, short time office mate, traveling companion, and friend. You are an inspiration to me and I look forward to watching your continued success. Thank you to Bokang Hou for your constant advice and limitless patience to help me talk through the problems, from the most inane to the deeply impactful, as well as your great kindness and humor. And thanks for keeping me from killing our tiny office succulent. It is in better hands now! Thank you Tommy Lin for your engaging scientific discussions and great energy in organizing the group actives that helped make this group such a wonderful place to work. Thank you to Leopoldo Mejia for insightful coffee chats and unrivaled perspective into our field. Thank you to Daniel Chabeda and Kaiyue Peng for the privilege of helping shape your paths as scientists. Thank you to Matt O'Rourke for taking on the continuations of my project; I wish you luck and great success! A huge thanks to all the other Rabani group members who paved the way before me: John Philbin, Paul Wrona, Lyron Kidon, Ming Chen, Alex Lee, and many others. Thank you all so much for providing a environment where scientific work could truly develop and thrive among great friends and colleagues.

Beyond the Rabani group, I have felt the support and encouragement of the entire Pitzer center. In particular, thank you to the advice, teaching, and mentorship of David Limmer and Martin Head-Gordon from my first year classes through my quals, and on to my dissertation. Thanks as well to the Pitzer center lunch revolving cast including Amr Dodin, Sam Oakes-Leaf, Aditya Singh, Michelle Anderson, Songela Chen, Rohit Rana, and many others. These wide ranging conversations may have been the best part of many of my days and I will miss them greatly.

I have also had the great privilege of working with brilliant and talented scientific collaborators. Thank you to Chang Yan, Michael Enright, Shiekh Uddin, Naioki Higashitarumizu, Yoonjae Park, Alex Oddo, and all the rest for allowing me to do science with you.

I would also like to thank the broader community that has surrounded me here at Berkeley. Thank you to Diego, Orion, Hannah, the D&D crew, and all the other rats and hoodlums who have infinitely brightened my time here. I would also like to thank all the organizers

and members of UAW 2865 and UAW 5810 that helped us towards realizing our vision of unionized research under fair contracts. Particular thanks to the Chemistry OC for providing such an amazing community to work and organize with. I look forward to supporting your future endeavors from wherever I land.

Finally, thank you to my family, Martha, Andy, and Matthew. You have been so supportive though the ups and downs of grad school, and your constant love and encouragement has kept me going through all of it. I love you so much and cannot wait to celebrate together soon!

Chapter 1

Introduction

Semiconductor nanocrystals (NCs) provide a diverse playground within which to investigate the behavior of electronic excitations with a wide range of electronic densities of states and fundamental dynamic processes. Quantum confinement effects cause NCs to have discrete spectra at low excitation energies, like those in atoms and molecules, while at higher excitation energies they more resemble bulk materials with increasingly high densities of states [1–7]. The structure of NCs also derive from the bulk limit, but at the surface can be significantly modified by the termination of the crystal lattice. Understanding the intertwined effects of NC size, shape, structure and composition on the nature and degeneracy of electronic states has been a topic of extensively study [2, 8–15].

1.1 Effective Mass Models

Developing a theoretical description of the electronic excitations in semiconductor NCs presents a series of challenges. NCs contain orders of magnitude more atoms and valence electrons than the molecules that conventional quantum chemistry techniques have been perfected on. This prohibits the application of these techniques to all but the very smallest NCs. More progress has been made starting from the other limit: the bulk material. Continuum effective mass-style models had great early success describing quantum confinement and dielectric screening as a function of NC size [8, 16]. When expanded beyond the qualitative single-band effective mass models, sophisticated multi-band models have provided quantitative descriptions of exciton fine structure and splittings as a function of NC size, shape and composition [12, 17–19]. Further inclusion of many-body exchange interactions within excitons allowed for the accurate description of optically forbidden dark excitons and explained the non-monotonic temperature dependence of radiative lifetimes in NCs [20–23].

The qualitative picture offered by the single band models begins by assuming a parabolic dispersion of the bands near the band gap. This implies that the electron and hole quasiparticles can be treated as free particles with a renormalized effective mass related to the band

curvature by:

$$m^*_{e/h} = \frac{1}{\hbar^2}\left(\frac{\partial^2\epsilon(k)}{\partial k^2}\right)^{-1}, \tag{1.1}$$

where $\epsilon(k)$ refers to the valence or conduction band energies for the hole or electron masses respectively. The effect of confinement can then be treated as the imposition of potential barriers around these particles with the appropriate size and geometry [8, 12, 24]. For a spherical particle of radius a with an infinite potential barrier, the electron and hole confinement energies may be approximated as:

$$E^{e/h}_{nl} = \frac{\hbar^2\phi^2_{nl}}{2\pi^2 m^*_{e/h}a^2}, \tag{1.2}$$

where ϕ_{nl} is the nth zero of the spherical Bessel function of order l (i.e. $j_l(\phi_{nl}) = 0$). For a cuboidal particle with dimensions $a_{x/y/z}$ these energies can be approximated as:

$$E^{e/h}_{n_x n_y n_z} = \frac{\hbar^2}{2\pi^2 m^*_{e/h}}\left(\frac{n_x^2}{a_x^2} + \frac{n_y^2}{a_y^2} + \frac{n_z^2}{a_z^2}\right). \tag{1.3}$$

Both of these equations clearly show the inverse quadratic size dependence of these energy levels with smaller particles showing much higher confinement energies. Within an independent particle approximation, the energy for generating an electron and a hole in these confined systems is then the sum of the bulk band gap and the two confinement energies. Thus at the large size limit the bulk material properties are recovered, but for small particles confinement will result in a strong size dependence in the excitation energies of these materials.

To truly begin to grasp the optical properties of these systems we must move beyond the independent electron and hole energy levels which fail to capture the significant effect of the electron-hole Coulomb attraction. This interactions binds the electrons and holes into excitons, and lowers the energy of excitation. This Coulomb attraction is especially important in these systems as the electron and holes are both confined to the same nanoscale region. The energy of this interaction rises as $1/a$, slower than the energy of confinement, resulting in a crossover behavior of competing effects as a function of size [8, 25]. The relevant length scale for this competition is the exciton Bohr radius,

$$a_B = \frac{\hbar^2\epsilon_r}{\mu e^2}, \tag{1.4}$$

where ϵ_r is the relative permittivity of the material and $\mu = \frac{m^*_e m^*_h}{m^*_e + m^*_h}$ is the exciton reduced mass [12]. For sizes much greater than the exciton radius, known as the weak confinement regime, the confinement energy is smaller than the exciton binding energy and thus the exciton center of mass is confined. For sizes well below the exciton radius, what is known as the strong confinement regime, the confinement of the individual electron and hole states

is stronger than their attractions. Optical transitions in this regime look like transitions between individual hole and electron levels with the energy only slightly modified by the Coulomb attraction. Between these two regimes is the intermediate confinement regime where the intertwined effects of confinement and exciton binding are less clear cut. In some cases, if the electron and hole effective masses are mismatched, the heavier quasiparticle will feel only the average potential of the lighter and faster particles, localizing this heavy particle to the center of the nanocrystal [12].

These considerations within a single band approximation are sufficient for a qualitative picture, but to make quantitative contact with experimental results the theory must incorporate the details of the band structure beyond just the effective masses. Real band structures have band degeneracies and couplings that complicate the parabolic approximation. To move beyond this, various multi-band effective mass models have been constructed [12]. These models vary in what bands and inter-band couplings are considered most important based on the material parameters. For the zinc blende materials, the degeneracy of the valence band requires at least considering the coupling of the light hole and heavy hole bands. The spin split-off band can also be included to better describe the excited hole states [12]. For wide gap materials, the coupling of the valence and conduction bands can be neglected, however in materials with very small gaps (such as InAs and InSb) the coupling of the valence and conduction bands must also be considered [26]. These multi-band models write the quasiparticle wave functions as a linear combination of the bulk Bloch functions u_n of the relevant bands n, each modulated by envelope function $f_n(r)$:

$$\psi_i(r) = \sum_n f_n^i(r) u_n \,. \tag{1.5}$$

The Bloch functions are unit-cell periodic functions, and the couplings between them can be calculated from the bulk and used to create the interband coupling Hamiltonian [26]. For spherical dots, the total angular momentum of the quasi-particles is a good quantum number and thus the angular and radial parts of the envelope functions can be separated and the angular parts found exactly. The inter-band coupling Hamiltonian then leads to a series of coupled differential equations solving for the radial parts of the envelope functions and the energies of the corresponding states [12]. The results of these models have shown quantitative agreement with the size dependence of key absorption features in diverse quantum dot systems [12]. Further consideration of excitonic effects has allowed for the study of the exciton fine structure including optically forbidden dark excitons and explained the non-monotonic temperature dependence of radiative lifetimes in NCs [20–23, 27].

1.2 Pseudopotential Models

Despite these developments, the effective mass models remain inextricably tied to the bulk material properties which keeps them blind to any atomistic detail that may be important

to the NCs properties, particularly for strongly confined NCs. To better describe the complications of real NC structures, semiempirical pseudopotential models, popularized in the 1970s and 1980s to describe the electronic and optical properties of bulk semiconductors and surfaces [28], were employed and further developed to study excitons in a variety of semiconductor NCs [10, 29–31]. These models demonstrated remarkable success in postdicting and predicting the exciton fine structure [22, 32] as well as the roles of defects [33, 34], stress, and strain on the electronic structure [35, 36].

The application of this atomistic model to these NC systems allowed for investigation of several effects the effective mass models were unable to fully consider, including the effect of surface structure and orientation in NCs [10, 37]. This allowed for the identification of significant facet dependence in the rate of radiative recombination in Si NCs [10], and additional facet dependence of wave function symmetry and allowed transitions in InAs/GaAs pyramidal NCs [37]. Because the NCs represent finite systems, the pseudopotential model required adaptation from the initial bulk material formulation [10]. In the bulk, the reciprocal space pseudopotential $V(\boldsymbol{Q})$ need only be defined at values of $\boldsymbol{Q}$ that correspond to the bulk reciprocal lattice. However, to apply this to a finite system the pseudopotential must be given a continuous form as the breaking of translation symmetry removes the Bragg condition on the scattered waves. To obtain these continuous pseudopotentials, a functional form is chosen and then fit to reproduce either the discrete reciprocal space potential [38], key band parameters [10], or entire bulk band structures [31].

These theories involved some level of empiricism from simply fitting the pseudopotentials to recover bulk band quantities rather than deriving the potentials from first principles. Additional connections to *ab initio* theory were made by deriving the pseudopotentials from the self-consistently determined screened potential from the local density approximation (LDA) of the bulk material [39]. By performing calculations on an ensemble of bulk crystal structures and then averaging over the resulting potentials, a transferable, structurally averaged, and spherically symmetric potential could be obtained that still reproduced the LDA results with high fidelity [39]. This potential could then be tweaked slightly to bring the the excitation energies into line with experimental results. This process amounted to only a slight perturbation and could be done while maintaining near unity wavefunction overlap with the LDA wavefunctions [39]. Additional nonlocal terms of the pseudopotentials and spin-orbit coupling could also be incorporated by simply taking the usual nonlocal parts of the LDA pseudopotentials unmodified [30, 40].

These methods could be directly compared to the effective mass methods, and revealed a series of discrepancies. In spherical CdSe NCs, the pseudopotential method found a significantly higher density of hole states with energies more than 0.5 eV below the band edge than was predicted by the effective mass models [41]. The approximation of parabolic bands in the effective mass model was implicated in these missing states. At higher excitation energies the relevant k vectors shift away from the band extrema and the parabolic expansion no longer holds. Additional discrepancies were revealed by projecting the wavefunctions of the pseudopotential model into the effective mass-style form similar to Equation 1.5. While the effective mass model for spherical particles preserves rotational symmetry, the atomistic

nature of the pseudopotential model means that this symmetry does not hold. Thus there is considerable breaking of symmetries in the pseudopotential model that the effective mass model forbids, which has significant implications for which optical transitions are allowed and disallowed [41, 42]. To further understand the impact of the approximations of the effective mass models, the effective mass model parameters could be extracted from the bulk band structures produced by the pseudopotential model [41, 43, 44]. This allowed for a direct comparison of the two theories and their underlying assumptions. Generally the effective mass models overestimated the confinement energies in NCs and in narrow band gap materials like InAs the contribution from other band extrema to NC states was not described correctly [43].

In this dissertation, we present our work expanding upon and applying the pseudopotential model to a wide variety material systems, including systems not previously studied using these models. In the recent years, experimental development has shifted to explore new quantum dot materials. Of particular interest are the lead halide perovskite materials, due to their remarkable defect tolerance, size tunability, and strong and narrow emission [45–47]. They have attracted considerable interest for the development of LED technology [45], and as potential quantum light sources [48–51]. Describing these perovskite materials presents additional challenges not faced in the modeling of traditional II-VI and III-V semiconductor NCs. In lead halide perovskites, the bands near the band gap are impacted by strong spin-orbit coupling. This requires incorporating the nonlocal effects of this interaction into the pseudopotential model. Furthermore, the structure of perovskite materials is extremely flexible and can undergo structural phase transitions [52, 53], requiring the model to go beyond simply considering strain effects as had been done previously [35, 36, 54].

In Chapter 2 we describe the atomistic approach we have adopted to calculate quasiparticle excitations and neutral excitations in semiconductor NCs. First principles approaches, such as time-dependent density functional theory (DFT) [55–57] or many-body perturbation approximations [58], are limited to describing excitons in relatively small clusters, typically those with fewer than 100 atoms, due to their steep computational scaling [59, 60]. To make meaningful contact with experimental results on NCs that contain thousands of atoms and tens of thousands of electrons, we rely on the semiempirical pseudopotential model [10, 30, 31, 42] to describe quasiparticle excitations. We use a converged real-space grid method to represent the single-particle states combined with the filter diagonalization method [61, 62] to compute the single-particle states near the band edge and at higher excitation energies. We then use a subset of converged quasiparticle eigenstates to solve the Bethe-Salpeter equation [63] within the static screening approximation to account for electron-hole correlations in neutral optical excitations [64]. We also provide validation of the approach for the quasiparticle and optical gaps and the exciton binding energies for II-VI and III-V semiconductor NCs in both the strongly ($R < a_{\mathrm{B}}$) and weakly ($R > a_{\mathrm{B}}$) confined regimes.

In the second half of Chapter 2 we discuss the incorporation of spin-orbit coupling and other non-local terms into the pseudopotential model. We discuss the derivation of the appropriate terms in the Hamiltonian and how to implement them efficiently both in the calculation of bulk band structures and confined states in NCs. We show how the imple-

mentation of a separable form for the nonlocal potential can improve both the accuracy and efficiency of these calculations.

In order to apply these pseudopotential models to new materials they must be parameterized to recreate bulk band structures. This fitting process is discussed in Chapter 3. In this chapter we discuss the practical considerations involved in fitting pseudopotentials, a highly non-linear fitting process. Various strategies for overcoming local minima are discussed and the details of the fitting process for two example systems are reviewed. The process of fitting pseudopotentials for InAs/InP core-shell quantum dots is discussed, where a the same In pseudopotential was required to describe both materials. On the other hand the fitting process for $CsPbI_3$ perovskite required different pseudopotentials for I and Pb that depended on the structural phase of the material. These two examples highlight the extent to which these pseudopotential models require a specific understanding of the important properties of the material under study.

We then apply these developments in Chapter 4 to resolve a important point of contention regarding the ordering of bright and dark states in perovskite NCs. Here, the atomistic nature of the pseudopotential method allowed for the effects of nanoscale lattice distortion in these NCs to be fully incorporated into the electronic structure calculations. We find that some effective mass-type models [65, 66] had overestimated the role of the Rashba effect and that the ground state exciton is a dark state [67, 68]. We further examine the effects of lattice distortion and NC shape anisotropy on the level splitting among the bright states of these NCs.

The utility of the pseudopotential method goes beyond simply calculating spectra. As shown in Chapter 5 this method also gives access to the dynamics of excited state species. In this chapter the dynamics of the transfer of holes from multi-excitonic NCs is explored as a competition between transfer, trapping, and non-radiative Auger recombination (AR). Pseudopotential calculations provided crucial insight in the AR rates and how those are impacted by the presence of trapped species. The concept of trapping is explored from a different angle in Chapter 6 where density functional theory is employed to study the resilience of few-layer black phosphorous to surface oxygen defects from an *ab initio* perspective. In both of these chapters the electronic calculations are used to inform kinetic master equation models of carrier dynamics in these nanomaterials.

Chapter 2

Expanding the Pseudopotential Hamiltonian

Applications of the semiempirical pseudopotential method have often ignored nonlocal effects such as spin-orbit coupling, however these effects can be incorporated into this approach [30, 35, 69, 70]. The method to do so will be the focus of this section. Sec. 2.1 gives an overview of the pseudopotential method and where nonlocal affects may arise. Sec. 2.2 describes the incorporation of these effects in the calculation of bulk band structures. Sec. 2.3 describes the incorporation of these effects into calculations of finite systems using real-space grid methods. The parts of this chapter are adapted with permission from Jasrasaria, D.; Weinberg, D.; Philbin, J. P.; Rabani, E. Simulations of nonradiative processes in semiconductor nanocrystals. *J. Chem. Phys.* **2022**, *157*, 020901.

2.1 Introduction to the Pseudopotential Method

The diversity of dynamic processes in semiconductor nanocrystals (NCs) requires a comprehensive model that captures a wide spectrum of physics. The finite size of NCs modifies the electronic structure relative to the bulk material—the continuous conduction and valence bands of the bulk are split into discrete states for finite crystals. This quantum confinement of carriers gives rise to NCs' hallmark size-dependent optical properties. To properly describe these optical properties, a model must go beyond the ground electronic state and describe the excited electronic states, as well. While these excited states are generally well understood in bulk semiconductors, quantum confinement complicates our understanding by significantly enhancing the electron-hole interactions in nanoscale systems [42]. The small size of NCs compared to the exciton Bohr radius forces the electron and hole closer to each other than they would be in bulk, increasing the strength of their Coulomb interactions. Additionally, dielectric screening is reduced at the nanoscale as quantum confinement widens the band gap and increases the energy required to polarize the medium. This effect leads to a size-dependent reduction in screening, further contributing to size-dependent modifica-

tions of excited states in NCs. These enhanced interactions must be properly considered in order to describe the correlations between electrons and holes and achieve agreement with experimental measurements.

Experimentally relevant NCs are highly crystalline, and in the interior of the structure they closely resemble the corresponding bulk materials. The atomic configuration aligns closely with the bulk crystalline lattice across the majority of unit cells, suggesting that a description based on bulk bands would be a valid starting point. However, NCs possess additional features that distinguish them from bulk. The NC surface truncates the lattice symmetry, which gives rise to quantum confinement. Core-shell structures also form a nanoscale heterojunction that can introduce significant amounts of strain into the crystal structure [71, 72]. Both these internal interfaces and surfaces cause deformations from crystallinity on the scale of individual atoms, so accurate modeling of NCs must include this atomistic detail. For example, localized trap states at surfaces or interfaces due to atomic defects are ubiquitous in experimental studies of NCs, where they are observed to rapidly quench photoluminescence and result in significantly lower quantum yields [73, 74]. An atomistic description of the NC structure allows for the introduction of site-specific defects or alloying to understand their roles in trap formation and to determine the dynamics of trapping in NC systems [34, 75]. Finally, in order to make meaningful contact with experimental measurements on NCs that contain thousands of atoms and tens of thousands of electrons, computational evaluation of the model must scale moderately with system size in comparison to first principles approaches. Because NC systems have important size dependent properties, such as optical gaps [76], radiative lifetimes, and Auger recombination (AR) lifetimes [77], and the scaling of these properties with system size is often an important question, the ability to access experimentally relevant sizes with volumes ranging across multiple orders of magnitude is crucial.

These considerations have informed our development of the semiempirical pseudopotential model as a sufficiently detailed description of NCs that can also tackle calculations of experimentally relevant systems. For example, a CdSe quantum dot only 4 nm in diameter has over 1000 atoms and 4000 valence electrons, so the conventional workhorses of quantum chemistry, such as density functional theory (DFT) and related methods for excited states, despite making significant progress [56, 57], are still far from being able to tackle this problem. On the other hand, continuum models based on the effective mass approximation have produced successful predictions for simple, linear spectroscopic observables [12] but are unable to capture many of the more complicated dynamic processes that determine the timescales of processes, such as nonradiative exciton relaxation and AR. Furthermore, these continuum models are, by nature, blind to atomistic detail, such as defects, strain at heterostructure interfaces, and facet-dependent properties [78, 79].

Our approach is based on the semiempirical pseudopotential method [10, 31, 42], which was first developed to characterize the band structures of simple bulk materials [28] and was later extended to describe the role of surfaces [80] and confinement [10, 29]. The basic assumption made within this method is that the bulk band structure can be described by a

simple, non-interacting model Hamiltonian:

$$\hat{h}_{\mathrm{qp}} = \hat{t} + \hat{v}(\boldsymbol{r}) = \hat{t} + \sum_{\alpha} \hat{v}_{\alpha}(\boldsymbol{R}_{\alpha})\,, \tag{2.1}$$

where $\hat{t}$ is the single-particle kinetic energy operator, and $\hat{v}$ is the pseudopotential, which is given by a sum over all atoms, α, of a atomic pseudopotential, $\hat{v}_{\alpha}(\boldsymbol{R}_{\alpha})$, which may be entirely local or include nonlocal terms and is centered at $\boldsymbol{R}_{\alpha}$, the position atom α. The parameters used to describe the pseudopotential of each atom are obtained by fitting the reciprocal-space pseudopotentials to the bulk band structure obtained either from experimental measurements or high-accuracy electronic structure calculations, such as DFT+GW [28, 69]. Within the fitting procedure, we describe the real-space atomistic pseudopotential, $\hat{v}_{\alpha}(\boldsymbol{r})$, by its reciprocal-space counterpart, $\hat{\tilde{v}}_{\alpha}(\boldsymbol{q})$. The functional form of the local reciprocal-space pseudopotential used for the work presented throughout this dissertation is:

$$\hat{\tilde{v}}_{\alpha}(\boldsymbol{q}) = a_0^{\alpha} \frac{q^2 - a_1^{\alpha}}{a_2^{\alpha} \exp(a_3^{\alpha} q^2) - 1}\,. \tag{2.2}$$

The addition of nonlocal terms and their functional form will be the subject of discussion in this chapter.

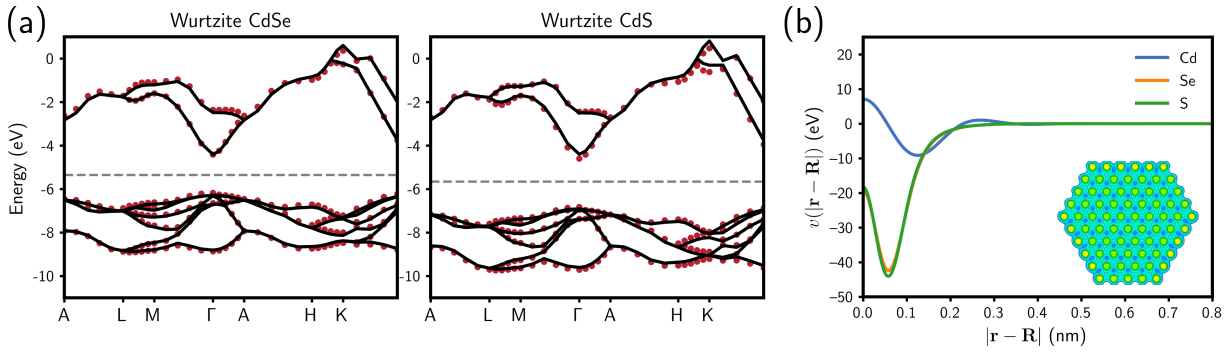

Figure 2.1: (a) The bulk band structures of wurtzite CdSe (left) and CdS (right) obtained from the pseudopotential Hamiltonian (red points) are compared to literature values [81] (black lines). The resulting band structures show excellent agreement across the entire Brilouin zone. (b) The corresponding real-space pseudopotentials for Cd, Se, and S. The inset illustrates a cross-section of the pseudopotential for a wurtzite 3.9 nm CdSe NC as constructed from these atom-centered functions.

The fitting of parameters $\{a_0, a_1, a_2, a_3\}$ proceeds by comparing the generated band structures to the expected band structures with special care taken to correctly capture the band gaps and effective masses. Additional discussion on the fitting process is the subject of Chapter 3. As shown in Fig. 2.1a, the model using a local-only pseudopotential captures

all band features and describes the band structure across the entire Brillouin zone. The real-space forms of the corresponding pseudopotentials are illustrated in Fig. 2.1b, where the pseudopotentials have been simultaneously fit to generate the correct band structures for both wurtzite and zincblende CdSe and CdS. Pseudopotential parameters for Cd, Se, S, In, As, and P that are used for electronic structure calculations in this section are collected in Table 2.1.

Table 2.1: Pseudopotential parameters for Cd, Se, S, In, As, and P. Cd, Se, and S parameters were fit to simultaneously reproduce wurtzite and zincblende CdSe and CdS bulk band structures. In, As, and P parameters were fit to simultaneously reproduce zincblende InAs and InP bulk band structures. All parameters are given in atomic units.

	a_0	a_1	a_2	a_3
Cd	-31.4518	1.3890	-0.0502	1.6603
Se	8.4921	4.3513	1.3600	0.3227
S	7.6697	4.5192	1.3456	0.3035
In	49.6411	1.8874	3.5301	0.4235
As	25.7465	2.6905	1.5253	0.5721
P	28.8706	2.5839	1.5821	0.5622

Once the pseudopotentials have been fit to describe bulk systems (the fits are not unique and often other physical measures are used to choose the best set of parameters [30]), they are used to construct the NC Hamiltonian. The central assumption made here is that the pseudopotentials that describe single particle properties in the bulk are also adequate when applied to quantum confined nanostructures. While this may seem to be a large leap, the error introduced by this assumption is relatively small compared to the fundamental band gap [82]. A cross-section of the resulting pseudopotential for a wurtzite 3.9 nm CdSe NC is shown in the inset of Fig. 2.1b, illustrating both the near-periodic potential in the interior of the NC and the manner by which it is modified at the surface. The NC atomic configurations are obtained by first pruning a bulk structure such that all atoms are bonded to at least two other atoms. The atomic positions are then relaxed using molecular dynamics-based geometry optimization with previously-parameterized force fields [83, 84], which include two- and three-body terms to enforce tetrahedral bonding geometries and produce NC configurations that are relatively crystalline in agreement with experiment [85]. In the case of core/shell structures, the core is cut from bulk, and the shell material is grown on the surface using the lattice constant of the core material. The subsequent geometry optimization allows the shell to relax and results in compressive strain on the core to minimize the stress along the core/shell interface [86, 87].

The description of the surface of the NC presents a challenge, as simply terminating the NC may result in dangling bonds. These dangling bonds can give rise to localized electronic

states within the band gap, which act as traps. For the II-VI and III-V families of semiconductors, we have found that dangling bonds from the non-metal atoms result in hole traps slightly above the valence band maximum, but metal dangling bonds do not result in electron traps due to the light electron effective mass relative to the hole effective mass [34, 75]. To passivate the surface of the NC, the outermost layer of atoms is replaced with passivation potentials that mimic the effect of organic ligands that terminate the surfaces of experimentally synthesized NCs, pushing the mid-gap states out of the band gap [10]. Lead halide perovskite NCs do not require passivation as if they are terminated to only leave halide dangling bonds. This procedure for building NC structures can be easily adapted to produce more complicated NCs, such as the core/shell NCs, nanorods, and nanoplatelets. Further modification, such as alloying, multi-layered NCs, dimer NC assemblies, and structural defects can also be modeled with atomistic detail.

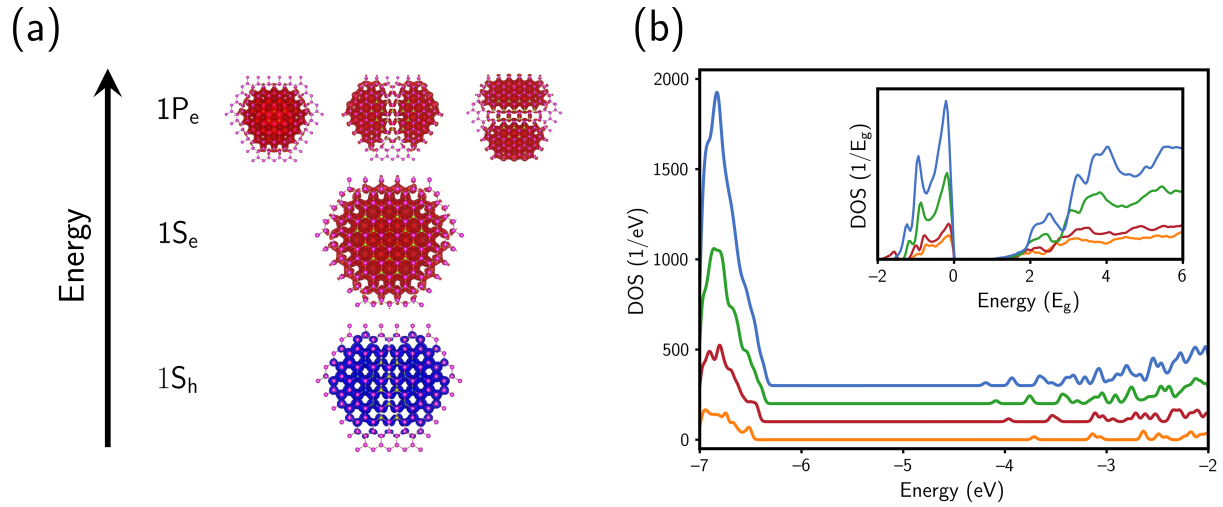

Figure 2.2: (a) Densities of the quasi-electron (red) and quasi-hole (blue) wavefunctions reveal that they are periodic across several unit cells in the interior of the NC. The electron states are labeled based on the symmetry of the envelope function in analogy to effective mass descriptions. (b) The densities of single-particle states (DOS) for wurtzite CdSe NCs of different sizes shows the effects of quantum confinement and the larger density of hole states in these II-VI systems. The inset illustrates the DOS across a larger energy range (that is scaled to the fundamental gap, E_g, of each NC), where the continuum of high energy states can be seen. The diameters of the NCs illustrated are 2.2 nm (orange), 3.0 nm (red), 3.9 nm (green), and 4.7 nm (blue).

While a NC of experimentally relevant size will have many single-particle states (see Fig. 2.2b), only a few highest-energy, occupied and lowest-energy, unoccupied states are relevant to describing the optical properties near the band edge. These single-particle states

are obtained using the filter diagonalization method [61, 62], which provides a framework to extract all the eigensolutions within a specific energy window. This process can be done with nearly linear scaling with the system size due to the locality of the single-particle Hamiltonian, making feasible the calculation for NCs with volumes spanning several orders of magnitude. Even with nonlocal potentials, this scaling can be preserved if the nonlocal effects are contained withing a small volume around each atom. As the pseudopotentials are fit to reproduce quasiparticle band structures, the eigenstates of the pseudopotential Hamiltonian are assumed to describe the quasi-electron and quasi-hole wave functions of the NC. Examples of the quasi-electron and quasi-hole densities are shown in Fig. 2.2a. We see that both the electron and hole states show Bloch-like oscillations, which are significantly more pronounced for the hole, and the electron states show a progression of envelope functions with s-type then p-type characteristics, in line with effective mass descriptions of NC electronic states [12, 41].

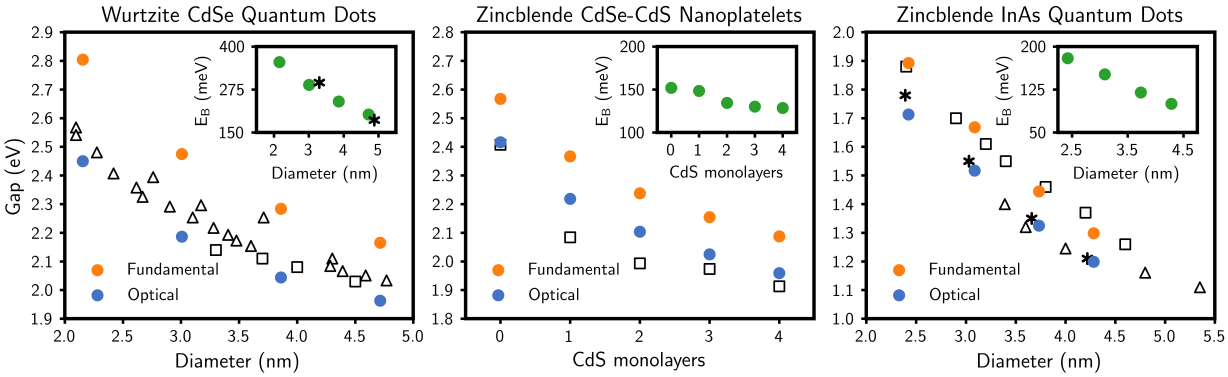

Figure 2.3: Gaps for wurtzite CdSe quantum dots of different sizes (left). The optical gaps computed by our semiempirical pseudopotential method agree with experimental measurements of the optical gap by Fan *et al.* [88] (black squares) and Yu *et al.* [89] (black triangles). The inset shows the exciton binding energy, E_{B}, computed by our method and compared to values computed by Franceschetti and Zunger [90] (black asterisks). Gaps for zincblende CdSe/CdS core/shell nanoplatelets with different thicknesses of CdS shell (middle). The optical gaps calculated by our method compare favorably with those measured experimentally by Hazarika *et al.* [87] (black squares). Gaps for zincblende InAs quantum dots of different sizes (right). The fundamental gaps calculated are in excellent agreement with those measured by Banin *et al.* [91] using scanning tunneling microscopy (black squares), and the optical gaps compare well with those measured by Guzelian *et al.* [92] (black triangles) and computed by Franceschetti and Zunger [93] (black asterisks).

As previously stated, connection to experiments also requires an accurate description of the neutral excited states probed by optical spectroscopy. To account for electron-hole correlations, we use the single-particle eigenstates as the basis to solve the Bethe-Salpeter equation (BSE) [63] for the correlated excitonic states using the static screening approxi-

mation [94]. This approach explicitly includes electron-hole correlations, which allows for the accurate description of excitons across all confinement regimes using just one formalism, instead of relying on different approximations for different regimes. We take the excitonic states to be a linear combination of noninteracting, electron-hole pair states:

$$|\psi_n\rangle = \sum_{ai} c^n_{a,i} \hat{a}^\dagger_a \hat{a}_i |0\rangle \,, \tag{2.3}$$

where $\hat{a}^\dagger_a$ and $\hat{a}_i$ are electron creation and annihilation operators in quasiparticle states a and i, respectively. The indexes $a, b, c, \ldots$ refer to quasi-electron (unoccupied) states while the indexes $i, j, k, \ldots$ refer to quasi-hole (occupied) states. The expansion coefficients $c_{a,i}$ are determined by solving the eigenvalue equation [63]:

$$(E_n - \Delta\varepsilon_{ai}) c^n_{a,i} = \sum_{bj} \left(K^d_{ai;bj} + K^x_{ai;bj} \right) c^n_{b,j} \,, \tag{2.4}$$

which also determines the energy of exciton n, E_n, in terms of the direct and exchange parts of the electron-hole interaction kernel [63], $K^d_{ai;bj}$ and $K^x_{ai;bj}$, respectively, and the quasiparticle energy difference, $\Delta\varepsilon_{ai} = \varepsilon_a - \varepsilon_i$. The direct part of the kernel describes the main attractive interaction between quasi-electrons and quasi-holes while the exchange part controls details of the excitation spectrum, such as the singlet-triplet splittings. Importantly, the direct term is mediated by a screened Coulomb interaction [63], which we approximate using the static screening limit with a dielectric constant that is obtained directly from the quasiparticle Hamiltonian [42] and that depends on the size and shape of the NC. The binding energy of excitonic state n, E^n_{B}, is calculated as:

$$E^n_{\mathrm{B}} = \sum_{abij} \left(c^n_{a,i} \right)^* \left(K^d_{ai;bj} + K^x_{ai;bj} \right) c^n_{b,j} \,. \tag{2.5}$$

As this model was built on semiempirical foundations, it is necessary to validate the resulting calculations on well-known NC properties before using the model to explore more complex phenomena. Furthermore, the fitting was carried out on pure bulk materials, so it is important to assess the performance of the model on different NCs across a range of sizes and compositions. One of the most fundamental properties we need to capture is the optical gap. As shown in Fig. 2.3, we obtain results that compare favorably with experiments with respect to the magnitude of the gap and the scaling with NC size for several different NC compositions and geometries. We additionally validate properties, such as exciton binding energies [64, 95], exciton fine structure effects on polarized emission [95, 96], radiative and Auger recombination lifetimes [64, 77, 97], and optical signals of trapped carriers [34]. The strong agreement we obtain between theoretical predictions and experimental observations across a variety of system sizes, compositions, and dimensionalities demonstrates that our approach is suitable for understanding and rationalizing trends across a wide range of nanomaterial systems. Additionally, this model is extremely versatile and lends itself to new development and expansion, such as the incorporation of nonlocal and spin-orbit terms which we now turn to.

2.1.1 Nonlocal pseudopotentials

Nonlocal terms can enter our pseudopotential for several reasons and have been widely used since the early development of the method [40, 80, 98–100]. The basic physical motivation for the pseudopotential theory is that a the highly oscillatory valence wave functions may be smoothed out by replacing the true potential with a pseudopotential which creates a smooth core region, however doing this in a systematic manner will in general result in nonlocal terms in the pseudopotential. This can be seen via the Phillips-Kleinmann cancellation theorem [101]. If we take a generic single particle Hamiltonian with a local potential $\hat{h} = \hat{t} + v(\hat{\boldsymbol{r}})$ where we know the eigenvalues and states ($|\Psi_n\rangle$, E_n) we can attempt to rewrite a highly oscillatory valence state $|\Psi_v\rangle$ as the sum of a smooth "pseudo" state $|\Phi_v\rangle$ and contributions from core states $|\Psi_c\rangle$:

$$|\Psi_v\rangle = |\Phi_v\rangle + \sum_c a_{v,c} |\Psi_c\rangle \ . \tag{2.6}$$

If we now consider how the Hamiltonian acts on this smooth state $|\Phi_v\rangle$

$$\hat{h}|\Phi_v\rangle = E_v|\Psi_v\rangle - \sum_c a_{v,c}E_c|\Psi_c\rangle \tag{2.7}$$

$$= E_v|\Phi_v\rangle - \sum_c a_{v,c}(E_c - E_v)|\Psi_c\rangle \tag{2.8}$$

$$= E_v|\Phi_v\rangle + \left[\sum_c (E_c - E_v)|\Psi_c\rangle\langle\Psi_c|\right]|\Phi_v\rangle \ , \tag{2.9}$$

we see that if we subtract the term in brackets to the Hamiltonian then we will have a new Hamiltonian for which the smooth state is an eigenstate with the proper energy. This motivates the pseudopotential of the form

$$\hat{v}_p = v(\hat{\boldsymbol{r}}) + \sum_c (E_v - E_c)|\Psi_c\rangle\langle\Psi_c| \ , \tag{2.10}$$

which is now clearly both nonlocal and energy dependent, but crucially since $E_v - E_c > 0$ the the pseudopotential is now shallower and smoother in the core region than the original potential. This construction is not generally used to generate pseudopotentials for practical use, but clearly shows how nonlocal terms may enter into the theory from the beginning. For many properties of semiconductor systems, however, the impact of nonlocality may be ignored, and fully local pseudopotential theories have been of great utility as we have seen in the previous section.

The introduction of spin-orbit coupling into the Hamiltonian forces the consideration of nonlocal terms. The operator describing spin-orbit coupling can be derived from the consideration of the effects of relativity on the electric field of the nuclei from the rest frame

of an electron. The electron will experience some portion of this electric field as a magnetic field

$$\boldsymbol{B}' = -\gamma \frac{\boldsymbol{v}}{c} \times \boldsymbol{E}\,, \tag{2.11}$$

where if we assume that the electric field emanates radially from the nucleus we can simplify to

$$\boldsymbol{B}' = \gamma \frac{\boldsymbol{p}}{mc} \times \frac{1}{er}\frac{dV}{dr}\boldsymbol{x} \approx \frac{1}{emrc}\frac{dV}{dr}\boldsymbol{L}\,. \tag{2.12}$$

This magnetic field couples to the electron spin, and while in general the form of $\frac{dV}{dr}$ is not known it can be written as some radial function, $v_{SO}(r)$ that also absorbs all the coeffecients

$$h_{SO} = v_{SO}(r)\hat{\boldsymbol{L}} \cdot \hat{\boldsymbol{S}}\,. \tag{2.13}$$

This operator is clearly nonlocal as the angular momentum operator, $\hat{\boldsymbol{L}}$, depends on both position and momentum.

The presence of the angular momentum operator suggests the common approach through which to incorporate additional nonlocal effects. Instead of using only a local form of the pseudopotential, each atomic pseudopotential may be expanded in the angular momentum subspaces around the given atom:

$$\hat{v}_\alpha = \sum_l v_l^\alpha(\hat{r}_\alpha)\hat{P}_l^\alpha\,, \tag{2.14}$$

where $\hat{P}_l^\alpha = \sum_m |l,m\rangle_\alpha \langle l,m|_\alpha$ is the projector onto the l angular momentum subspace around atom α and $\hat{r}_\alpha = |\hat{\boldsymbol{r}} - \boldsymbol{R}_\alpha|$ is the distance to atom α. In the case of spin-orbit coupling these may be total angular momentum subspaces formed from the coupling of electron spin and orbital angular momentum. Additionally, it is generally practical to assign one of the angular momenta the role of the local potential, and keep only the difference between that potential for the other angular momentum subspaces. In our case we have chosen to make the $l = 0$ subspace (i.e. the s orbitals) the local potential so, the potential then becomes

$$\hat{v}_\alpha = v_{loc}^\alpha(\hat{\boldsymbol{r}}) + \sum_{l\neq 0} \delta v_l^\alpha(\hat{r}_\alpha)\hat{P}_l^\alpha\,. \tag{2.15}$$

The pseudopotential Hamiltonian we will then use in the following section is:

$$\hat{h} = \hat{t} + \sum_\alpha \left[v_{loc}^\alpha(\hat{r}_\alpha) + \sum_{l\neq 0} \delta v_l^\alpha(\hat{r}_\alpha)\hat{P}_l^\alpha + \hat{v}_{SO}^\alpha(\hat{r}_\alpha)\hat{\boldsymbol{L}}^\alpha \cdot \hat{\boldsymbol{S}} \right]\,. \tag{2.16}$$

A crucial consideration when using the semi-empirical pseudopotential method is that the same pseudopotential Hamiltonian will have to be used both for computing bulk band structures with a plane wave basis during the fitting process, and for computing quasiparticle states of finite systems on a real space grid. For a local potential ensuring this correspondence is simple, however when a nonlocal potential is used the decision of how to represent the

nonlocal operator will have a significant impact on both the efficiency and accuracy that may be different depending on which basis is being used. Thus, ensuring the correspondence of the pseudopotential Hamiltonian used for fitting with the Hamiltonian used for finite systems becomes less trivial and will be examined in the following sections.

2.2 Bulk Calculations with a Nonlocal Potential

To calculate a bulk material band structure using these nonlocal pseudopotentials with spin orbit coupling, we solve the pseudopotential Hamiltonian given in Eqn. 2.16 in a basis of spinor plane wave states. As we know our solutions will have the Bloch form, we can consider the Hamiltonian associated with a specific vector $\boldsymbol{k}$ in the first Brillioun zone. Our basis is the set of states $|\boldsymbol{K}, s\rangle$ where $\boldsymbol{K} = \boldsymbol{k} + \boldsymbol{G}$ for all $\boldsymbol{G}$ that are in the reciprocal space lattice of the material and $s \in \{\uparrow, \downarrow\}$ is a one-electron spin function.

The kinetic energy matrix is already diagonal in this basis,

$$\langle \boldsymbol{K}, s|\hat{t}|\boldsymbol{K}', s'\rangle = \frac{\hbar^2 K^2}{2m}\delta_{K,K'}\delta_{s,s'}\,, \tag{2.17}$$

and the local part of the potential is known to be

$$\langle \boldsymbol{K}, s|\, v_{loc}^{\alpha}(\hat{\boldsymbol{r}})\,|\boldsymbol{K}', s'\rangle = \left(\sum_{\alpha}^{\text{atoms}} \tilde{v}_{\alpha}(|\boldsymbol{K}-\boldsymbol{K}'|)e^{i(\boldsymbol{K}-\boldsymbol{K}')\cdot\boldsymbol{R}_{\boldsymbol{\alpha}}}\right)\delta_{s,s'}\,, \tag{2.18}$$

where $\tilde{v}_{\alpha}(|\boldsymbol{K}-\boldsymbol{K}'|)$ is the k-space pseudopotential around atom α, which is located at position $\boldsymbol{R}_{\alpha}$. This part couples different $\boldsymbol{K}$-basis states only as long as they have common spin, so it has zeros in both of the off-diagonal quadrants.

We will now turn to the spin-orbit operator. For simplicity will initially consider only the case of a single atom, dropping the αs where they are redundant, and will later show the simple extension to multiple atoms.

$$\hat{V}_{SO} = v_{SO}\,(\hat{r})\,\hat{\mathbf{L}}\cdot\hat{\mathbf{S}} \tag{2.19}$$

$$= \sum_{l}\sum_{m=-l}^{l}\sum_{\sigma}\int r^2 dr\; v_{SO}\,(\hat{r})\,|lmr\sigma\rangle\,\langle lmr\sigma|\,\hat{\boldsymbol{L}}\cdot\hat{\boldsymbol{S}} \tag{2.20}$$

$$= \sum_{l}\sum_{mm'}\sum_{\sigma\sigma'}\int r^2 dr\,|lmr\sigma\rangle\,\mathbf{L}^{l}_{m,m'}\cdot\mathbf{S}_{\sigma,\sigma'}v_{SO}\,(r)\,\langle lm'r\sigma'| \tag{2.21}$$

where a resolution of the identity has presented the operator in a matix form in the basis of spherical harmonic functions with definite spin and radius which have wavefunctions:

$$\langle lmr\sigma|\mathbf{r}'\sigma'\rangle = Y^{*}_{lm}\,(\boldsymbol{r}')\,\frac{\delta\,(r-r')}{r^2}\delta_{\sigma\sigma'} \tag{2.22}$$

where $Y_{lm}(\boldsymbol{r}')$ is the standard spherical harmonic of degree l and order m evaluated at the point on the unit sphere corresponding to the direction of $\boldsymbol{r}'$. Note that we will use the quantum mechanical conventions on phase and normalization of spherical harmonics. This basis is a useful as it nearly diagonalizes the operator and only leaves the key mixing of spin and orbital angular momentum. While a basis of total angular momentum eigenstates would fully diagonalize the spin-orbit operator, they would require considering both the up and down spin components for each function. Because we are working in a spinor basis it is much easier to use basis functions of definite spin.

To convert this to the plane wave basis we need to know the change-of-basis matrix elements

$$\langle lmr\sigma|\mathbf{k}\sigma\rangle = \frac{1}{\sqrt{\Omega}}\int d^3\mathbf{r}'\frac{\delta(r-r')}{r^2}Y_{lm}^*(\mathbf{r}')\,e^{-i\mathbf{k}\cdot\mathbf{r}'} \tag{2.23}$$

This can be simplified using the plane wave expansion

$$e^{-i\mathbf{k}\cdot\mathbf{r}} = 4\pi\sum_{l=0}^{\infty}\sum_{m=-l}^{l}(-i)^l\,j_l(kr)\,Y_{lm}^*(\mathbf{k})\,Y_{lm}(\mathbf{r}) \tag{2.24}$$

and the orthogonality of spherical harmonics

$$\iint Y_{lm}(\mathbf{r})\,Y_{l'm'}(\mathbf{r})\,d\theta d\phi = \delta_{ll'}\delta_{mm'}\,. \tag{2.25}$$

Applying these equalities, the overlap integral can be simplified to

$$\langle lmr\sigma|\boldsymbol{k}\sigma\rangle = \frac{1}{\sqrt{\Omega}}\int d^3\boldsymbol{r}'\frac{\delta(r-r')}{r^2}Y_{lm}^*(\boldsymbol{r}')\,e^{-i\boldsymbol{k}\cdot\boldsymbol{r}'} \tag{2.26}$$

$$= \frac{4\pi}{\sqrt{\Omega}}\sum_{l'=0}^{\infty}\sum_{m=-l'}^{l'}(-i)^{l'}\,Y_{l'm'}^*(\mathbf{k})\int d^3\mathbf{r}'\frac{\delta(r-r')}{r^2}Y_{lm}^*(\mathbf{r}')\,j_{l'}(kr')\,Y_{l'm'}(\mathbf{r}') \tag{2.27}$$

$$= \frac{-4\pi i}{\sqrt{\Omega}}Y_{lm}^*(\mathbf{k})\,j_l(kr) \tag{2.28}$$

plugging this into Eqn. 2.21 we get

$$\langle\boldsymbol{k}\sigma|\,\hat{V}_{SO}\,|\boldsymbol{k}'\sigma'\rangle = \sum_{lmm'}\frac{16\pi^2}{\Omega}\left[Y_{lm}(\boldsymbol{k})\,Y_{lm'}^*(\boldsymbol{k}')\,\boldsymbol{L}_{m,m'}^l\cdot\boldsymbol{S}_{\sigma,\sigma'}\int_0^\infty r^2dr\,j_l(kr)\,v_{SO}(r)\,j_l(k'r)\right] \tag{2.29}$$

The part with the $\mathbf{L}$ operator can be simplified further following the approach of Weisz [102]. To do this we first make a rotation of the coordinate systems so that $\mathbf{k}\parallel\mathbf{z}$ and $\mathbf{k}'\parallel\mathbf{x}\sin\alpha+\mathbf{z}\cos\alpha$ so

$$\frac{\mathbf{k}\times\mathbf{k}'}{kk'} = \mathbf{z}\times\mathbf{x}\sin\alpha = \mathbf{y}\sin\alpha\,, \tag{2.30}$$

and so that the spherical harmonic that has been aligned with the $\boldsymbol{z}$ axis has a simple form as

$$Y_{lm}\left(\boldsymbol{k}\right) = Y_{lm}\left(\boldsymbol{z}\right) = \sqrt{\frac{2l+1}{4\pi}}\delta_{m,0}\,. \tag{2.31}$$

We the take the vector $\boldsymbol{L}_{m,m'}$ one component at a time. We start with the z component where, since and $L^z_{0,m'} = 0$, we can clearly see that

$$\sum_{mm'} Y_{lm}\left(\boldsymbol{k}\right) L^z_{m,m'} Y^*_{lm'}\left(\boldsymbol{k}'\right) = 0\,. \tag{2.32}$$

Now we can turn to the x and y components where we will avail ourselves of the raising and lowering operators to express

$$L^x_{m,m'} = \frac{1}{2}\left(L^+_{m,m'} + L^-_{m,m'}\right) \tag{2.33}$$

$$L^y_{m,m'} = \frac{-i}{2}\left(L^+_{m,m'} - L^-_{m,m'}\right)\,. \tag{2.34}$$

Since the raising and lowering operators can only change m' by one we can see that we only need to consider the terms where $m' = \pm 1$. For the raising operator we get that

$$\sum_{mm'} Y_{lm}(\boldsymbol{k}) L^+_{m,m'} Y^*_{lm'}(\boldsymbol{k}') = \sum_{mm'} \sqrt{\frac{2l+1}{4\pi}}\delta_{m,0}\sqrt{l(l+1)}\delta_{m-1,m'} Y^*_{lm'}(\boldsymbol{k}') \tag{2.35}$$

$$= \sqrt{\frac{2l+1}{4\pi}}\sqrt{l(l+1)} Y^*_{l,-1}(\boldsymbol{k}')\,. \tag{2.36}$$

Similarly for the lowering operator we get that

$$\sum_{mm'} Y_{lm}(\boldsymbol{k}) L^-_{m,m'} Y^*_{lm'}(\boldsymbol{k}') = \sqrt{\frac{2l+1}{4\pi}}\sqrt{l(l+1)} Y^*_{l,1}(\boldsymbol{k}')\,. \tag{2.37}$$

Now, since we have aligned our axes such that $\boldsymbol{k}'$ lies in the x-z plane, $Y_{l,m}(\boldsymbol{k}')$ is purely real and thus,

$$Y_{l,1}(\boldsymbol{k}') = -Y^*_{l,-1}(\boldsymbol{k}') = -Y_{l,-1}(\boldsymbol{k}')\,. \tag{2.38}$$

We can use this now to show that the x component comes to

$$\sum_{mm'} Y_{lm}(\boldsymbol{k}) L^x_{m,m'} Y^*_{lm'}(\boldsymbol{k}') = \frac{1}{2}\sum_{mm'} Y_{lm}(\boldsymbol{k})\left(L^+_{m,m'} + L^-_{m,m'}\right) Y^*_{lm'}(\boldsymbol{k}') \tag{2.39}$$

$$= \frac{1}{2}\sqrt{\frac{2l+1}{4\pi}}\sqrt{l(l+1)}\left(Y^*_{l,1}(\boldsymbol{k}') + Y^*_{l,-1}(\boldsymbol{k}')\right) \tag{2.40}$$

$$= 0\,. \tag{2.41}$$

and the y component

$$\sum_{mm'} Y_{lm}(\boldsymbol{k}) L^y_{m,m'} Y^*_{lm'}(\boldsymbol{k}') = \frac{-i}{2} \sum_{mm'} Y_{lm}(\boldsymbol{k}) \left(L^+_{m,m'} - L^-_{m,m'} \right) Y^*_{lm'}(\boldsymbol{k}') \tag{2.42}$$

$$= \frac{-i}{2} \sqrt{\frac{2l+1}{4\pi}} \sqrt{l(l+1)} \left(Y^*_{l,1}(\boldsymbol{k}') - Y^*_{l,-1}(\boldsymbol{k}') \right) \tag{2.43}$$

$$= -i \sqrt{\frac{2l+1}{4\pi}} \sqrt{l(l+1)} Y_{l,1}(\boldsymbol{k}') \tag{2.44}$$

$$= -i \sqrt{\frac{2l+1}{4\pi}} \sqrt{l(l+1)} \left[-\sqrt{\frac{2l+1}{4\pi l(l+1)}} P^1_l(\cos\alpha) \right] \tag{2.45}$$

$$= i \frac{2l+1}{4\pi} P^1_l(\cos\alpha) \,, \tag{2.46}$$

where P^1_l is the first order associated Legendre polynomial of degree l. Generalizing out from our specially rotated coordinate system we can say that

$$\sum_{mm'} Y_{lm}(\boldsymbol{k}) \boldsymbol{L}^l_{m,m'} Y^*_{lm'}(\boldsymbol{k}') = i \frac{\boldsymbol{k} \times \boldsymbol{k}'}{|\boldsymbol{k} \times \boldsymbol{k}'|} \frac{2l+1}{4\pi} P^1_l \left(\frac{\boldsymbol{k} \cdot \boldsymbol{k}'}{kk'} \right) . \tag{2.47}$$

If we consider the first few associated Legendre polynomials of order 1,

$$P^1_1(\cos\alpha) = -\sin\alpha \tag{2.48}$$

$$P^1_2(\cos\alpha) = -3\cos\alpha\sin\alpha \tag{2.49}$$

$$P^1_3(\cos\alpha) = \frac{3}{2}(1 - 5\cos^2\alpha)\sin\alpha \,, \tag{2.50}$$

we see the expression can be simplified in terms of the vectors $\boldsymbol{k}$ and $\boldsymbol{k}$. Truncating to keep only the $l = 1$ components I get

$$\sum_{mm'} Y_{1m}\left(\hat{\mathbf{k}}\right) Y^*_{1m'}\left(\hat{\mathbf{k}}'\right) \mathbf{L}_{m,m'} = -i \frac{3}{4\pi} \frac{\mathbf{k} \times \mathbf{k}'}{kk'} \,. \tag{2.51}$$

The final generalization to a multi-atom unit cell is made by recognizing the different positions merely impact the phase at which the plane waves meet the atomic potential, which gives a form which corresponds with that considered by Hybersten and Louie [69]:

$$V_{SO}\left(\mathbf{k}\sigma, \mathbf{k}'\sigma'\right) = -i \frac{12\pi}{\Omega} \frac{\mathbf{k} \times \mathbf{k}'}{kk'} \left[\sum_\alpha \int_0^\infty r^2 dr \, j_1(kr) \, v^\alpha_{SO}(r) \, j_1(k'r) \, e^{i(\boldsymbol{k}-\boldsymbol{k}')\cdot\boldsymbol{R}_\alpha} \right] \cdot \mathbf{S}_{\sigma,\sigma'} \tag{2.52}$$

To validate this approach, I compared the results of my band structures to those obtained by Williamson [42] using a very similar pseudopotential method, but a distinct implementation of the spin-orbit coupling effects.

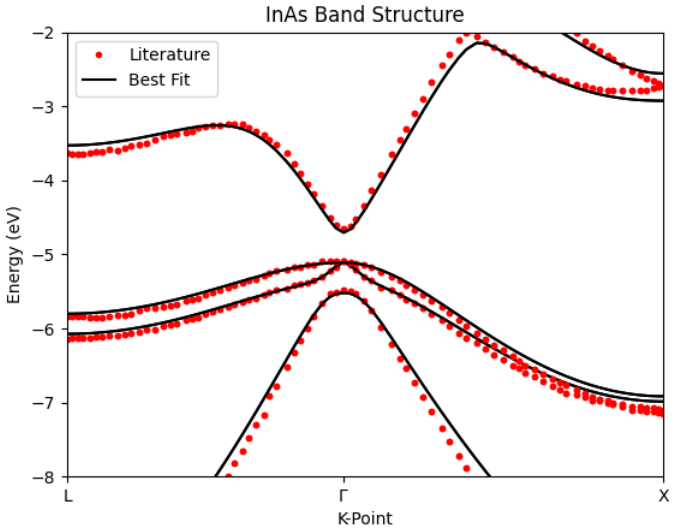

Figure 2.4: A comparison of the InAs band structure including spin-orbit effects, calculated by Williamson [42] (red points), and that calculated using the procedure discussed herein (black lines).

The band structures shown in Figure 2.4 show very strong agreement, particularly around the band gap at the Γ point. The disagreement farther away from the band gap likely comes from the particularities of the Williamson calculation. Due to the computational limitations of the time the pseudopotential calculations were not performed in a converged plane wave basis, but were calculated using a kinetic energy cut-off of 2.5 Hartree [42].

The additional nonlocal parts of the pseudopotential can also be considered in this plane wave basis. Considering the terms found in Equation 2.16 we can tackle them in a very similar manner to the spin-orbit terms.

$$\delta\hat{V}_{\text{nonloc}} = \sum_{\alpha}\sum_{l\neq 0}\delta v_l^{\alpha}(\hat{r}_\alpha)\hat{P}_l^{\alpha} \tag{2.53}$$

$$= \sum_{\alpha}\sum_{l\neq 0}\sum_{m}\int r^2\,|lmr_\alpha\sigma\rangle\,dr\;\delta v_l^{\alpha}(\hat{r}_\alpha)\,\langle lmr_\alpha\sigma| \tag{2.54}$$

Using the same overlap matrix elements we calculated earlier we can see that

$$\langle \boldsymbol{k}\sigma|\,\delta\hat{V}_{\text{nonloc}}\,|\boldsymbol{k}'\sigma'\rangle = \sum_{\alpha}\sum_{l\neq 0}\sum_{m}\frac{16\pi^2}{\Omega}Y_{lm}\left(\hat{\boldsymbol{k}}\right)Y_{lm}^{*}\left(\hat{\boldsymbol{k}}'\right)\left[\int_0^{\infty} r^2 dr\, j_l\left(kr\right)\delta v_l^{\alpha}\left(r\right)j_l\left(k'r\right)\right] \tag{2.55}$$

which can be simplified by the addition theorem of the spherical harmonics to get

$$\langle \boldsymbol{k}\sigma |\, \delta\hat{V}_{\text{nonloc}} \,|\boldsymbol{k}'\sigma'\rangle = \sum_{\alpha} \sum_{l\neq 0} \sum_{m} \frac{4\pi(2l+1)}{\Omega} P_l\left(\frac{\boldsymbol{k}\cdot\boldsymbol{k}'}{kk'}\right) \left[\int_0^\infty r^2 dr\, j_l\left(kr\right) \delta v_l^\alpha\left(r\right) j_l\left(k'r\right)\right] \tag{2.56}$$

Using these nonlocal terms in conjunction with the spin-orbit terms of the pseudopotential gives independent control over each of the total angular momentum components. Based on the addition of angular momenta the total angular momentum state $|j, m_j, l\rangle$ will see a potential equal to

$$v(r) = v_{\text{loc}}(r) + \left[\frac{j(j+1)}{2} - \frac{l(l+1)}{2} - \frac{3}{8}\right] v_{so}(r) + \delta v_l(r)\,. \tag{2.57}$$

This independent control of each of the angular momentum components allows for significant additional flexibility for fitting the pseudopotentials to reproduce literature band structures. For example when fitting the pseudopotential forms for the $CsPbI_3$ perovskites, the nonlocal potential was crucial to better fitting the effective masses and band gaps.

2.3 Using a Nonlocal Pseudopotential in Confined Systems

As discussed previously, in order to use these pseudopotentials for calculations in finite systems it is necessary to understand how to represent them on the real-space grid used in these calculations. For the local potential this was an intuitive and straightforward process, but the introduction of nonlocal elements requires additional considerations. Equation 2.21 suggests a simple way to do this, however a detailed analysis will show that this naive approach is inefficient and prone to significant error, requiring the development of a different, separable form of the spin-orbit operator.

In these finite systems we want to calculate the action of the Hamiltonian on a state expressed in a basis of real space spinor grid points, i.e the set of basis states $|\boldsymbol{r}, \sigma\rangle$ where $\boldsymbol{r} = n_x\boldsymbol{a}_x + n_y\boldsymbol{a}_y + n_z\boldsymbol{a}_z$ for integers $n_{\{x,y,z\}}$ and grid basis vectors $\boldsymbol{a}_{\{x,y,z\}}$. To evaluate the correspondence of the real-space form of the nonlocal operator I first solved for eigenstates at the Γ point in the plane wave basis $|\psi_n\rangle = \sum_{\boldsymbol{G},\sigma} c_{n,\boldsymbol{G},\sigma} |\boldsymbol{G}, \sigma\rangle$as described above. I then cast that state into the real space basis by evaluating $\psi_n(\boldsymbol{r}, \sigma) = \sum_{\boldsymbol{G}} c_{n,\boldsymbol{G},\sigma} e^{-i\boldsymbol{G}\cdot\boldsymbol{r}}$ at all of the points $\boldsymbol{r}$ on the real space grid. The operator in the real-space representation is then applied and both the expectation value, $\langle\psi|\,\hat{O}\,|\psi\rangle$, and the quality of the eigenstate, $\langle\psi|\,\hat{O}\,|\psi\rangle^2 - \langle\psi|\,\hat{O}^2\,|\psi\rangle$ is calculated to determine if the operator is in fact identical in the two representations.

2.3.1 Naive formalism and error

The action of the spin orbit operator in real space takes the form of

$$\langle \mathbf{r}, \sigma | \hat{V}_{SO} | \psi \rangle = \langle \mathbf{r} | \sum_{\sigma'} \int d\mathbf{r}' \psi(\mathbf{r}', \sigma') \left[\sum_{\alpha}^{\text{atoms}} |l_\alpha = 1\rangle \lambda_\alpha v_{SO}(|\mathbf{r}_\alpha|) \hat{\mathbf{L}}^\alpha \langle l_\alpha = 1| \right] |\mathbf{r}'\rangle \cdot \langle \sigma | \hat{\mathbf{S}} | \sigma' \rangle \tag{2.58}$$

$$= \sum_{\alpha}^{\text{atoms}} \lambda_\alpha v_{SO}(|\mathbf{r}_\alpha|) * \sum_{\sigma'} \sum_{m,m'=-1}^{1} Y_{1,m}(\mathbf{r}_\alpha) \mathbf{L}_{m,m'} \int d\mathbf{r}' \frac{\delta(r_\alpha - r'_\alpha)}{r'^2} Y^*_{1,m'}(\mathbf{r}'_\alpha) \psi(\mathbf{r}', \sigma') \cdot \mathbf{S}_{\sigma,\sigma'} \tag{2.59}$$

It turns out that its very hard to take the integrals of the form

$$\langle lmr\sigma | \psi, \sigma' \rangle = \int d\mathbf{r}' \frac{\delta(r_\alpha - r'_\alpha)}{r'^2} Y^*_{1,m'}(\mathbf{r}'_\alpha) \psi(\mathbf{r}', \sigma') \delta_{\sigma,\sigma'} \tag{2.60}$$

$$= \int_0^\pi d\theta' \sin\theta' \int_0^{2\pi} d\phi Y^*_{l,m}(\theta', \phi') \psi(r, \theta', \phi', \sigma') \delta_{\sigma,\sigma'} \tag{2.61}$$

on a rectangular grid as it requires a set of points all at radius r from atom α. As an initial attempt we tried to approximate the delta function with a Gaussian sharply peaked at the appropriate radius, and integrate over all rectangular grid points within a cutoff radius R_c.

$$\langle lmr\sigma | \psi, \sigma' \rangle \approx \frac{1}{\sqrt{2\pi a^2}} \int_0^{R_c} dr' \int_0^\pi d\theta' \sin\theta' \int_0^{2\pi} d\phi' \exp\left(-\frac{(r - r')^2}{2a^2} \right) Y^*_{l,m}(\theta', \phi') \psi(r', \theta', \phi') \tag{2.62}$$

$$= \frac{1}{\sqrt{2\pi a^2}} \iiint_{r' < R_c} \frac{d\boldsymbol{r}'}{r'^2} \exp\left(-\frac{(r - r')^2}{2a^2} \right) Y^*_{l,m}(\boldsymbol{r}') \psi(\boldsymbol{r}') \tag{2.63}$$

Numerically calculating this approximation shows that this integral is poorly behaved numerically since the Gaussian will no longer be normalized for short r where there is a significant portion of the function that falls in *negative* r and thus isn't included in the integral. Furthermore this is highly computationally inefficient as for each point within the cutoff radius the integral runs over all other points in that sphere giving a scaling of $O(N^2_{\text{nonloc}})$ where N_{nonloc} is the number of grid points in the cutoff radius.

2.3.2 Derivation of projector formalism

The issue here is that the radial part of the angular momentum eigenfunctions $|lmr\sigma\rangle$ is a delta function of radius which is not well defined on our rectangular grid. We then need

to find a different set of angular momentum eigenfunctions with a radial part more easily represented on this grid, but that still capture the spatial variation of the spin-orbit coupling. We do this by assuming the spin orbit operator can be put into a separable form (similar to the Kleinman-Bylander form [103, 104]) and then derive the radial functions needed to give equality with the non-separable form up to a certain kinetic energy cutoff.

Taking the spin-orbit coupling around a single atom:

$$\hat{V}_{SO} \approx |l=1\rangle\, v_{SO}(|\mathbf{r}|)\hat{\mathbf{L}}\cdot\hat{\mathbf{S}}\,\langle l=1| \tag{2.64}$$

$$= \sum_{\sigma,\sigma'}\sum_{m,m'}\int r^2 dr\,|1m,r,\sigma\rangle\,\mathbf{L}_{m,m'}v_{SO}(r)\cdot\mathbf{S}_{\sigma,\sigma'}\,\langle 1m',r,\sigma'| \tag{2.65}$$

and we know that the plane wave matrix elements will be

$$\langle\mathbf{k},\sigma|\,\hat{V}_{SO}\,|\mathbf{k}',\sigma'\rangle = -i\frac{12\pi}{\Omega}\frac{\mathbf{k}\times\mathbf{k}'}{kk'}\cdot\hat{\mathbf{S}}_{\sigma\sigma'}\int_0^\infty dr\,r^2 j_1(kr)\,v_{SO}(r)\,j_1(k'r) \tag{2.66}$$

We want to rewrite the spin-orbit operator in a separable form with some to-be-determined radial functions ϕ_n

$$\hat{V}_{SO}^{sep} = \sum_{\sigma,\sigma'}\sum_{m,m'}\sum_{n}|1m,\phi_n,\sigma\rangle\,\mathbf{L}_{m,m'}\cdot\mathbf{S}_{\sigma,\sigma'}\,\langle 1m',\phi_n,\sigma'|\ , \tag{2.67}$$

where

$$\langle\boldsymbol{r}\sigma|1m\phi_n\sigma'\rangle = Y_{1m}^*(\boldsymbol{r})\phi_n(r)\delta_{\sigma\sigma'}\,. \tag{2.68}$$

We want these functions such that we best approximate the full operator on the plane waves by the separable operator:

$$\langle\mathbf{k},\sigma|\,\hat{V}_{SO}^{sep}\,|\mathbf{k}',\sigma'\rangle = \sum_n\left[\frac{1}{\Omega}\sum_{m,m'}\int d\mathbf{r}'e^{i\mathbf{k}\cdot\mathbf{r}}\phi_n(\mathbf{r})\,Y_{1m}(\mathbf{r})\,\mathbf{L}_{m,m'}\int d\mathbf{r}'e^{i\mathbf{k}'\cdot\mathbf{r}'}\phi_n^*(\mathbf{r}')\,Y_{1m}^*(\mathbf{r}')\right]\cdot\hat{\mathbf{S}}_{\sigma\sigma'} \tag{2.69}$$

$$= \frac{16\pi^2}{\Omega}\sum_{m,m'}Y_{1m}(\mathbf{k})\,Y_{1m'}^*(\mathbf{k}')\,\mathbf{L}_{m,m'}\cdot\hat{\mathbf{S}}_{\sigma\sigma'} * \sum_n\int r^2 dr j_1(kr)\,\phi_n(r)\int r^2 dr j_1(k'r)\,\phi_n^*(r) \tag{2.70}$$

$$= -i\frac{12\pi}{\Omega}\frac{\mathbf{k}\times\mathbf{k}'}{kk'}\cdot\hat{\mathbf{S}}_{\sigma\sigma'}\sum_n\int r^2 dr j_1(kr)\,\phi_n(r)\int r^2 dr j_1(k'r)\,\phi_n^*(r) \tag{2.71}$$

Thus, by equating the plane wave matrix elements of the non-separable (Equation 2.66) and separable (Equation 2.71) forms, we can see that we are looking for ϕ_n such that,

$$\sum_n\int r^2 dr j_1(kr)\,\phi_n(r)\int r^2 dr j_1(k'r)\,\phi_n^*(r) \approx \int_0^\infty dr\,r^2 j_1(kr)\,v_{SO}(r)\,j_1(k'r)\ , \tag{2.72}$$

for all k, k' below a given kinetic energy cutoff. The right hand side above is the matrix we call $\bar{V}_{\mathrm{SO}}(k, k')$, and let us call the identical integrals on the left hand side

$$b_n(k) = \int r^2 dr j_1(kr)\,\phi_n(r) \tag{2.73}$$

We find the optimal b_n by an eigendecomposition of $\bar{V}_{\mathrm{SO}}$. Taking a linearly spaced sampling of k values up to a $k_{\max}$ $\left\{k_i : i \leq N, k_i = \frac{ik_{\max}}{N}\right\}$ we find the eigenvalues and orthonormal eigenvectors of $\bar{V}_{\mathrm{SO}}$, which we call $\{\lambda_n\}$ and $\{u_n(k)\}$. The eigendecomposition gives us that $\bar{V}_{\mathrm{SO}}(k, k') = \sum_n b_n(k)\, b_n(k')$ where

$$b_n(k) = \sqrt{\lambda_n} u_n(k) \tag{2.74}$$

From the definition of b_n as a function of k we can then extract $\phi_n(r)$ using the orthogonality of the spherical Bessel functions

$$\int_0^\infty r^2 dr j_l(qr)\, j_l(q'r) = \frac{\pi}{2q^2}\delta(q - q') \tag{2.75}$$

thus

$$\int_0^\infty k^2 dk\, j_1(r'k)\, b_n(k) = \int_0^\infty k^2 dk \int_0^\infty r^2 dr j_1(r'k)\, j_1(rk)\,\phi_n(r) \tag{2.76}$$

$$= \int_0^\infty r^2 dr \phi_n(r) \int_0^\infty k^2 dk j_1(r'k)\, j_1(rk) \tag{2.77}$$

$$= \int_0^\infty r^2 dr \phi_n(r)\, \frac{\pi}{2r^2}\delta(r - r') \tag{2.78}$$

$$= \phi_n(r')\,\frac{\pi}{2} \tag{2.79}$$

The eigenvalues of $\bar{V}_{\mathrm{SO}}(k, k')$ are quite rapidly decaying so the full matrix can be well-approximated with only a handful of ϕ_n, as can be seen in Figure 2.5.

With these radial functions in hand we can calculate the action of the spin-orbit operator on a real space wavefunction

$$\langle \mathbf{r}, \sigma | \hat{V}_{SO}^{sep} | \psi_i \rangle = \sum_{\sigma,\sigma'} \sum_{m,m'} \sum_n \langle \mathbf{r}, \sigma | 1m\phi_n\sigma \rangle\, \mathbf{L}_{m,m'} \cdot \mathbf{S}_{\sigma,\sigma'} \langle 1m'\phi_n\sigma' | \psi_i \rangle \tag{2.80}$$

$$= \sum_{\sigma,\sigma'} \sum_{m,m'} \sum_n Y_{1,m}(\mathbf{r})\,\phi_n(r)\,\mathbf{L}_{m,m'} \cdot \mathbf{S}_{\sigma,\sigma'} \int d^3\mathbf{r}' Y^*_{1,m'}(\mathbf{r}')\,\phi_n(r')\,\psi_i(\mathbf{r}', \sigma') \tag{2.81}$$

$$= \sum_{\sigma,\sigma'} \sum_{m,m'} \sum_n Y_{1,m}(\mathbf{r})\,\phi_n(r)\,\mathbf{L}_{m,m'} \cdot \mathbf{S}_{\sigma,\sigma'} P_{n,m',\sigma'} \tag{2.82}$$

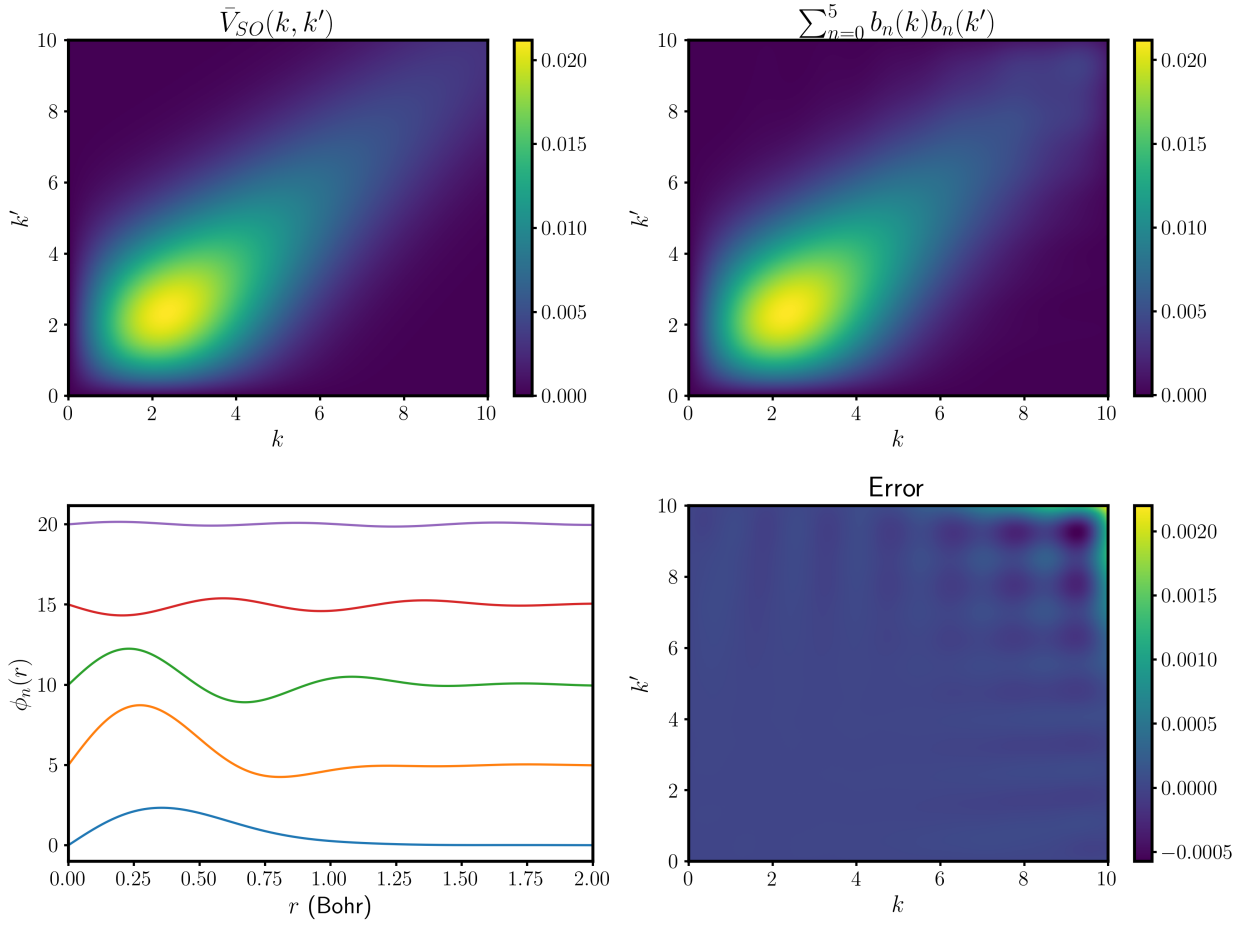

Figure 2.5: (top left) The matrix of the right hand side of equation 2.72. (top right) The matrix of the left hand side of equation 2.72 using 5 projection functions. (bottom left) The real space projectors ϕ_n defined above. (bottom right) The error between the right and left sides of equation 2.72.

Using this we can calculate the expected energy levels at the gamma point within the plane wave formalism and the real space formalism. Comparing the energy of the spin-orbit split-off band as a function of the number of projectors used (with a quite small real-space grid), we see the convergence of the real space formalism to the plane wave values.

This same formalism can be applied to the calculation of any other nonlocal parts of the pseudopotential Hamiltonian. For a general nonlocal atomic potential $\delta V_l(r)$ we can form the same matrix

$$\delta\bar{V}_l(k,k') = \int r^2 dr \; j_l(kr)\delta V_l(r) j_l(k'r) \tag{2.83}$$

and solve again for the eigenvalues and eigenvectors $\{\lambda_n\}$ and $\{u_n(k)\}$ and define

$$b_n(k) = \sqrt{|\lambda_n|}u_n(k) \tag{2.84}$$

which give us that

$$\delta\bar{V}_l(k,k') = \sum_n \mathrm{sgn}(\lambda_n) b_n(k) b_n(k') \tag{2.85}$$

where here we must be careful to preserve the sign of the eigenvalues λ_n as the nonlocal potential may have both negative and positive eigenvalues.

We can then define the real-space projectors equivalently

$$\varphi_n(r) = \frac{2}{\pi}\int_0^\infty k^2 dk \; j_l(r'k) b_n(k) \tag{2.86}$$

giving a separable form for the nonlocal operator

$$\delta\hat{V}_l^{\mathrm{sep}} = \sum_n \sum_m \sum_\sigma \mathrm{sign}(\lambda_n) \left|lm\varphi_n\sigma\right\rangle \left\langle lm\varphi_n\sigma\right| \; . \tag{2.87}$$

Notably this is even easier to calculate than the spin-orbit potential as there is no mixing of spin or angular momenta components meaning all sums are only over a single set of coordinates.

2.3.3 Evaluation of numerical accuracy

There are several mutually dependent parameters that control the convergence of equation 2.72. The first parameter to consider is k_{max}, the maximum value of k or k' for which $\bar{V}_{\mathrm{SO}}(k,k')$ is calculated. This is also then the highest value of k for which the eigenfunctions $u_n(k)$ are defined, and through equation 2.79 determine the maximum frequency components in the real-space radial projectors $\phi_n(r)$.

The next important convergence parameter to consider is the number of projectors ϕ_n used in the sum. As Figure 2.5 shows, using only a few projectors can approximate the underlying matrix $\bar{V}_{\mathrm{SO}}(k,k')$ quite effectively, but the number of projectors needed for overall convergence of the real-space operator can also depend on the other convegence factors.

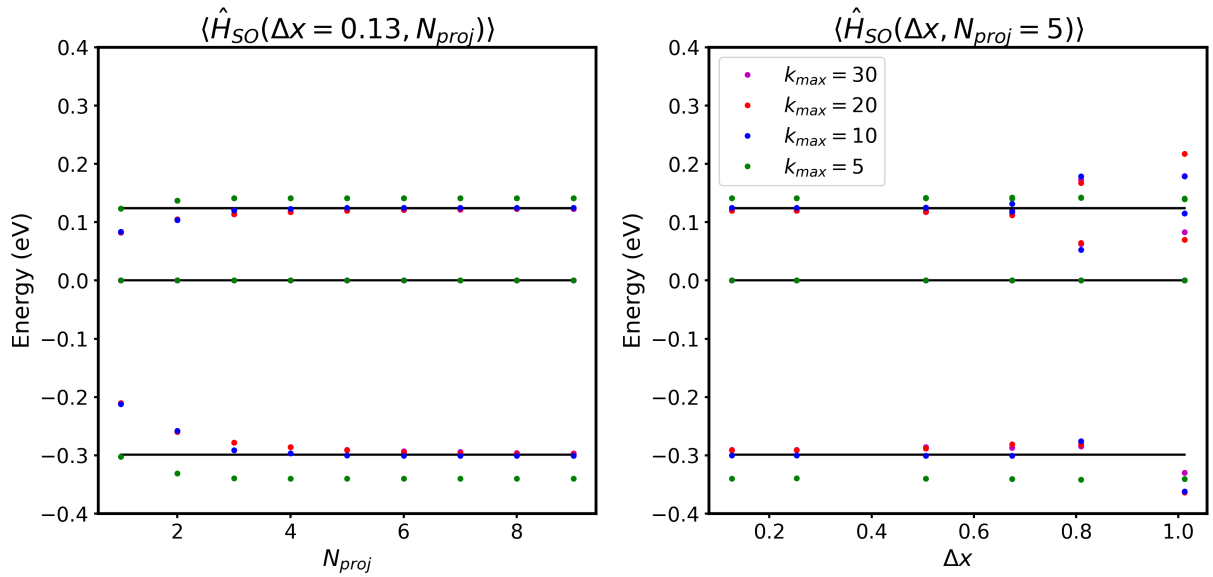

Figure 2.6: (left) The convergence of the spin orbit energy in a InAs unit cell as a function of the number of projectors used, with a constant grid spacing of 0.13 Bohr. (right) The same value as a function of the grid spacing, all using 5 projection functions. The different colored points represent the effect of adjusting the kinetic energy cutoff of the matrix $\bar{V}(k, k')$.

The good convergence of the real space calculation to the plane wave result in the unit cell calculation was only possible with a very fine real space grid. In order to perform calculations on nanocrystals of reasonable sizes, the grid spacing must be on the order of 0.5 Bohr. For the convergence between the plane wave and real space calculations, a grid spacing of ∼0.25 Bohr was required. This would obviously severely limit the potential applications of this method. The source and solution to this issue has been explored in depth in Ref. [105] where it is termed "wrap around error".

In essence, if the radial part of the projectors contains Fourier components at frequencies higher than the frequency of the real space grid, then these components will be double counted in the discrete sum over real space grid points. Thus when generating the radial part of the projectors, the $k_{\max}$ should be lower than $\frac{2\pi}{\Delta x}$. Thus for a $\Delta x \approx 0.5$ we should have a $k_{\max} \approx 10$. Applying this solution to nanocrystal calculations shows that this can be effective, introducing only a few meV of shift in energies and gaps while allowing for the use of appropriate grid spacings to study larger nanocrystals. The projector method can also be used in the plane wave bulk band structure calculations so any errors associated with a finite cutoff and number of projectors will be resolved in the band structure fitting procedure.

Chapter 3

Fitting Pseudopotentials for New Materials

The pseudopotential method presented in Chapter 2 requires specific pseudopotentials for each material to be studied. The form presented in that section is generally extremely flexible and has been adapted to a wide range of materials, but this also requires that the parameters be fit to describe each of these materials. Additionally, as was mentioned above, the parameters for a given material are often not unique, and there may be several pseudopotentials that describe a given material with associated strengths and weakness. In this chapter we will give an overview of the process through which pseudopotential parameters for a material can be determined, discuss some of the practicalities of this highly non-linear fitting process, and give a two examples of how this process has been employed to enable the study of new material systems. The description of the InAs/InP fitting is adapted with permission from Enright, M. J; Jasrasaria, D; Hanchard, M. M.; Needell, D. R.; Phelan, M. E.; Weinberg, D. *et al.* Role of Atomic Structure on Exciton Dynamics and Photoluminescence in NIR Emissive InAs/InP/ZnSe Quantum Dots *The Journal of Physical Chemistry C* **2022** *126*(17), 7576-7587.

3.1 Producing Pseudopotentials

The goal of the pseudopotential fitting process is to find a pseudopotential for the material under consideration that will reproduce the bulk material band structure. This need not be the only consideration, and early formulations of this theory took a slightly different approach. In this early realization the pseudopotentials were first approximated by enforcing a circularized approximation onto the Kohn-Sham potential from density functional theory (DFT) using the local density approximation (LDA)[39, 40]. The pseudopotentials generated this way produced strong agreement with the LDA band structures and thus inherited their flawed description of excited state energies, leading to wildly underestimated band gaps. To correct this, the pseudopotentials were allowed to vary somewhat in order to produce the

experimentally determined band gaps. Care was taken in this process to ensure that this variation was small and that the pseudopotential wave-functions still closely resembled the LDA Kohn-Sham states, just with corrected energies.

We do not take quite such careful care to compare between our pseudopotential wave functions and *ab initio* wavefunctions, but instead rely on the careful reproduction of high-quality band energies that have strong agreement with experiments. For many of the standard II-VI and II-V materials these band structures are taken from the empirical pseudopotential method [28], which fit discrete form factors to reproduce the extensive experimental characterization of these materials. For materials without such a long history of careful study, finding high-quality band structures in the literature can present a greater problem. The results of band structures calculated with DFT are often in poor agreement with experimental results, and will vary significantly based on the specific approximations employed. Adding many-body corrections to DFT calculations produces significantly better agreement with experimental results, but these results still show significant variations based on specific implementations. These variations are particularly pernicious when fitting interoperable pseudopotentials for a class of materials. As we will discuss in the examples below, it may be necessary to fit a pseudopotential for In that works both in InAs and InP, or to understand how the pseudopotential for I may need to change as $CsPbI_3$ undergoes a phase transition. In both of these cases band structures of multiple materials (or the same material in different configurations) are needed, and if these band structures are calculated at different levels of approximation then it may be impossible to disentangle the intended effect from any difference in errors between the approximations.

This makes clear an initial difficulty of this method, which is that to produce these semi-empirical pseudopotentials we must rely on computationally expensive and complicated ab inito methods, which still may not reach full agreement with experiment and may require further modification. The extent to which this further modification should be undertake introduces a degree of uncertainty into the process and potentially can only be known based on the agreement of final results with expectations. The idea scenario would be one where a consistent set of *ab initio* calculations, potentially at a quite sophisticated level to capture experimental results, and were used and the pseudopotentials were then fit to reproduce these results. In this way the pseudopotential method would give access to the electronic structures of large systems with the known level of error associated with the *ab initio* method used to generate those bands. Regardless of how band structures are obtained the pseudopotentials much be fit to reproduce them, so we now turn to consider that process.

3.2 The Fitting Algorithm

As discussed in Section 2.2, bulk band structures using the pseudopotential method are calculated using an independent electron Hamiltonian where potential energy operator is a sum of atom-centered pseudopotentials. These are parameterized by a number of independent variables to describe the local, non-local, and spin-orbit coupling parts of the potential for

each atom, which we will here call $\{a_i^\alpha\}$ as the ith parameter describing the potential around atom α. Thus the number of independent parameters to fit to may climb quite quickly. In the case of $CsPbI_3$ there were 7 independent parameters for each atom, although it was quickly determined that the parameters for Cs were not impactful on the band structure.

The band structures are generated by calculating these energy levels independently at a series of points along a given path through the first Brillouin zone of the material. This gives a set of band energies $\epsilon_n(k)$ of the nth band at point k in the Brillouin zone. These energies are then compared to those from the target band structure $E_n(k)$ and the overall quality of fit is described by a cost function $C(E_n(k), \epsilon_n(k))$ which may chosen in various to emphasize specific features of the bands and should equal 0 when $E_n(k) = \epsilon_n(k)$ for all bands and k-points. The goal of fitting is to minimize this cost function against the $\{a_i^\alpha\}$.

We have implemented this minimization using a stochastic descent based on a modification of the Metropolis algorithm. After an initial calculation the all the the parameters are modified by random step in parameter space and then the band structure is recalculated and the cost function evaluated with these new parameters. This move is then accepted or rejected with the Metropolis acceptance criterion. If the cost function at the new parameter set is lower then the move is accepted, but if the cost is higher the move is accepted with a probability

$$P(\Delta C) = \exp\{-\beta \Delta C\} \tag{3.1}$$

where ΔC is the change in the cost function and $\frac{1}{\beta}$ is the fitting "temperature". The purpose of this temperature is to allow the fitting procedure to escape shallow local minima with a depth on the order of a few times $\frac{1}{\beta}$. The appropriate range of this temperature will depend on the cost function being used and the quality of any initial guess. If the initial guess could be very far off, a low β (high "temperature") can be used to more fully explore the potential parameter space, while if the initial guess only needs minor refinement a high β can be used to focus the fitting on steps that decrease the cost function.

3.2.1 Determining Parameter Step Sizes

As discussed in previously common way to parameterize the local part of the pseudopotentials is through the reciprocal space function

$$\tilde{v}_{loc}^{\alpha}(q) = a_0^\alpha \frac{q - a_1^\alpha}{a_2^\alpha \exp\left(a_3^\alpha q^2\right) - 1} \tag{3.2}$$

where q is the reciprocal coordinate. The impact of the four fitting parameters on the band structures is non-linear and occurs over very different parameter ranges. In order to appropriately sample the parameter space it is important to correctly scale the step size used for each of the parameters. A overly large step size for one parameter might cause the fitting process to be dominated by that parameter, or an overly small step size might prevent that parameter from fully exploring the potential parameter space. Thus the relative step size for each parameter is controlled along with a global step size that is allowed to vary with

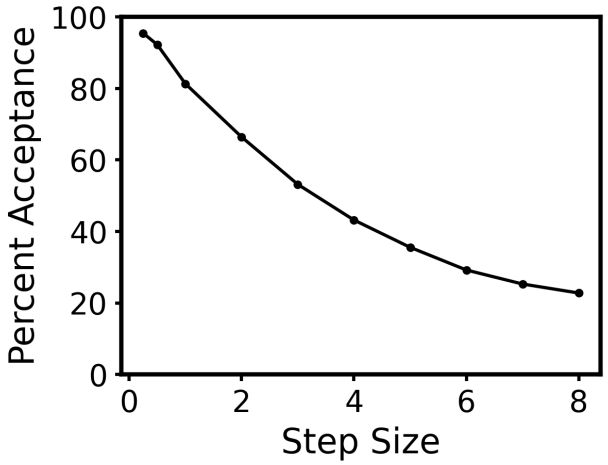

Figure 3.1: The percentage of accepted moves as a function of the paramter step size δ_0^{Pb} for the fitting of cubic $CsPbI_3$

the fitting temperature. Thus at step n, each parameter will be:

$$a_i^\alpha(n) = a_i^\alpha(n-1) + \xi \delta_i^\alpha \Delta \tag{3.3}$$

where ξ is a uniformly distributed random variable on the range $[-1, 1]$, δ_i^α is the parameter specific scaling and Δ is the global step scaling.

To determine the optimal relative parameter step size for each parameter, a fixed value of β is chosen and all of the other the parameters are fixed by setting their step sizes to zero. The sampling is then run with different step sizes for the parameter of interest, and the appropriate step size is the one that gives an acceptance of around one half. By repeating this process for all of the parameters, the relative step sizes for each can be determined.

3.2.2 Avoiding Local Minima

As alluded to earlier, the "temperature" has a significant impact on the fitting algorithm. At high temperatures the algorithm will explore the parameter space more freely, but may not fully optimize around a given local minimum, while at low temperatures the algorithm may become stuck in a local minimum. This is exemplified by the behavior in Figure 3.2, where the trajectories at different temperatures are compared to the behavior of a pure random walk where the overall displacement would grow as the square root of the distance traveled. As we see, at low temperature the fit is unable to exit an initial local minimum, while at high temperature the fit freely explores a wide parameter space without extensively optimizing. To combine these two regimes a tempering algorithm can be implemented. In this algorithm, the fitting process will switch between the high temperature and the low temperature regimes

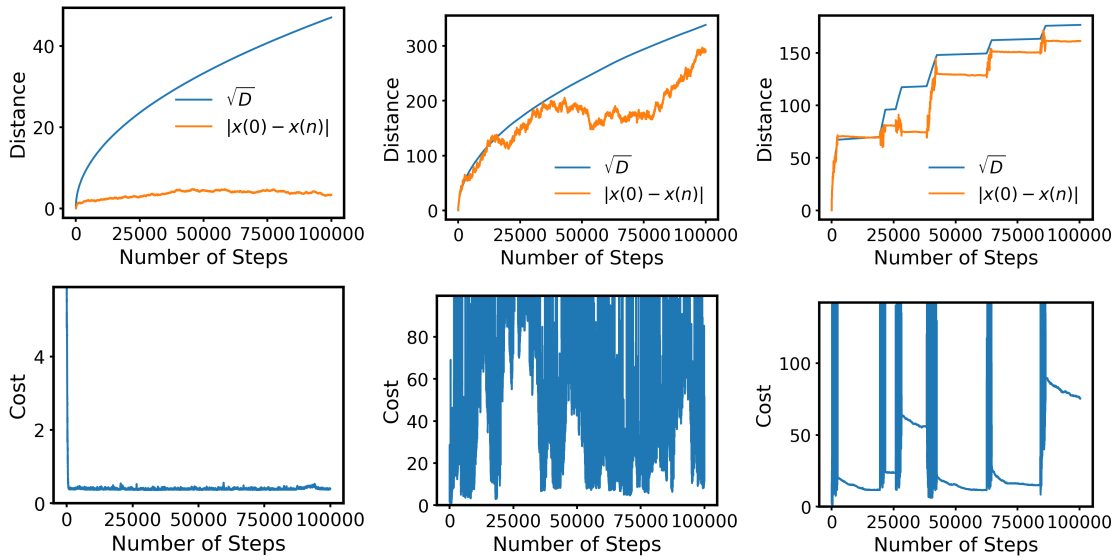

Figure 3.2: Analytics of the fitting of cubic $CsPbI_3$. On the top row, the square root of the total distance traveled, $D = \sum_{i=0}^{n-1} |x(i) - x(i+1)|$, and the distance from the starting parameters sets for three different fitting attempts. On the bottom row, the corresponding values of the cost function. On the left low temperature and small steps size ($\beta = 100$ and $\Delta = 0.01$) gets stuck in a local minimum. In the middle high temperature and large step size ($\beta = 1$ and $\Delta = 0.5$) explores the parameter space. On the right a tempering run that switches between the two regimes and hops to many local minima.

to allow for minimization within a local minimum, and exploration to other local minima. The decision to switch to a higher temperature should be made when a long series of moves at the lower temperature have failed to further decrease the cost function.

This tempering algorithm also reveals something about the nature of the cost function landscape. As we can see in the right hand column of Figure 3.2, after each period at higher temperature the fitting then relaxes quickly before plateauing, presumably near the bottom of some local minima. We can see that these are in fact all distinct local minima (even when the plateau value is very similar) as their distances from the starting point are distinct. Allows us to intuit that the fitting landscape is quite rough, and presents many local minima with a wide range of optimal costs. This type of optimization problem is extremely challenging and does not have easy solutions. It suggests that potentially greater care should be taken in picking the cost function as there may be a choice that would produce a smoother landscape with fewer local minima.

3.3 Fitting InAs/InP Band Offsets

To perform atomistic calculations on InAs/InP core/shell quantum dots (QDs) we developed a model within the semi-empirical pseudopotential method that involves fitting a single pseudopotential each for In, As, and P that reproduces accurate band structures for both bulk InAs and bulk InP [40, 106]. We used only a local potential for this work.

The bulk band structure is calculated from the reciprocal-space pseudopotentials by the direct diagonalization of the Hamiltonian within a plane wave basis over a single primitive unit cell. For both InAs and InP, the unit cells used for calculation were the standard zincblende primitive cell with axes $(0, \frac{1}{2}, \frac{1}{2})$, $(\frac{1}{2}, 0, \frac{1}{2})$, $(\frac{1}{2}, \frac{1}{2}, 0)$ in units of the lattice spacing, which was taken as 6.057 Å and 5.826 Å for InAs and InP, respectively.

The band structures depend on the 4 pseudopotential parameters for each atom via the potential energy term of the Hamiltonian. Thus, these parameters were fit simultaneously to reproduce reference InAs and InP bulk band structures, which were calculated using the discrete symmetric and anti-symmetric form factor method [28]. These band structures match well to experimental results, but they only give band energies up to an additive constant. Thus, the band offsets between the constituent materials, which are of critical importance for studying core-shell systems, must be corrected manually. We take the valence band maximum of InP to lie 0.42 eV below that of InAs [107, 108]. The sensitivity of the core-shell nanoparticle calculations to this parameter was also examined. The band offset value has an impact on the extent to which the valence band-edge hole localizes to the core InAs, with a larger band offset increasing localization, but with no significant qualitative differences.

The initial pseudopotential parameters for both InAs and InP were taken as the parameters for In and As that have been used previously [37]. From these initial parameters, band structures were calculated and compared to reference band structures using a band-weighted cost function. To optimize the fit near the band gap, the cost function was chosen to emphasize the difference between the calculated energy $\epsilon_n(k)$ of band n at point k in the first Brillouin zone and the reference energy $E_n(k)$ for the bands near the band gap. The cost function to do this is given by:

$$C = \frac{1}{N_k N_i} \sum_k \sum_{n \in 0..7} n(7-n)(\epsilon_n(k) - E_n(k))^2 \tag{3.4}$$

where N_i is the number of bands considered (8 in this case) and N_k is the number of k-points sampled. In our calculations the band gap lay between bands 3 and 4, so the cost function emphasized the contribution of those bands to the fit. Bands higher than band 7 were not included.

In this case tempering was implemented differently than discussed above. The fitting started with a short ($\sim$100 step) random walk through the 3-species parameter space. The 16 parameter sets with the lowest values of the cost function were then further refined using the Metropolis algorithm procedure described above to produce band structures that closely

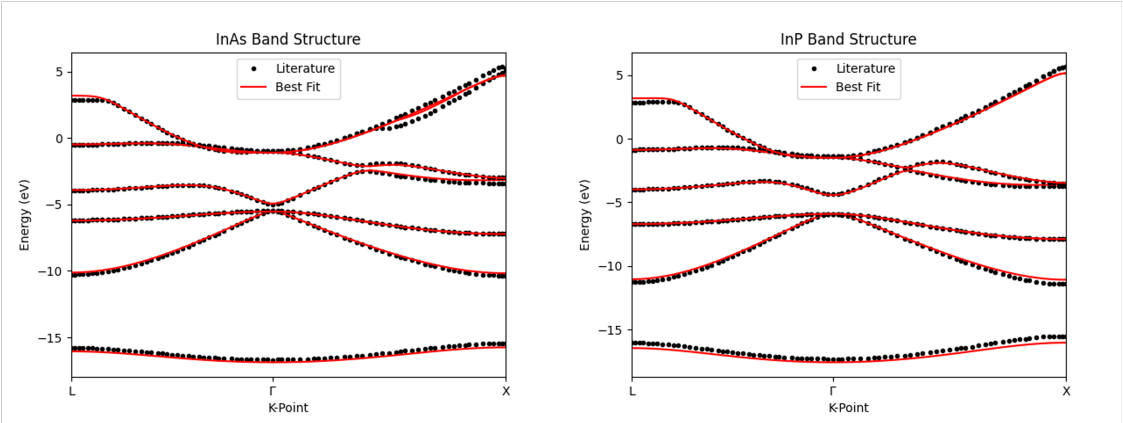

Figure 3.3: Comparison of the literature and best-fit band structures for InAs (left) and InP (right) shows strong agreement, especially near the band gap. Small deviations from the expected band structure away from the gamma point should have minimal impact on QD electronic properties, which are dominated by the behavior near the band gap.

agree with the reference. The final best-fit parameters for the pseudopotentials are collected in Table 2.1. The fit band structures match very closely to the expected band structure as seen in Figure 3.3.

3.4 Fitting Cubic and Orthorhombic $CsPbI_3$ Phases

For the $CsPbI_3$ perovskites we faced the opposite problem from the InAs/InP QDs. Here we had a material with single chemical composition, but multiple crystalline phases with distinct band structures. Not only that but the purpose of the project was to understand any impacts a change in crystal structure might have on the electronic states of perovskite nanomaterials (for more on this see Chapter 4). While for InAs/InP the goal was to find a single pseudopotential for In that would describe both band structures, it was quickly determined that separate parameters would have to be fit for both the cubic and the orthorhombic phases of $CsPbI_3$. Not only that, but the fitting in these systems required the description of spin-orbit coupling.

The introduction of spin-orbit coupling along with the larger unit cell of the orthorhombic phase of $CsPbI_3$ significantly slowed the evaluation of the band structure calculations. For the InAs/InP calculations a kinetic energy cutoff of 10 Hartree was sufficient to converge the band structure. This translated to a basis set of 900 plane wave. For the orthorhombic $CsPbI_3$, due to a significantly larger unit cell and the distinction of spin up and down compenents, a kinetic energy cutoff of only 7 Hartree translated to more than 11000 spinor plane wave basis states. This 12-fold increase in the basis set size means that determining the band energies for the perovskite systems at a given set of pseudopotential parameters

was more that 1000 times slower than for the InAs/InP. To overcome this obstacle, much of the initial fitting was carried out using a much smaller basis set and then the final refinement was taken in the converged basis set.

Additionally, this slower evaluation of band energies forced judicious choices of which k-points to evaluate the band energies at. In Figure 3.4 the 16 k-points where the fitting for the orthorhombic $CsPbI_3$ band structure was are shown. They are intentionally clustered around the high symmetry points with the hope that aligning the positions and slopes of the band crossings at these points would lead to agreement across the rest of the band structure. Special attention was taken to fit the bands at the Γ point where the band gap of the material is located. Along with placing extra fitting points in that region, each k-point was given a weight and the fit at that k-point was magnified by that weight. Furthermore, one of the stubborn issues that arose from using fewer points in the fitting was a difficulty capturing the proper effective masses of the valence and conduction bands. Thus a point near the band gap was introduced into the fitting for the sole purpose of calculating the effective massed by finite difference. The effective mass around the Γ point was calculated as:

$$m^*_{e/h} = \pm\frac{1}{2}\frac{(\Delta k)^2}{\epsilon(\Gamma) - \epsilon(\Gamma + \Delta k)}\,, \tag{3.5}$$

with the $\pm$ referring to the electron and hole effective masses. To take all of that into account, a different cost function from the InAs was used:

$$C = \frac{1}{N_k N_i}\sum_k \sum_n w(k)(\epsilon_n(k) - E_n(k))^2 + w_m[(m^*_e - M^*_e)^2 + (m^*_h - M^*_h)^2]\,, \tag{3.6}$$

where $w(k)$ refers to the weight of that k-point, w_m is the weighting of the effective mass, and $M^*_{e/h}$ refers to the expected electron and hole effective masses. These Weights are collected in table 3.1. This use of the effective masses and the weighting of the most important k-points allowed for many of the difficulties associated with the large unit cells of $CSPbI_3$ to be circumvented and produce pseudopotentials that effectively fit both the cubic and orthorhombic phases of the material.

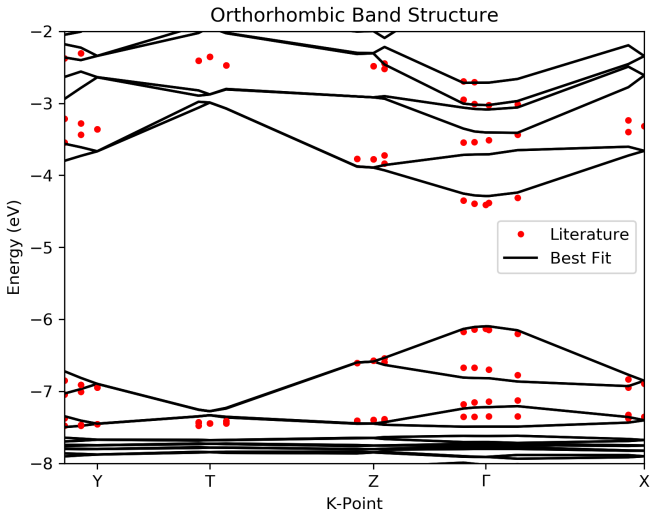

Figure 3.4: The points where the orthorhombic $CsPbI_3$ band structure was fit against.

Table 3.1: k-points and weights for fitting orthorhombic $CsPbI_3$.

k-point	k_x $(\frac{2\pi}{a_0})$	k_y $(\frac{2\pi}{a_0})$	k_z $(\frac{2\pi}{a_0})$	weight
	0.00	0.40	0.00	5
	0.00	0.45	0.00	5
Y	0.00	0.50	0.00	10
	0.00	0.50	0.45	5
T	0.00	0.50	0.50	10
	0.00	0.45	0.50	5
	0.00	0.05	0.50	5
Z	0.00	0.00	0.50	10
	0.00	0.00	0.45	5
	0.00	0.00	0.10	5
	0.00	0.00	0.05	5
Γ	0.00	0.00	0.00	100
	0.01	0.00	0.00	0
	0.10	0.00	0.00	5
	0.45	0.00	0.00	5
X	0.50	0.00	0.00	10

Chapter 4

Exciton Fine Structure in Perovskite Nanocrystals

Calculating the optical properties of perovskite nanocrystals (NCs) required the realization of the advancements to the pseudopotential method discussed in Chapter 2 to account for the highly important effects of spin-orbit coupling in these systems and the completion of the fitting process described in Chapter 3. In this chapter we develop a model that combines the atomistic determination of the structure of perovskite NCs via a force field with the pseudopotential method for electronic states. This method allows us to examine the exciton fine structure in these systems which has been a matter of debate in the field. The content of this chapter is adapted with permission from Weinberg, D.; Park, Y.; Limmer, D. T.; Rababi, E. Size-Dependent Lattice Symmetry Breaking Determines the Exciton Fine Structure of Perovskite Nanocrystals. *Nano Lett.* **2023**, *23*(11), 4997-5003.

4.1 The Impact of the Rashba Effect on Exciton Fine Structure

Lead-halide perovskite nanocrystals (NCs) have attracted significant attention due to their remarkable optical and electronic properties that could lend themselves to diverse applications [109–111]. Perhaps most interestingly, these materials show remarkably fast radiative lifetimes, which shorten at low temperatures in contrast to other nanomaterials [65, 112–117]. This anomalous temperature dependence of the radiative lifetimes has led to speculation that these materials could exhibit a reversal of the typical exciton fine structure (FS) measured in all other nanomaterials to date [21, 65, 66]. Specifically, Becker et al. [65] proposed that the lowest excitonic state is a bright state, i.e that it has an optically allowed transition to the material ground state. If that is the case, at low temperatures the carriers will preferentially be in the bright, rapidly emissive state rather than depending on thermal fluctuations to reach an emissive state. Understanding the excitonic fine structure in these materials is important to assess their suitability as quantum light sources, which depends

in part on the uniquely fast radiative lifetimes [48–51]. The argument for a bright excitonic ground state was supported by a detailed analysis of the physics of excitons in perovskite NCs from an effective mass model. We will briefly revisit this before describing our atomistic approach to this problem, which can provide a definitive ordering of bright and dark states in lead-halide perovskite NCs.

In the typical picture, electrons and holes are bound into excitons by their strong Coloumbic attraction forming a hydrogenic series of states that may be modified by confinement effects of the NC [118]. For systems with negligible spin-orbit coupling, the electron and hole spins are decoupled from the spatial degrees of freedom and simple addition of angular momentum describes the resulting triplet and singlet spin functions. The electron-hole exchange interaction slightly reduces the strength of exciton binding for excitons with spin-singlet character, introducing a spin dependence into the exciton FS. Notably, for materials like perovskites with significant spin-orbit coupling, the spatial and spin degrees of freedom are not separable. Further, it is known that the excited state properties of the perovskites are sensitive to the lattice structure, as the charge-lattice coupling in these materials is significant [119–122].

In the specific case of the perovskite NCs studied here, the conduction band is composed mainly of of Pb-6p orbitals which are strongly split by spin-orbit coupling. The conduction band edge is composed of the the $J = 1/2$ total angular momentum subspace formed from the addition of the spin and the orbital angular momentum. The valence band has s-type symmetry and thus is not split by spin-orbit coupling [123]. In the exciton, this causes the exchange interaction to split three bright states with mixed spin-triplet and spin-singlet character above a dark ground state with pure spin-triplet character. These bright states each have dipoles polarized normal to one of the nanocrystal facets, corresponding to the $\langle 100 \rangle$ family of directions in the cubic lattice and which we take as the Cartesian principle axes. For such a cubic crystalline structure these three bright states are perfectly degenerate and are often referred to as "bright triplets" due to their total angular momentum triplet character, however this should not be confused with their spin character.

Any deviation from this cubic structure will result in splitting among these bright states. Perovskite materials are known to progress through a series of symmetry lowering phase transitions as temperature is reduced [52, 53], and Figure 4.1(b) illustrates the effect of these distortions on the exciton FS. A tetragonal distortion caused by rotation of the lead-halide octahedra around the z-axis splits the z-oriented state higher in energy, but the symmetry in the x-y plane maintains the degeneracy of those two states. At lower temperatures, tilting of the octahedra breaks that symmetry and further splits the bright states in the x-y plane into two states polarized at 45° angle to the principle axes [124]. These symmetry lowering splittings are observed experimentally as a splitting of the excitonic emission into two or three distinct lines [65, 114, 125], but on their own they do not lead to a reversal of the bright-dark level ordering.

The theorized bright ground state may be arrived at through the influence of the Rashba effect [126]. This additional term in the $\mathbf{k} \cdot \mathbf{p}$ Hamiltonian comes from the co-existence of strong spin-orbit coupling and inversion symmetry breaking. The additional "effective exchange" [65] term only enters the Hamiltonian through two parameters– a magnitude and

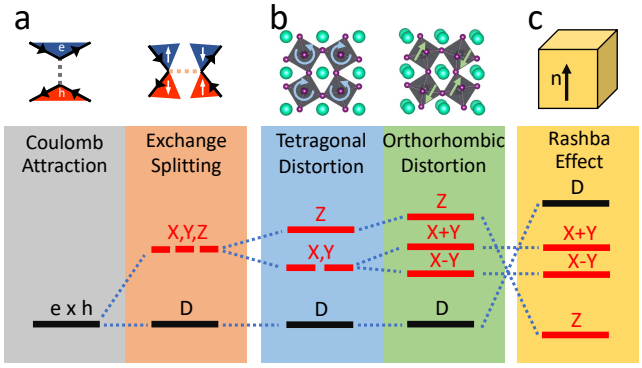

Figure 4.1: (a) The effects of electron-hole interaction, (b) lattice distortion, and (c) the previously proposed [65] role of the Rashba effect on the exciton FS.

direction along which inversion symmetry is broken. This, by nature, is blind to the atomistic detail of the symmetry breaking at the nanoscale, and leaves unknown the exact nature of a NC structure that would give rise to such a level ordering.

In fact, several recent measurements [114, 125, 127] have detected a signature of a dark ground state several meVs below the bright states. Under the influence of a external magnetic field, the Zeeman effect couples dark states to energetically close bright states, resulting in an emergent emission line. Under these conditions the dark ground state can be directly observed. The fine structure splittings are instead explained in terms of the interplay of crystal structure and NC shape anisotropy [125].

Various theoretical attempts have been made to provide additional understanding of atomistic detail of this effect, as well as provide tools to understand how to disentangle the Rashba effect, the crystal field splitting, and NC shape anisotropy to determine the level ordering and splitting in these NCs. Within an effective mass model, the Rashba splitting as indicated by the energy difference between Z and X/Y excitons is predicted to increase to the bulk limit with increasing NC size [66]. On the other hand, the effect of shape anisotropy should be lesser for larger NCs [128]. This does, however, lead to a troubling question: If the Rashba effect is more pronounced for larger NCs, but absent in the bulk, where would the transition to more bulk-like behavior occur? The resolution of this must come from an atomistic theory that can also describe how the structure of small NCs may be distorted and how that of large NCs converges to the bulk limit. These questions involving the Rashba effect have also been considered in the context of 2D layered perovskites, where theoretical studies using both phenomenological [129] and BSE-based [130] models of the electron-hole exchange interaction show that specific polar lattice distortions may be sufficient to cause a bright excitonic ground state. On the other hand, a recent theoretical investigation focusing on methylammonium lead iodide considered the effect of methylammonium relaxation within a fixed tetragonal lead iodide framework and found only weak a Rashba effect insufficient to

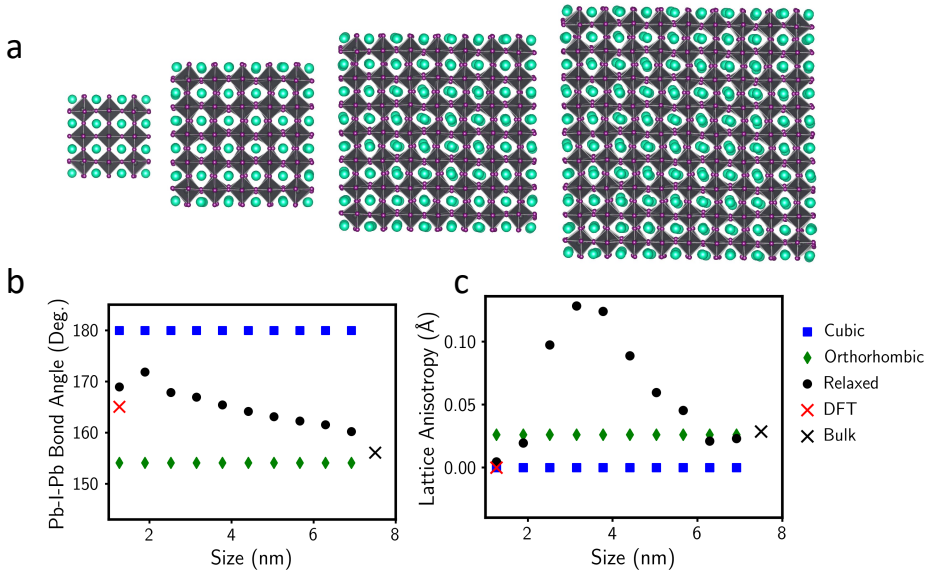

Figure 4.2: (a) Renderings of 1.9nm, 3.1nm, 4.4nm, and 5.7nm $CsPbI_3$ NC cubes after structural relaxation. Cs atoms are shown in teal, I atoms in purple and Pb are shown as grey coordination octahedra. (b) The average Pb-I-Pb bond angle and (c) the extent of lattice anisotropy induced by the relaxation for cubic (blue squares), orthorhombic (green diamonds) and relaxed (black circles) structures. Red and black x symbols represent the results from DFT calculation and bulk simulation, respectively.

cause level inversion [67].

4.2 Atomistic Structure of Perovskite NCs

To fully understand the intertwined roles of the Rashba effect and lattice symmetry we must consider the full structure of perovskite NCs in atomistic detail, especially including the lead halide framework that contributes most strongly to the valence and conduction band states. To do this, we use a previously developed atomistic force field [131] to find the lowest energy configuration for a series of $CsPbI_3$ perovskite NCs shown in Figure 4.2(a). The bulk properties of this model have been extensively validated [132, 133] and the parameters used are reproduced in Table 4.1. For each size of NC, we take the unrelaxed orthorhombic structure as an initial configuration for relaxation. However, since the corresponding structure doesn't satisfy the condition of charge neutrality, to reduce the effect from surface boundaries of NC and to stabilize the NC structure instead of having organic ligands on the surface in the experiments, relying on the fact that the electronic structure of $CsPbI_3$ perovskite is

Table 4.1: Force field parameters from Ref. [131]

	Pb	I	Cs	Cs (Surface)
q (e)	0.85	-0.57	0.86	q_{surf}
σ (Angstrom)	3.210	4.014	3.584	3.584
ε (eV)	0.001086	0.06389	0.07728	0.07728

largely determined by the lead halide octahedra. Using the force field parameters adopted from Ref. [131] which are parameterized to reproduce the energy difference between different crystal structures, the partial charge of surface Cs atoms, q_{surf}, is defined as

$$q_{\text{surf}} = -\frac{N_{\text{Pb}}\, q_{\text{Pb}} \;+\; N_{\text{I}}\, q_{\text{I}} \;+\; N_{\text{Cs}}\, q_{\text{Cs}}}{N_{\text{surf}}} \tag{4.1}$$

where q_α is a partial charge of atom α listed in Table 4.1 and N_α is the number of α atoms in each NC with $\alpha \in \{\text{Pb, I, Cs}\}$. The subscript surf is used to refer to surface Cs atoms whereas the subscript Cs indicates the core Cs atoms. With the modified initial configuration, the structure of each NC size is minimized using conjugate gradient algorithm based on the pairwise interaction u_{ij} between atom i and j described by Lennard-Jones potential with Coulombic interaction

$$u_{ij}(r) = \frac{q_i q_j}{4\pi\varepsilon_0 r} + 4\varepsilon_{ij}\left[\left(\frac{\sigma_{ij}}{r}\right)^{12} - \left(\frac{\sigma_{ij}}{r}\right)^{6}\right], \quad r < r_c \tag{4.2}$$

where $i, j \in \{\text{Pb, I, Cs, surf}\}$, ε_0 is the vacuum electric permittivity, and the cutoff distance r_c is set to be the maximum length of each NC among three different axis times $\sqrt{3}$ to take care of the fact that periodic boundary condition cannot be applied for NC. Lennard-Jones parameters ε and σ of each atom are listed in Table 4.1. Where parameters not listed can be derived using following combining rules $\varepsilon_{ij} = \sqrt{\varepsilon_i \varepsilon_j}$ and $\sigma_{ij} = (\sigma_i + \sigma_j)/2$. Minimizations were performed using the LAMMPS package [134].

A DFT structural minimization was also performed on a 1.26 nm NC using the PBE exchange correlation functional. The electronic calculation used a kinetic energy cutoff of 65 Rydbergs and a charge density cutoff of 530 Rydbergs. The structure was optimized to a force threshold of less than 10^{-4} atomic units using Quantum Espresso [135–137]. The results of this calculation show strong agreement with the structure calculated by the force field.

As the measurements of the exctionic FS occur at cryogenic temperatures, these single minimized structures accurately represent the atomic configuration of the NCs in these experiments, and the effects of lattice dynamics may be ignored. The relaxed structures can be compared to the bulk cubic and orthorhombic structures on the basis of the average Pb-I-Pb bond angles. These are shown in Figure 4.2 (b) and reveal that these relaxed structures lie somewhere between the cubic and orthorhombic structures. The cubic structures have no octahedral rotation and therefore all bond angles are 180 degrees. For the orthorhombic

structures the significant octahedral rotation leads to an average bond angle of 154 degrees. The smallest relaxed structures take more cubic forms, but the larger ones approach the orthorhombic configuration which is the stable bulk structure.

To quantify the extent to which the NC relaxation breaks crystal symmetries we define a lattice anisotropy parameter. It is defined by taking the average of the Pb-Pb distances along each of the principal axes, and then finding the difference between the direction with the lowest average and the direction with the highest average. We plot this parameter against NC size in Figure 4.2 (c). For the cubic structures this is always zero, and for the orthorhombic structures the elongated z-axis gives a small constant anisotropy. The small relaxed structures are highly symmetric so this anisotropy is near zero, but as the size increases beyond 2 nm in size, octahedral rotations begin to emerge. These are not uniform throughout the NC, however, and remain suppressed at the surface leading to significant lattice anisotropy. Significant deviation from the cubic crystal structure is not unexpected, as although cubic phase QDs have been stabilized at room temperature and somewhat below [47], the cryogenic temperatures at which the FS measurements take place should favor the orthorhombic structure. The size-dependent effect has been observed experimentally [138], and is driven by a competition between surface energy and bulk phase stability which had been previously explored using a continuum model [139]. The predicted phase crossover around 2.7 nm aligns well with the region of highest lattice anisotropy. Additionally, for both average bond angle and lattice anisotropy parameter, the results from the smallest and largest nanocrystals agree well with the results from DFT calculation and bulk CsPbI3 simulation, respectively, which lends confidence to our ability to produce an atomistic description of complex structural behavior at the nanoscale. This size dependent effect has not previously been considered in the context of the exciton FS, and will play a crucial role in understanding the size dependence of the FS splittings.

4.3 Electronic States in Relaxed NCs

Obtaining the exciton FS from these relaxed NC configurations requires an electronic structure method that is responsive to the atomistic detail of the material. While these materials are too large for *ab-initio* theories such as DFT combined with many-body perturbation techniques, semi-empirical methods are able to access the size ranges necessary. We employ the semi-empirical pseudopotential method [10, 30, 31, 42], which assigns each atom in the NC an effective potential derived from bulk band structures. These pseudopotentials include both local and non-local components that capture the effect of spin-orbit coupling. As our relaxed NCs lie somewhere in between the cubic and orthorhombic crystal phases, pseudopotentials have been fit to describe the band structures of both phases individually. The pseudopotentials used in the NC calculations are linearly interpolated between these, based on the local NC structure. This way, the electronic structure is sensitive to local deformations or distortions in the lattice. The optical absorption spectrum is computed using the Bethe-Salpeter equation (BSE) within the static screening approximation, which describes

the bound excitonic states in the basis of free electron-hole pairs [63, 94]. This approach allows for equal treatment of the direct and exchange terms in a non-perturbative manner, and fully takes into account the effects of spin-orbit coupling. This treatment is essential to determining the full excitonic spectrum of these NCs and the FS splitting.

As discussed in Chapter 2, the electronic Hamiltonian is a single electron operator

$$\hat{H} = \hat{T} + \sum_{\alpha}^{\text{atoms}} \left[\hat{V}_{loc}^{\alpha} + \hat{V}_{nonloc}^{\alpha} + \hat{V}_{SO}^{\alpha} \right] \tag{4.3}$$

where $\hat{T}$ is the kinetic energy operator, $\hat{V}_{loc}^{\alpha}$ is the local part of the pseudopotential around atom α, $\hat{V}_{nonloc}^{\alpha}$ describes angular momentum-dependent corrections to the local pseudopotential around atom α, and $\hat{V}_{SO}^{\alpha}$ describes the spin orbit coupling around atom α. The local part of the potential is defined in by a reciprocal space function

$$\tilde{v}_{loc}^{\alpha}(q) = a_0^{\alpha} \frac{q - a_1^{\alpha}}{a_2^{\alpha} \exp\left(a_3^{\alpha} q^2\right) - 1} \tag{4.4}$$

where q is the reciprocal coordinate, and the parameters $a_0^{\alpha} \ldots a_3^{\alpha}$ are fit based on the atom α and are listed in Table 4.2. The potential is defined in terms of the position-space counterpart of $\tilde{v}_{loc}^{\alpha}(q)$, which we call $v_{loc}^{\alpha}(r)$. The local part of the potential is given by

$$\hat{V}_{loc}^{\alpha} = v_{loc}^{\alpha}\left(|\hat{\boldsymbol{r}} - \boldsymbol{R}_{\alpha}|\right) \tag{4.5}$$

where $\hat{\boldsymbol{r}}$ is the position operator, $\boldsymbol{R}_{\alpha}$ is the position of atom α. The angular momentum-dependent part of the pseudopotential gives a correction to the local part of the pseudopotential for the electrons in p-type orbitals.

$$\hat{V}_{nonloc}^{\alpha} = \delta v_{l=1}^{\alpha}\left(|\hat{\boldsymbol{r}} - \boldsymbol{R}_{\alpha}|\right) \hat{P}_{l=1}^{\alpha} = \left[a_4^{\alpha} \exp\left(-|\hat{\boldsymbol{r}} - \boldsymbol{R}_{\alpha}|^2\right) + a_5^{\alpha} \exp\left(-\left(|\hat{\boldsymbol{r}} - \boldsymbol{R}_{\alpha}| - \rho\right)^2\right)\right] \hat{P}_{l=1}^{\alpha} \tag{4.6}$$

where $\hat{P}_{l=1}^{\alpha}$ is the projector onto the $l = 1$ angular momentum subspace around atom α, ρ is a shift of 1.5 Bohr, and the a_4^{α} and a_5^{α} parameters are fit based on atom α. The spin-orbit coupling acts only on the p-type orbitals as well and has the form

$$\hat{V}_{SO}^{\alpha} = v_{SO}^{\alpha}\left(|\hat{\boldsymbol{r}} - \boldsymbol{R}_{\alpha}|\right) \hat{\boldsymbol{L}}^{\alpha} \cdot \hat{\boldsymbol{S}} \hat{P}_{l=1}^{\alpha} = a_6^{\alpha} \exp\left(\frac{-|\hat{\boldsymbol{r}} - \boldsymbol{R}_{\alpha}|^2}{w^2}\right) \hat{\boldsymbol{L}}^{\alpha} \cdot \hat{\boldsymbol{S}} \hat{P}_{l=1}^{\alpha} \tag{4.7}$$

where $\hat{\boldsymbol{L}}^{\alpha}$ is the vector of electron orbital angular momentum operators around atom α, $\hat{\boldsymbol{S}}$ is the vector of electron spin operators, w is a width of 0.7 Bohr and a_6^{α} is fit based on atom α. The total potential can be rewritten as three separate, spherically symmetric potentials felt by s-type (along with d-type and higher angular momentum) orbitals, $p_{\frac{1}{2}}$-type orbitals and $p_{\frac{3}{2}}$-type orbitals. The s-type orbitals feel the local potential only:

$$v_s(r) = v_{loc}^{\alpha}(r) \tag{4.8}$$

The $p_{\frac{1}{2}}$-type orbitals feel a combination of the angular momentum dependent potential and the spin-orbit potential

$$v_{p_{\frac{1}{2}}}(r) = v^{\alpha}_{loc}(r) + \delta v^{\alpha}_{l=1}(r) - v^{\alpha}_{SO}(r) \tag{4.9}$$

while the $p_{\frac{3}{2}}$-type orbitals feel a different combination

$$v_{p_{\frac{3}{2}}}(r) = v^{\alpha}_{loc}(r) + \delta v^{\alpha}_{l=1}(r) + \frac{1}{2} v^{\alpha}_{SO}(r) \tag{4.10}$$

The single particle Hamiltonian was solved via the filter diagonalization method [61, 62] on a real-space grid with a grid spacing of 0.5 Bohr. This finer grid spacing was used to ensure sufficient convergence of the non-local parts of the Hamiltonian. The non-local operators were implemented via a modified Kleinman-Bylander representation [104, 105, 140]. On the order of a few hundred states in the energy range near the band gap were converged.

The pseudopotential parameters were fit for each atom in a particular crystal structure in order to reproduce bulk band structures. For the perovskite system we are investigating here, we generated best fit parameter sets for both the cubic and the orthorhombic crystal structures. The best fit was determined by using the pseudopotential Hamiltonian within a converged plane-wave basis to generate the bulk band structures of the respective phases, with care taken to properly describe the non-local and spin-orbit interactions [30, 35, 69, 70]. These pseudopotential band structures were then compared to literature GW band structures [141]. In order to better compare with experimental results, the band gap of the GW calculations for the cubic structure, which differed significantly from measurements of the bulk band gap, was corrected by a static shift of the valence band. The GW calculations of the orthorhombic band structure agreed with experiment and were used without modification. The valence band offsets between the cubic and orthorhombic phase were calculated from DFT using Quantum Espresso [135, 136].

The seven pseudopotential parameters per atom were fit for each phase using a Monte-Carlo fitting procedure where the objective function emphasized the closeness of fit around the band gap as well as the effective mass of the bands at the gaps. The parameter space was extensively searched to find the best parameters. Initial fitting showed that contribution from the Cs ion was nearly zero, consistent with the understanding across lead halide perovskite materials that the valence and conduction bands are composed mainly of lead and halide orbitals [123]. Thus the potential around the Cs atoms was set to zero and the fits were further refined considering only the lead and iodine parameters.

The results of the fitting are shown in Figure 4.3. The orthorhombic band structure generated from our pseudopotentials has a hole effective mass of 0.320 m_e and an electron effective mass of 0.386 m_e. The cubic band structure generated from our pseudopotentials has a hole effective mass of 0.289 m_e and an electron effective mass of 0.309 m_e. These slightly overestimate the masses of the literature structures, leading to some small additional confinement effects in the NCs.

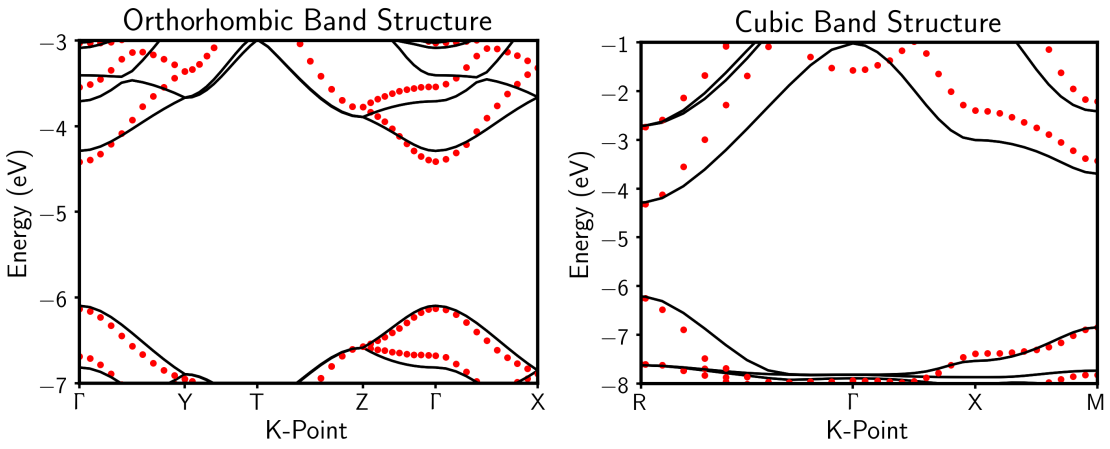

Figure 4.3: The band structures generated by the pseudopotential method (black lines) and the literature band structures (red points).

For relaxed nanocrystal structures, there is no bulk phase that perfectly matches the nanocrystal structure. This requires that the pseudopotential around each atom adapt to the local structure. We do this by linearly interpolating between the pseudopotentials for the cubic and orthorhombic structures. The relaxed nanocrystal Hamiltonian is then

$$\hat{H} = \hat{T} + \sum_{\alpha}^{\text{atoms}} (x_\alpha) \left[\hat{V}_{loc}^{\alpha,\text{ortho}} + \hat{V}_{nonloc}^{\alpha,\text{ortho}} + \hat{V}_{SO}^{\alpha,\text{ortho}}\right] + (1 - x_\alpha) \left[\hat{V}_{loc}^{\alpha,\text{cubic}} + \hat{V}_{nonloc}^{\alpha,\text{cubic}} + \hat{V}_{SO}^{\alpha,\text{cubic}}\right] \tag{4.11}$$

where $x_\alpha \in [0, 1]$ denotes the extent of orthorhombic distortion. For iodine atoms bonded to two lead atoms this was determined by the Pb-I-Pb bond angle, θ_α. Lead atoms were assigned the average of the distortion parameters of the six bonded iodine atoms. For the cubic phase the Pb-I-Pb bond is straight, $\theta = 180°$ while for the orthorhombic phase there are two bond angles of $\theta_\alpha = 150.8°$ and $\theta_\alpha = 160.6°$. Thus the orthorhombic distortion was calculated as

$$x_\alpha = \frac{180 - \theta_\alpha}{180 - 160.6} \tag{4.12}$$

where if the angle was less than 160.6 degrees the atom was assigned a fully orthorhombic pseudopotential. Iodine atoms not bonded to two lead atoms (dangling iodine at the surface) were assigned the cubic pseudopotential. It is important to note that for the local part of the pseudopotential, $\hat{V}_{loc}$, a linear interpolation between the orthorhombic and cubic operators does not mean a linear interpolation of the parameters listed in Table 4.2.

The linear interpolation was deemed reasonable based on the closeness of the pseudopotentials for the cubic and orthorhombic phases, as shown in Figure 4.5.The choice of the Pb-I-Pb bond angle as the key parameter for interpolation was motivated by the observed relaxation effects consisting mainly of octahedral rotations and tilts, which are well-parameterized

Table 4.2: Best pseudopotential parameters, in Hartree atomic units.

Iodine	Orthorhombic	Cubic
a_0	117.89162750	113.75644925
a_1	2.12591587	2.14135468
a_2	2.91148249	2.84227140
a_3	0.58243028	0.56706414
a_4	0.16631532	0.04515637
a_5	-0.02486412	0.00220169
a_6	2.23037552	3.03441874

Lead	Orthorhombic	Cubic
a_0	97.86083166	88.83030750
a_1	2.25710305	2.60529157
a_2	3.71951773	4.28692327
a_3	0.55872538	0.51950186
a_4	1.40412238	1.06405744
a_5	-0.01566674	-0.00808029
a_6	7.94721141	7.78990812

by these bond angles. This simple parameterization is not sensitive to all possible lattice distortions, such as changes to Pb-I bond length without bond angle changes, but such distortions are not significant in the relaxed structures we consider. To ensure that this interpolation did not cause significant issues with with electronic structure, band structures were calculated using unit cells with distortions between those of the cubic and orthorhombic structures. The energies of the valence and conduction band edges from these calculations are shown in Figure 4.4 as the structure is distorted from the cubic to the orthorhombic form. Because the orthorhombic structure differs from the cubic structure only by slight rotations of the lead-iodide octahedra it was simple to construct such structures and calculate their band structures both using the interpolated pseudopotentials and DFT, again within the Quantum Espresso [135, 136] package. The DFT results are known to significantly underestimate the band gap of the cubic structure, but our pseudopotential method, being trained on the corrected band structures, is able to match much better to experimental results at the end-points. The interpolated pseudopotentials generate non-monotonic trend in the band gap with overall a slight decrease in the band gap over the sequence of structures from cubic to orthorhombic, while the DFT shows a monotonic increase. However, the DFT increase seems to stem only from the previously mentioned underestimation of the band gap in the cubic phase. Without resorting to extremely computationally costly techniques like GW, we are satisfied that the pseudopotentials are able to smoothly interpolate between the cubic and orthorhombic phases without issue.

The impact of the choice of interpolation scheme was further assessed by considering the extreme case of no interpolation at all. The optical properties NCs with relaxed crystals structures were calculated using either exclusively the cubic or orthorhombic pseudopotentials. In Figure 4.6 we show the that the impact of the interpolation on the optical gap serves to simply bring the gaps of relaxed NCs in line with experiments with no impact on the splitting of dark and bright excitons and only a minor impact on the splitting between bright excitons. This strongly suggests that even a more detailed treatment of the interpolation would not have an impact on our results.

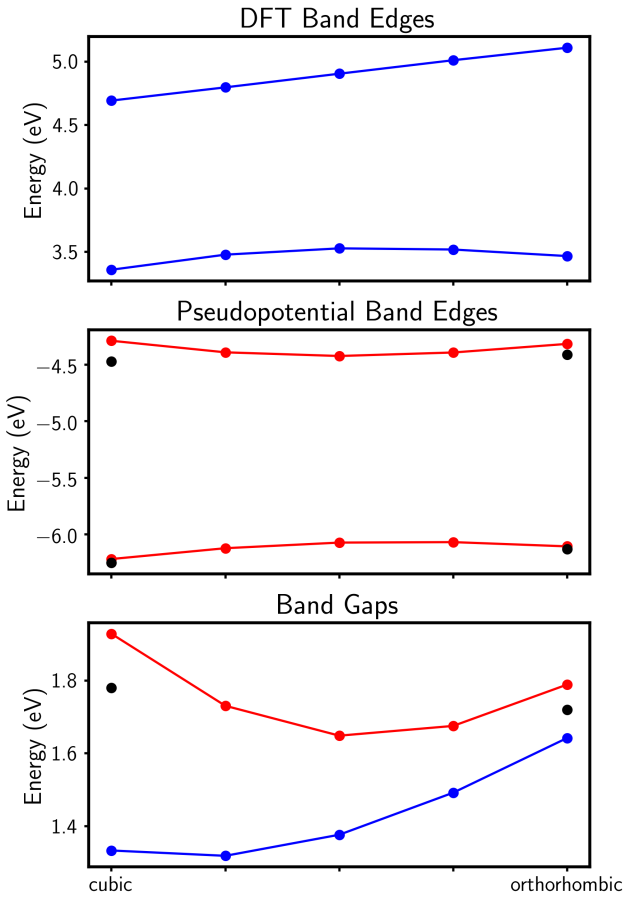

Figure 4.4: Comparison of DFT (blue) and pseudopotential (red) band edges in bulk structures interpolated between the cubic and orthorhombic phases.

4.4 Optical Properties of Perovskite NCs

The excitonic states were calculated using the Bethe-Salpeter equation (BSE) within the Tamm-Dancoff approximation, which writes the excitonic states as linear combinations of non-interacting electron-hole pair states [63]. The nth excitonic state, $|\psi_n\rangle$, is written as

$$|\psi_n\rangle = \sum_{ai} c^n_{a,i} \, |a, i\rangle \tag{4.13}$$

where the indices $a, b, c, \ldots$ refer to electron (unoccupied) states, and the indices $i, j, k, \ldots$ refer to hole (occupied) states, $|a, i\rangle$ refers to the non-interacting pair state, and the expansion coefficients, $c^n_{a,i}$, are determined by the eigenvalue equation

$$(E_n - \Delta\varepsilon_{a,i}) \, c^n_{a,i} = \sum_{bj} \left(K^d_{ai;bj} + K^x_{ai;bj} \right) c^n_{b,j} \tag{4.14}$$

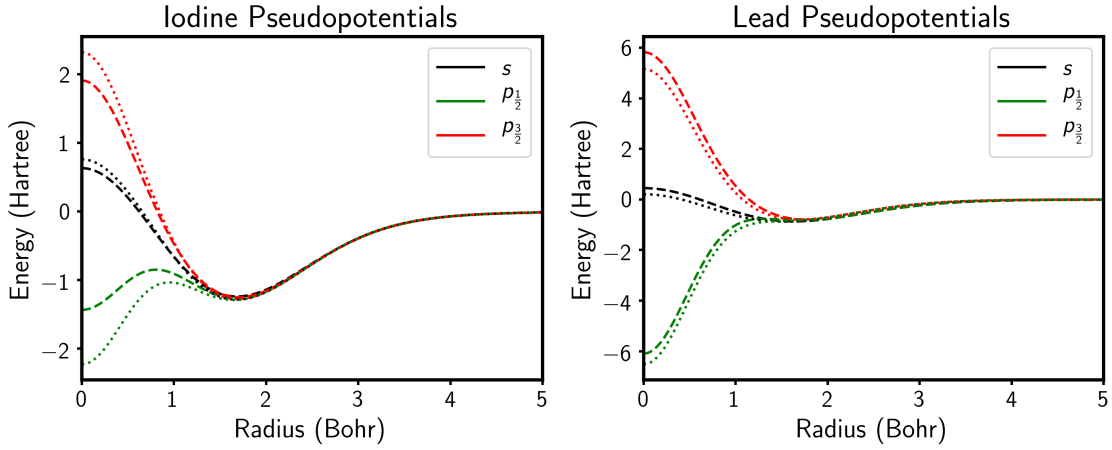

Figure 4.5: Pseudopotentials for iodine and lead atoms in the cubic (dotted lines) and orthorhombic (dashed lines).

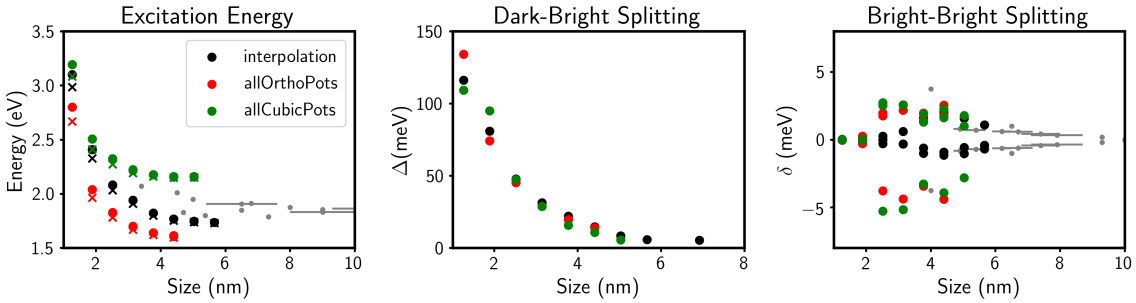

Figure 4.6: (top) The lowest optical excitations for NCs with a relaxed crystal structure, but either using the interpolated pseudopotentials (black) or only the orthorhombic or cubic pseudopotentials (red and green respectively). (middle) The splitting between the lowest dark and bright excitonic states for the same calculations. (bottom) The splitting among the three lowest bright excitonic states for the same calulations.

which also determines the energy of the nth excitonic state E_n. The electron hole interaction kernel, which describes the binding of the independent electron-hole states into correlated excitonic states, has two parts: the direct interaction K^d describes the coulomb attraction between the electron-hole pair, while the exchange interaction K^x controls the details of the excitonic spectrum, crucially including the singlet triplet splitting under consideration here. The direct interaction is calculated using a screened coulomb interaction $W\left(|\boldsymbol{r}-\boldsymbol{r'}|\right)$ within a static screening approximation as:

$$K^d_{ai;bj} = -\int d\boldsymbol{x}d\boldsymbol{x'}\phi^*_a\left(\boldsymbol{x}\right)\phi^*_j\left(\boldsymbol{x'}\right)W\left(|\boldsymbol{r}-\boldsymbol{r'}|\right)\phi_i\left(\boldsymbol{x'}\right)\phi_b\left(\boldsymbol{x}\right)\,, \tag{4.15}$$

where the integrals over $\boldsymbol{x}=(\boldsymbol{r},\sigma)$ index over both the position and spin degrees of freedom. The static dielectric constant used in the calculation is $\epsilon = 6.1$ [142]. The exchange interaction is calculated with the bare coulomb interaction $v\left(|\boldsymbol{r}-\boldsymbol{r'}|\right)$ to be

$$K^x_{ai;bj} = \int d\boldsymbol{x}d\boldsymbol{x'}\phi^*_a\left(\boldsymbol{x}\right)\phi^*_j\left(\boldsymbol{x'}\right)v\left(|\boldsymbol{r}-\boldsymbol{r'}|\right)\phi_b\left(\boldsymbol{x'}\right)\phi_i\left(\boldsymbol{x}\right) \tag{4.16}$$

This form of the exchange interaction does not distinguish between the so-called short-range and long-range exchange terms, but includes both on equal footing [143]. Note that due to the integrals over spin, the exchange interaction only couples excitons with spin-allowed electron-hole overlap. The interaction kernel matrices are solved in the basis of band-edge states. The binding energy of the nth excitonic state, E^n_{B}, is calculated as

$$E^n_{\mathrm{B}} = \left\langle \hat{K}^d + \hat{K}^x \right\rangle_n = \sum_{abij}\left(c^n_{a,i}\right)^*\left(K^d_{ai;bj}+K^x_{ai;bj}\right)c^n_{b,j}. \tag{4.17}$$

Generally 60-80 electron states and a similar number of hole states were selected to form the basis for solving the BSE, which were sufficient to converge the excitonic fine structure for the low energy states under consideration here.

We can evaluate the success of this method by comparing the computed optical gaps to a wide range of experimental results. In Fig. 4.7(a) we show the lowest excitonic states (dark and bright) of the relaxed NCs across a range of sizes. The excitation energies for the cubic and orthorhombic structures are plotted in Fig. 4.8, and show a strong agreement with experimental PL measurements [47, 144, 145, 147, 148]. The relaxed structures show a stronger confinement effect, with the smallest NCs having higher excitation energies than the other structures due to the effects of relaxation on the angles between lead halide octahedra. The smallest relaxed structures differ significantly from either the cubic or orthorhombic geometries, and this forces the electron and hole quasiparticle states further apart in energy, opening the optical gap. For the larger NCs, the effect is the opposite as the optical gaps fall somewhat below that of the other structures and experiments. This can be understood through the simple bonding and anti-bonding picture of the bulk lead halide perovskites band structure. In the bulk, the upper valence band consists of antibonding states between Pb-6s

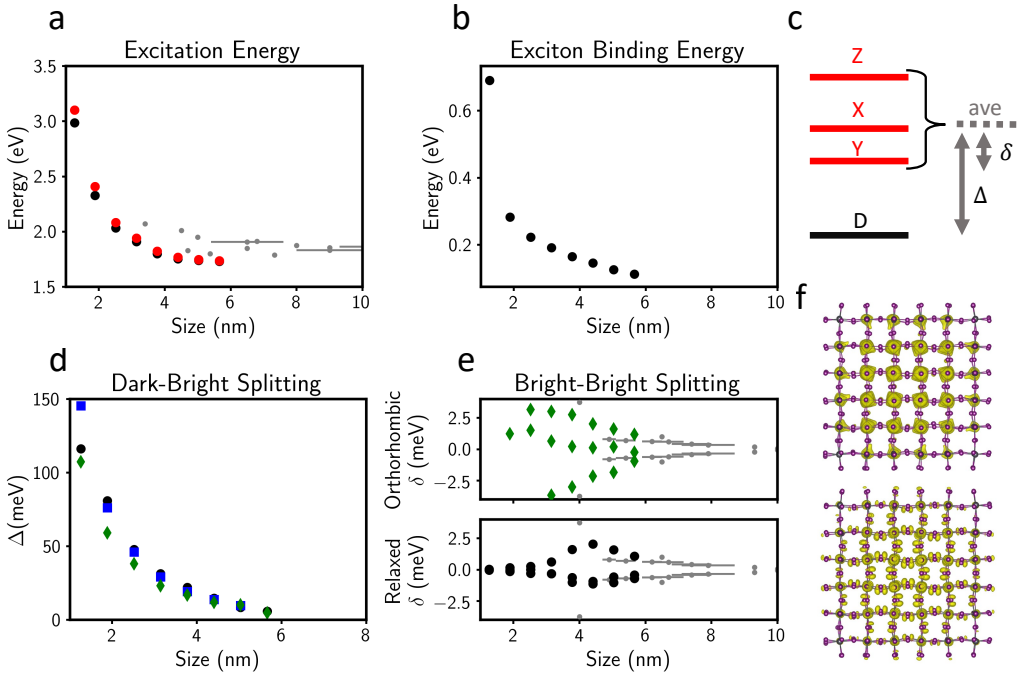

Figure 4.7: (a) The lowest bright (red) and dark (black) excitonic states for relaxed NCs as a function of size along with experimental data [47, 144–148]. (b) Exciton binding energies ignoring dielectric confinement effects [149, 150] for relaxed NCs as a function of size. (c) A level diagram describing the splittings calculated. (d) Calculated splitting between the bright and dark excitonic states. (e) Splitting among the bright excitonic states for orthorhombic (top, green diamonds) and relaxed (bottom, black circles) NCs with experimental splittings [117, 124, 151, 152]. (f) Electron density plots for the HOMO (bottom) and LUMO (top) states.

and I-5p orbitals, and the lower conduction band consists of antibonding states between Pb-6p and I-5p orbitals, dominated by the Pb-6p orbitals [123, 153, 154].

In the NCs the hole and electron quasi-orbitals (shown in Figure 4.7(f)) maintain much of their bulk character. For the smallest relaxed NCs, the Pb-I bond lengths are at a maximum, decreasing their antibonding interaction and lowering the valence band energy. The Pb-Pb distance is also exceptionally long lessening their interaction and pushing the conduction band higher in energy. This distortion changes character once the NCs pass the critical threshold of 3-4 nm in length where octahedral tilting brings the Pb atoms closer together, and the decreased Pb-I-Pb bond angle somewhat lessens the antibonding interaction. This brings the valence band quasiparticle energies into line with those of the orthorhombic structures, but the decreased Pb-Pb distances still drive the conduction band to fall below that of the fully orthorhombic structures.

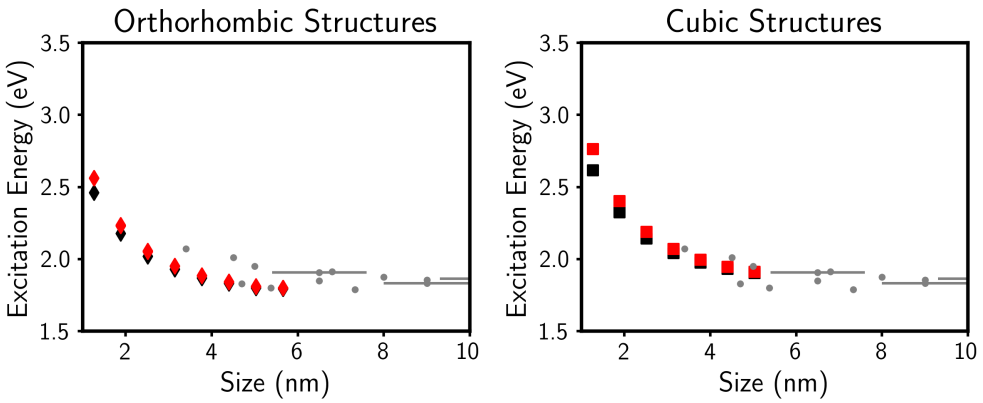

Figure 4.8: The lowest bright (red) and dark (black) excitonic states for NCs with orthorhombic and cubic structures as a function of size along with experimental data [47, 144–146, 148].

While the relaxation has some impact on the overall excitation energies, Figure 4.7(d) shows that it has little to no impact on the splitting between dark and bright states. For the cubic, orthorhombic and relaxed structures studied, the ground state exciton remains dark up to 6nm NCs, and the trend with increasing size shows that a positive dark-bright splitting is expected for all sizes of NCs. This is consistent with the recent calculations by Biffi et al. [67] which considered $MAPbI_3$ NC with atomistic electronic theory while only allowing relaxation of the MA cations. We find that expanding the relaxation to the lead halide octahedral backbone does not result in a level inversion and does not support a strong Rashba effect in these materials. If either relaxation, or the enforcement of an orthorhombic crystal structure caused a significant Rashba effect, then the dark-bright splitting would be qualitatively different from that of the cubic structures which always have inversion symmetry and thus no Rashba effect.

A deeper understanding of the exciton fine structure can come from investigating the spin statistics of the lowest excitonic states. While the total spin $\hat{S}^2_{tot} = \left(\hat{\boldsymbol{S}}_e + \hat{\boldsymbol{S}}_h\right)^2$ need not be a good quantum number, the expectation value of the total spin will still be indicative of the degree of spin-singlet versus spin-triplet character. The effect of the exciton spin on the exchange interaction is the key factor in energetically separating spin singlet and triplet states. The exciton spin operator is the sum of the electron and hole spin operators,

$$\hat{\boldsymbol{S}}_{\text{tot}} = \hat{\boldsymbol{S}}_{\text{e}} + \hat{\boldsymbol{S}}_{\text{h}} \tag{4.18}$$

The total spin of an excitonic state can be calculated as,

$$\langle\psi_n|\,\hat{S}^2_{\rm tot}\,|\psi_n\rangle = \langle\psi_n|\,\hat{S}^2_{\rm e} + \hat{S}^2_h + 2\hat{\boldsymbol{S}}_{\rm e}\cdot\hat{\boldsymbol{S}}_{\rm h}\,|\psi_n\rangle \tag{4.19}$$

$$= \sum_{ai;bj} c^n_{bj}\,(c^n_{ai})^*\,\langle a,i|\left(\hat{S}^2_{\rm e+} + \hat{S}^2_{\rm h} + 2\hat{\boldsymbol{S}}_{\rm e}\cdot\hat{\boldsymbol{S}}_{\rm h}\right)|b,j\rangle \tag{4.20}$$

$$= \sum_{ai;bj} c^n_{bj}\,(c^n_{ai})^*\left(\langle a|\,\hat{S}^2_{\rm e}\,|b\rangle\,\delta_{ij} + \langle i|\,\hat{S}^2_{\rm h}\,|j\rangle\,\delta_{ab} + 2\,\langle a|\,\hat{\boldsymbol{S}}_{\rm e}\,|b\rangle\cdot\langle i|\,\hat{\boldsymbol{S}}_{\rm h}\,|j\rangle\right) \tag{4.21}$$

$$= \sum_{ai;bj} c^n_{bj}\,(c^n_{ai})^*\left(3/4\delta_{ab}\delta_{ij} + 3/4\delta_{ij}\delta_{ab} + 2\,\langle a|\,\hat{\boldsymbol{S}}_{\rm e}\,|b\rangle\cdot\langle i|\,\hat{\boldsymbol{S}}_{\rm h}\,|j\rangle\right) \tag{4.22}$$

$$= 3/2 + 2\sum_{ai;bj} c^n_{bj}\,(c^n_{ai})^*\,\langle a|\,\hat{\boldsymbol{S}}_{\rm e}\,|b\rangle\cdot\langle i|\,\hat{\boldsymbol{S}}_{\rm h}\,|j\rangle \tag{4.23}$$

Importantly, the spin of the hole states must be treated as that of time-reversed electronic states, meaning that while the electron spin matrix elements are simply,

$$\langle a|\,\hat{\boldsymbol{S}}_{\rm e}\,|b\rangle = \frac{1}{2}\,\langle a|\,\hat{\boldsymbol{\sigma}}\,|b\rangle \tag{4.24}$$

the hole spin matrix elements are given by

$$\langle i|\,\hat{\boldsymbol{S}}_{\rm h}\,|j\rangle = \frac{1}{2}\left[\langle i|\,\hat{\Theta}^\dagger\right]\hat{\boldsymbol{\sigma}}\left[\hat{\Theta}\,|j\rangle\right] \tag{4.25}$$

$$= -\frac{1}{2}\,\langle j|\,\hat{\boldsymbol{\sigma}}\,|i\rangle \tag{4.26}$$

where $\hat{\boldsymbol{\sigma}}$ is the vector of Pauli spin matrices.

As shown in Figure 4.9, the total spin expectation value for the dark states is very close to 2, the value for a triplet state. The bright states have lower total spin, close to the value of $\frac{4}{3}$ predicted by effective mass theory [66, 128], indicative of a significant spin-singlet character. The implications of this can be understood through the expectation values of the exchange interaction for each of the states. Only the bright states, with their partial spin-singlet character, feel the effects of exchange. This spin structure is present in all the structures we consider, ensuring a dark excitonic ground state regardless of structural relaxation.

The crystal structure does, however, have a significant impact on the splitting among the bright states as seen in Figure 4.7(e). The cubic structures are not shown as the bright levels are always degenerate. Considering the orthorhombic structures, the bright-bright splitting decreases with increasing NC size, contrary to the predictions of a model where the Rashba effect is sufficiently strong to cause a bright-dark inversion [66]. What is observed is consistent with a simple crystal-field splitting that would approach the bulk at large NC sizes [155, 156]. The relaxed crystal structures are where we would expect to see signatures of the Rashba effect emerge if it was present, as the ions are allowed to relax and could strongly break inversion symmetry. These signatures are not present, and the complex behavior that we do see in the bright-bright splittings is due to the NC size dependent structural transition

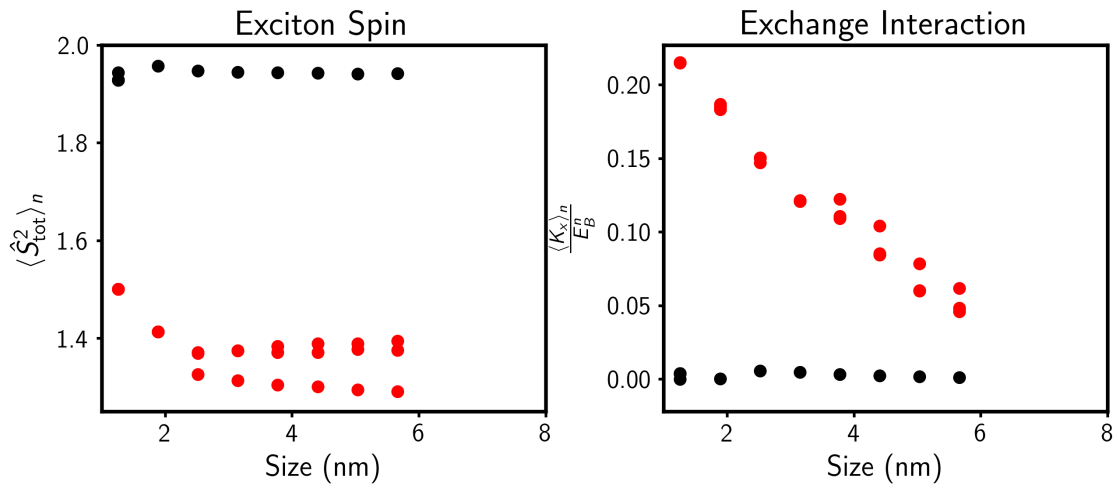

Figure 4.9: The total spin expectation value (left) and the exchange energy as a fraction of the total exciton binding energy (right) for the lowest dark (black) and bright (red) excitonic states in relaxed NCs as a function of size.

discussed earlier. The smallest NCs have more symmetric structures and thus smaller bright-bright splittings. For the larger NCs the structures become nearly orthorhombic and thus the splittings resemble those of the orthorhombic NCs. Both of these splittings match well to experiments [114, 117, 124, 151, 152], although the lack of data for extremely small NCs make the predictions of the relaxed structures difficult to verify. Additional measurements of the exciton FS in extremely small perovskite NCs could help resolve questions of the structure of these smallest clusters.

The polarization dependent emission spectra can also be calculated from our atomistic theory. Simulated spectra were calculated from the oscillator strengths of the transition from each excitonic state to the ground state. These spectra are shown in Figure 4.10 for NCs of various crystal structures all with 3.8 nm edge lengths.

$$f_{(x,y,z)}(E) = \sum_n \delta(E - E_n) \sum_{ai} c^n_{a,i} \left| \langle i | \hat{\mu}_{(x,y,z)} | a \rangle \right|^2 \tag{4.27}$$

where $c^n_{a,i}$ are the BSE expansion coefficients for electron state $|a\rangle$ and hole state $|i\rangle$ into excitonic state n with energy E_n. The dipole operator $\hat{\mu}_{x,y,z}$ is broken down along the three principal axes as shown in color in Figure 4.10, and the average of the three polarizations is used for the total spectrum shown as the black line in Figure 4.10. In agreement with the effective mass models, we observe only one peak for the cubic structure, lying around 20 meV above a dark ground state. For the orthorhombic structure, the splittings due to lattice distortion are clearly recovered and the polarization of the lower two excitonic states is aligned with the orthorhombic crystal axes rather than the faces of the NC, also in agreement

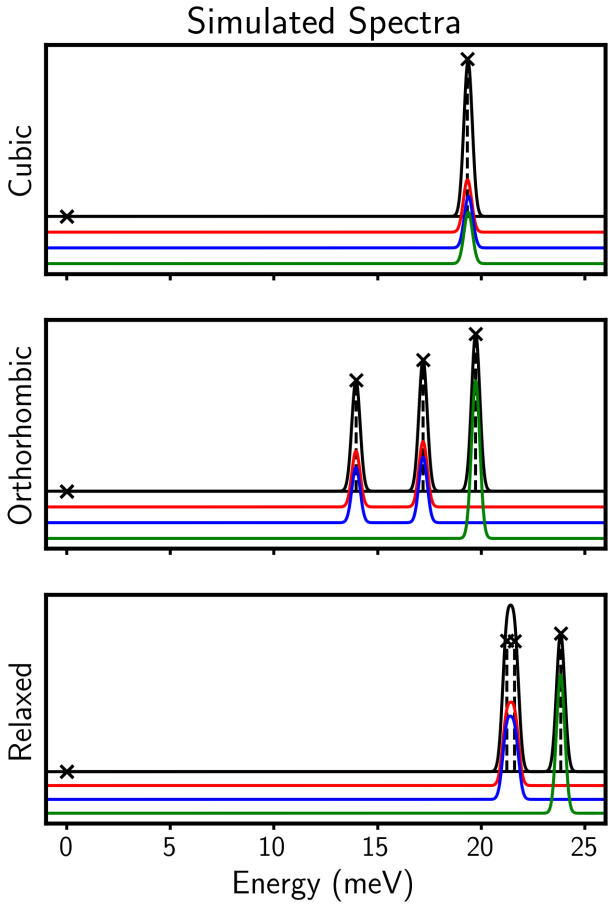

Figure 4.10: Simulated absorption spectrum for a 3.8 nm NC with various crystal structures with the lowest excitonic state set to the energy zero. The polarized spectra along the z (green), y (blue) and x (red) are also shown with an offset for clarity.

with the effective mass models [124]. The spectra for the relaxed structures show similarities to the orthorhombic structure, but the lower two excitonic states are close enough in energy that they may not be resolvable into separate peaks. The results for the relaxed structures add the additional structural complexity not considered in an effective mass model. Taken as a whole, the results of our model conclusively show that the inversion symmetry breaking in perovskite NCs is not sufficient to produce a bright ground state.

While it is easy to simulate a perfectly cubic NC, experiments tend to produce a distribution of NCs that differ from the perfect cubic geometry. This NC shape anisotropy is also known to impact the excitonic fine structure and may be implicated in the diversity of fine structure splittings observed experimentally [125]. In Figure 4.11 we consider the effect of shape anisotropy on NCs of cubic, orthorhombic and relaxed crystal structures. We

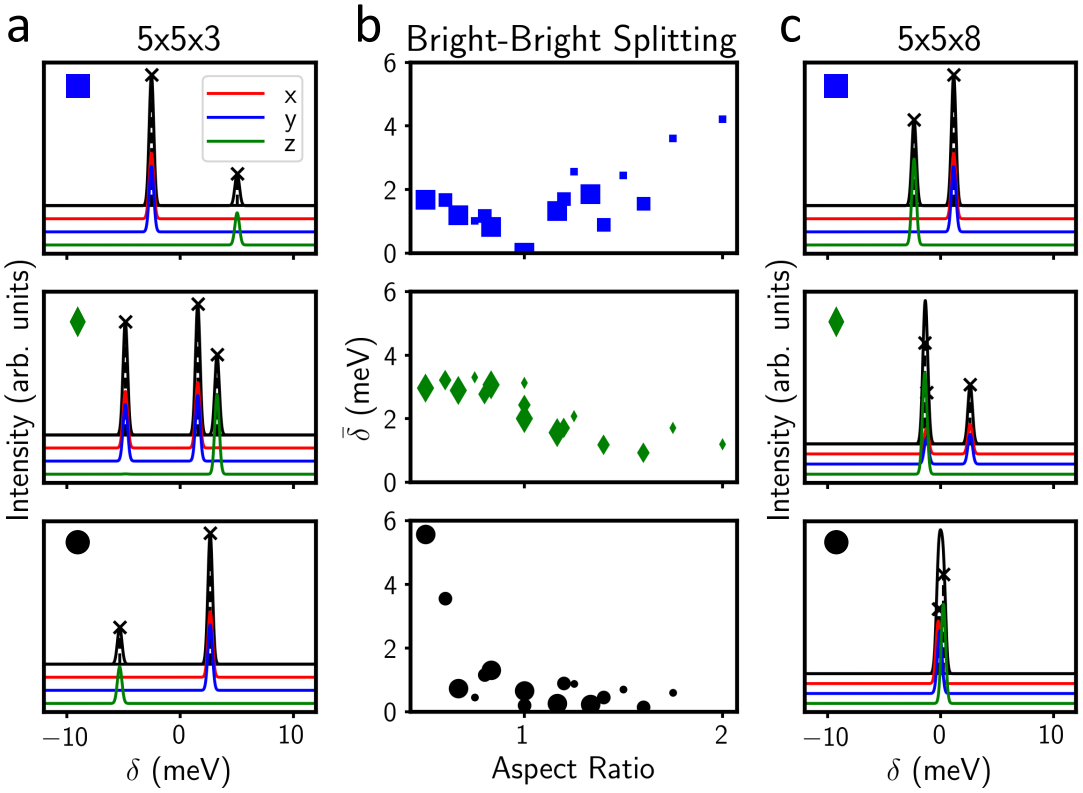

Figure 4.11: (b) The standard deviation of the bright excitonic states for the cubic (top), orthorhombic (middle) and relaxed (bottom) crystal structures. The sizes of the symbols represent the sizes of the NCs along the x and y directions. The largest symbols correspond to $N = 6$ and the smallest to $N = 4$. (a) The polarization-dependent spectra for NCs consisting $5 \times 5 \times 3$ lead-halide octahedra (aspect ratio of 0.6) and (c) $5 \times 5 \times 8$ octahedra (aspect ratio of 1.6) similarly arranged by crystal structure.

generated a series of NCs consisting of $N \times N \times Z$ lead-halide octahedra where $N = 4, 5, 6$ and $Z = 3, \ldots, 8$. We define the aspect ratio as Z/N and in Figure 4.11(b) we plot the standard deviation of the bright states for each of these NCs. In Figure 4.11(a) and (c) we show the polarization dependent spectra of the bright states for an aspect ratio less than 1 and greater than 1 respectively. For the NCs with cubic crystal structures the bright-bright splitting is zero for cube-shaped crystals, and either adding or removing layers from such a NCs causes a finite splitting. As the axis of shape anisotropy was chosen as the z-axis, the x- and y-polarized excitons remain degenerate, as seen in the plotted spectra. For an aspect ratio less than 1 the z-polarized exciton is split higher in energy. For an aspect ratio greater than 1 the z-polarized exciton is lower in energy than the x- or y-polarized ones. This behavior agrees well with what has been derived from various effective mass models [114, 124, 125].

The NCs with an orthorhombic crystal structure show a significant degree of bright-bright splitting at all aspect ratios, consistent with effective mass theories [114, 124, 125]. Additionally, the extent to which the z-polarized exciton is split lower at large aspect ratio appears suppressed, as it can be seen to be essentially degenerate with the lower x/y-polarized exciton in the middle panel of Figure 4.11(c). The relaxed structures show a unique behavior with significant bright-bright splittings at aspect ratios less than 1, which are due almost entirely to the z-polarized exciton splitting to lower energy. This behavior is the opposite of that observed in the orthorhombic and cubic phases, and may result from surface relaxation effects that become more dominant for plate-like geometries. At larger aspect ratios, the relaxed structures show small splitting that depends only weakly on aspect ratio. This may be due to the size-dependent effects discussed above. As single NC measurements remain extremely challenging, especially those correlated to NC shape data, understanding the exact impacts of NC shape anisotropy is still an experimental challenge.

In conclusion, we calculate the exciton FS for lead-halide perovskite NCs using a fully atomistic theory to obtain relaxed NC crystal structures and the electronic states of these relaxed NCs. The structural relaxation reveals in atomistic detail previously predicted structural transitions, and the electronic theory reproduces experimental optical gaps with excellent agreement. This atomistic theory would be able to discern the causes and nature of a Rashba effect caused by collective inversion symmetry breaking if it was present in these systems. None of the signatures of a significant Rashba effect are found in this study. For all NCs studied the excitonic ground state is optically dark, and we conclude that it should remain so for all NC sizes. The explanation of the anomalous temperature dependence of radiative lifetimes in perovskite NCs must lie elsewhere and will be a subject of future investigation.

Chapter 5

Kinetics of Hole Transfer from Multiexcitonic Quantum Dots

The pseudopotential methods discussed in Chapter 2 can provide utility beyond simply examining the optical signatures of nanomaterials, such as in Chapter 4. These methods can also give access to the rates of dynamic excited state processes in these nanomaterials. In this chapter we utilize this insight into these dynamics to inform a kinetic master equation describing the transfer of holes from multiply excited quantum dots to molecular acceptors attached at the surface. The content in this chapter is adapted with permission from Yan C.; Weinberg, D.; Jasrasaria, D. *et al.* Uncovering the Role of Hole Traps in Promoting Hole Transfer from Multiexcitonic Quantum Dots to Molecular Acceptors. *ACS Nano* **2021** *15*(2), 2281-2291.

5.1 Introduction

As compared to molecular light absorbers, QDs have the capacity to concentrate many excited charge carriers within a small volume following multiple photon absorption or charge multiplication processes, due to their large absorptivity and high density of available electronic states [157, 158]. The multiexcitonic state of a QD can enable photophysical processes that are inaccessible by single-excitonic states, such as the transfer of multiple charges on ultrafast time scales [159, 160] and the tunneling transport of electrons across high energy barriers [161]. The efficient extraction of charge carriers from multiexcitonic QDs would also be particularly useful for reactions related to photocatalytic solar fuel generation, as these chemical transformations universally involve multielectron catalysis.

As depicted in Figure 5.1A, the multiexcitonic state of a QD can undergo multiexcitonic dissociation (MED) to transfer charges to acceptors, thereby creating a charge-separated state, which generally has a long lifetime. However, as the excitons are confined in the small volume of a nanocrystal, the Coulomb interaction between multiple excitons unavoidably leads to Auger recombination (AR), which nonradiatively annihilates an exciton and creates

a hot electron–hole pair. The AR rate increases nonlinearly with the number of excitons in a QD [158]. On fast time scales from several to hundreds of picoseconds, AR can swiftly annihilate charge carriers until the QD is brought to the single-excitonic state [158]. Hole transfer rates are typically much slower, and yet ideally QDs could be designed such that, when multiply excited, hole transfer could still compete efficiently against AR.

Ultrafast multiple electron transfer occurring within a few picoseconds has been observed to compete effectively against AR events in a number of systems, including CdS QDs [162], CdSe QDs [163], CdSe/CdS core/shell QDs [159], and PbS QDs [164]. In contrast, the transfer of multiple holes from a QD to acceptors is typically much more challenging and had not been observed until a recently reported case, where up to 5.6 holes were extracted from a $CsPbCl_xBr_{3-x}$ QD to tetracene acceptors [165]. As the inefficient part of the redox cycle, hole transfer processes often form the bottleneck for improving the overall performance of photocatalysts and photovoltaic devices [166]. Furthermore, the accumulation of holes on the widely studied metal chalcogenide QDs leads to their eventual photodegradation [167]. Therefore, it is very desirable to provide mechanistic insights for devising pathways that could efficiently extract multiple holes from a QD.

For metal chalcogenide QDs, hole trap states are prevalent on the surface due to underpassivated chalcogenide atoms [33, 168]. The multitude of these relatively localized hole traps play an important role in mediating hole transfer from delocalized valence band (VB) states to surface bound acceptors [169–171]. Hole-trapping states also affect the AR lifetimes by altering the electron–hole interactions and, therefore, significantly impacting the kinetic competition between hole transfer and AR dynamics [172–174]. Ultrafast transient absorption (TA) spectroscopy provides the time resolution required to directly track the population of holes in different states as they migrate from QDs to acceptors. Previous works with TA methods by Lian *et al.* and Weiss *et al.* have established that phenothiazine derivatives can serve as a class of hole acceptors for CdS QDs or nanorods with both the high driving force and the necessary optical signature in TA to track hole transfer [169, 175, 176]. In these model systems, ultrafast hole trapping was observed within ∼1 ps following photoexcitation, and trap-mediated hole-transfer dynamics were investigated under single-excitonic or biexcitonic conditions.

Herein, we utilized TA spectroscopy to investigate the hole-transfer dynamics from three different cadmium chalcogenide QDs to a synthesized phenothiazine derivative, which binds to the QD surface via a carboxylate group (Figure 5.1B). The QDs were excited by a pump pulse of 415 nm wavelength and the average initial number of excitons per QD, $\langle N0 \rangle$, was experimentally calibrated to range from ∼1 to 19. The hole acceptor, 4-(3-bromo-7-(dihexylamino)-10H-phenothiazin-10-yl)benzoic acid (NPTZ), is designed to carry functional groups on the phenothiazine ring to shift the photoinduced absorption (PA) signal of its oxidized form to the longer wavelength region >600 nm. The shifted PA feature enables us to track the hole transfer in CdSe and CdSe/CdS QDs by avoiding interference with exciton bleaching (XB) signal.

In the QD-NPTZ systems, the time-dependent populations of the trapped holes and the oxidized ligands were separately tracked and analyzed so that we could systematically

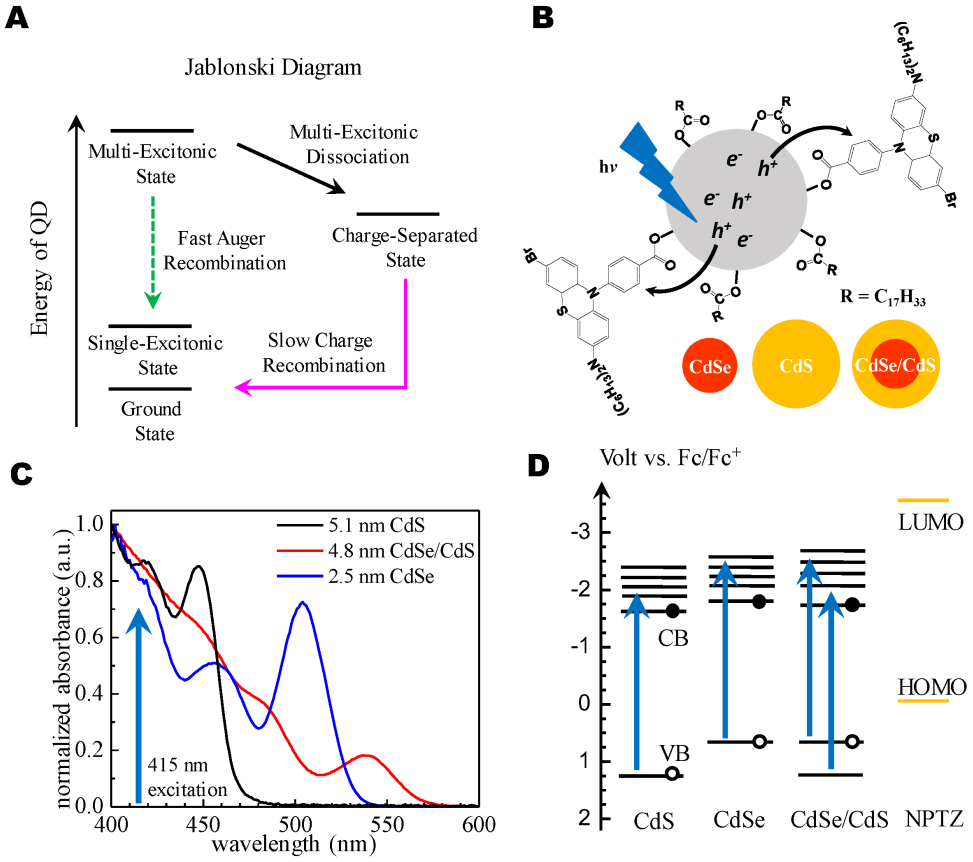

Figure 5.1: A) The Jablonski diagram of the QD-NPTZ system used to study multi-excitonic hole transfer dynamics. The fast Auger recombination dynamics (green dashed arrow) competes with multi-excitonic dissociation dynamics (black arrow). B) Schematic illustration of multi-excitonic hole transfer from QDs to NPTZ ligands. C) Normalized absorption spectra of the investigated QDs dissolved in toluene. The excitation wavelength used in TA experiments was 415 nm (∼3.0 eV). D) The diagram shows the energy levels of QDs and NPTZ ligand relative to the ferrocene/ferrocenium redox couple in acetonitrile. Trapping states are omitted from the display. The scaled length of the blue arrows is 3.0 eV. For the core/shell system, both CdSe core and CdS shell contribute to photo-absorption.

investigate the interplay between charge trapping, hole transfer, and Auger recombination dynamics. To describe the observed kinetics, we test two types of kinetic models where the hole-trapping states are kinetically coupled to or decoupled from the VB populations. For QDs passivated with oleate ligands (referred to as native QDs), our results indicate that the hole-trapping states exist in a fast trapping/detrapping equilibrium with the VB, and the trapped holes can be rapidly consumed by AR events. In contrast, the hole-trapping states in QDs capped with NPTZ ligands are kinetically decoupled from VB states and have prolonged lifetimes. Fluence dependent hole transfer kinetics were observed at intermediate times of 10s to 100s of ps, after AR would be expected to relax the QDs to single-excitonic states. These decoupled trapping states resemble the long-lived charge-separated states proposed to account for the "dark states" in QD single particle blinking experiments [177, 178]. The long-lived, trapped holes can serve as a reservoir to temporarily store charges and then slowly transfer to NPTZ over the course of 10s to 100s of ps. In the most efficient system, up to three holes were transferred to NPTZ per CdS QD.

5.2 Transient Absorption Spectroscopy of QDs

To investigate the competition between hole transfer and AR kinetics, we examined a series of QDs of different sizes and compositions. As the AR lifetime of a QD generally increases with the volume of a QD [77, 158], we present the results obtained from the following systems: a small CdSe QD ($d = 2.5$ nm); a large CdS QD ($d = 5.1$ nm); and a core/shell CdSe/CdS QD ($d_{\text{total}} = 4.8$ nm, $d_{\text{core}} = 2.3$ nm) with a quasi-type II band structure.

To promote the transfer of multiple holes, the QDs were functionalized with the highest possible surface coverage of the NPTZ ligands. The NPTZ ligands replace the native oleate ligands in a 1-to-1 stoichiometry and bind to cadmium ions on the QD surface via their carboxylate group. The 1-to-1 stoichiometry and surface coverage of the NPTZ ligand can be determined by the 1H nuclear magnetic resonance technique (Table S1). Because the NPTZ ligands are significantly larger molecules than the oleate ligands, the surface coverages of NPTZ ligands saturates at around 20% for all the QDs. For the 2.5 nm CdSe, we calculated that there are ∼25 NPTZ ligands bound per QD. For the 5.1 nm CdS and 4.8 nm core/shell QD, there are ∼75 NPTZ ligands bound per QD.

The UV–vis absorption spectra of the three types of QDs are shown in Figure 5.1C. In the TA experiments, the pump wavelength was set above the band edge energy of the QDs at 415 nm (∼3 eV) to access levels deep in the energy bands and create a large number of excitons. The energy diagrams of the QDs and NPTZ are shown in Figure 5.1D. The absorption feature of the phenothiazine ring located in the UV region (>3 eV) will not be excited [169, 176]. The driving force of hole transfer from all three types of QDs to the NPTZ molecule is sufficiently high [166], as the highest occupied molecular orbital (HOMO) of NPTZ is located 0.7 and 1.2 eV above the VB band edges of CdSe and CdS, respectively [166]. Photoinduced charge transfer from the QDs to NPTZ is energetically prohibited. The blue arrows in Figure 5.1D point to the highest possible conduction band (CB) levels to which the electrons can

be promoted by the 415 nm excitation. These levels are significantly lower than the lowest unoccupied molecular orbital (LUMO) of NPTZ. The HOMO and LUMO positions of NPTZ were determined from cyclic voltammetry and UV–visible absorption spectroscopy.

Photoexcited hot electrons and holes rapidly cool on a subpicosecond time scale to energy levels near the band edges, as shown by the solid and empty circles, respectively, in Figure 5.1D. The strongly quantum confined 2.5 nm CdSe QD and the weakly quantum confined 5.1 nm CdS QD differ significantly in the VB edge energies but have similar CB edge energies. For the 4.8 nm CdSe/CdS QD containing a 2.3 nm CdSe core, the 415 nm pump pulse excites both the CdSe core and the CdS shell. Due to the small size of the core, the energy levels of CdSe and CdS form a quasi-type II alignment causing the electron wave function to distribute throughout both the core and the shell while the hole wave function localizes mostly to the core after cooling [94, 159, 179]. In the core/shell system, the driving force for hole transfer is determined by the CdSe core, and the transfer to surface ligands needs to overcome the energy barrier of the CdS shell [166, 170].

We measured the TA spectra for a series of excitation fluences for both of the native QDs capped with oleate ligands and the QDs with surface-bound NPTZ ligands. For each TA measurement, the initial average number of excitons per QD, $\langle N_0 \rangle$, was experimentally determined from the calibrated energy per pump pulse, the effective absorbance at 415 nm for each pump pulse energy, the excited sample volume, and the concentration of QD in solution. To reduce the spread of $\langle N_0 \rangle$ caused by the attenuation of the pump pulse through the sample while maintaining a reasonable signal level for TA experiments, the optical densities at 415 nm for all the samples were kept around 0.2. The relative standard deviation of the calculated $\langle N_0 \rangle$ is $\sim$15% for all of the samples.

In Figure 5.2, the TA spectra of CdS QDs with native oleate ligands and NPTZ ligands are displayed as examples to illustrate the major TA features used for kinetic analysis. The major negative XB feature around 450 nm shown in Figure 5.2A is associated with the bleaching of the first excitonic transition from $1S_h$ to $1S_e$ of the QD. The change of absorbance induced by the pump pulse, ΔA, was divided by the steady-state linear absorbance at the first excitonic absorption peak, A_0. The lowest CB level ($1S_e$ state) can accommodate at most two electrons, and therefore, the XB signal at the band edge will be close to the saturation level of $\frac{\Delta A}{A_0} \sim 1$ when the CB is populated by two or more electrons [159, 175]. At the early time $t = 10$ps, both the QDs with and without NPTZ ligands showed nearly full saturation of the band edge XB signal as seen by the black lines in Figure 5.2A. For QDs without NPTZ added (top panel), the XB signal decayed to $\frac{\Delta A}{A_0} \sim 0.5$ at longer delay times $t > 100$ps, indicating that fast AR processes have brought the system from a multiexcitonic state to a single-excitonic state. For CdS QDs bound with NPTZ ligands (bottom panel), the full saturation level lasts for several nanoseconds (ns), indicating that >1 electron remains on the CB. For systems where less than 2 holes were transferred, we did not observe the lasting saturation of the band edge XB signals on ns time scales (Figures 5.3 and 5.4). This XB signal cannot, however, be used to determine the dynamic behavior of the holes associated with these electrons. Tracking the hole population requires detailed analysis of other spectroscopic data discussed below.

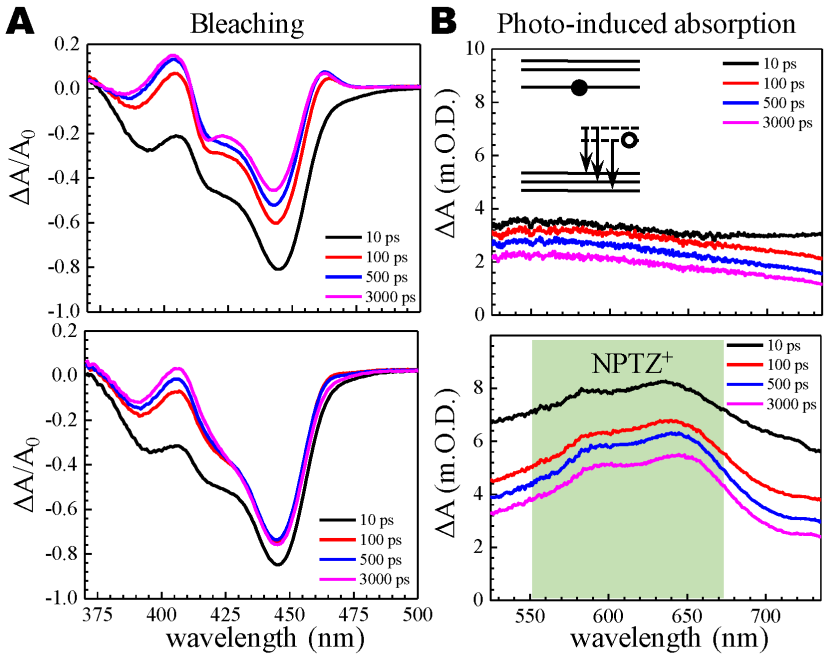

Figure 5.2: Examples of TA spectra at various delay times showing the exciton bleaching (A) and photo-induced absorption (B) features of CdS QDs without NPTZ (top panels) and with NPTZ (bottom panels) added. The excitation power is 1.25 μJ per pulse and $\langle N_0 \rangle \approx 19$. The inset in the upper panel of (B) indicates that the broad offset-like PA feature originates from the absorptions promoting the trapped holes into densely spaced levels deep in the VB. The green shaded area in the bottom panel of (B) highlights the PA peaks of $NPTZ^{+\bullet}$ radical on top of the PA feature of trapped holes.

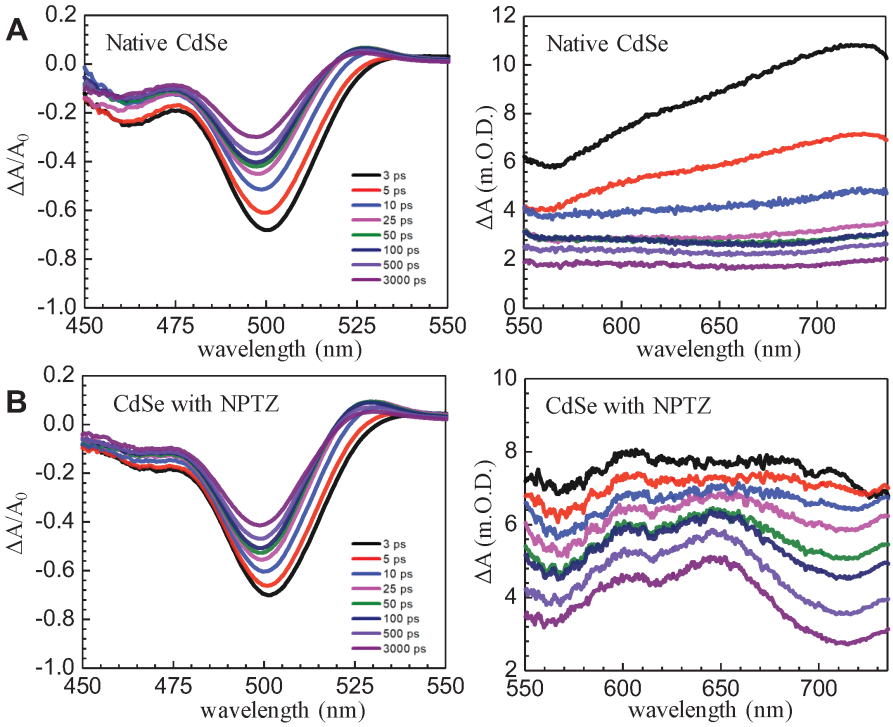

Figure 5.3: Examples of TA spectra of the native CdSe QDs (A) and CdSe QDs with NPTZ (B). Left panels display XB signals and right panels display PA signals. The data shown here were measured at $\langle N_0 \rangle \sim 4$ with a pump pulse energy of 1.25 μJ. A_0 is the linear absorbance measured by UV-Vis at the first excitonic absorption center.

In Figure 5.2B, the positive PA features of CdS are shown in the range of 535-735 nm. Based on theoretical [34] and experimental evidence [159, 180] this broad but weak PA signal is assigned to the transitions promoting trapped holes into deeper levels of the VB (inset in the upper panel of Figure 5.2B). The high density of states in the VB causes the broad feature of the PA signal. The hole trapping states in native QDs dispersed in colloidal solutions are typically attributed to under-passivated surface chalcogenide atoms. The PA signal of trapped holes shares the same broad, offset-like feature for all the three types of QDs measured here. The transient kinetics of the trapped hole population are largely independent of the wavelength chosen for analyzing the PA signal. To avoid overlapping with the PA signal of oxidized NPTZ ligands, we chose to use 710 nm as the wavelength for tracking the population of trapped holes because the signal amplitude at 710 nm was unaffected by the deconvolution of the contribution from the molecular acceptors. Hole transfer and AR of multi-excitonic states can be inferred from the decay kinetics of the broad PA feature. As discussed later, the decay kinetics of the population of trapped holes represented at 710 nm

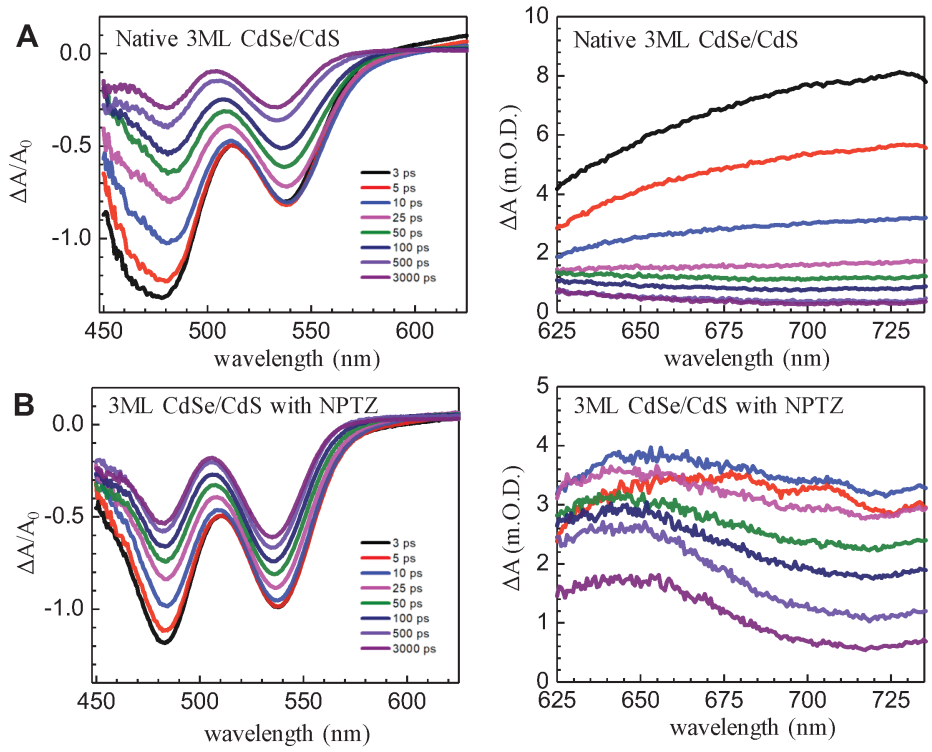

Figure 5.4: Examples of TA spectra of the native 3ML CdSe/CdS QDs (A) and native 3ML CdSe/CdS QDs with NPTZ (B). Left panels display XB signals and right panels display PA signals. Due to the redshifted tail of XB features as compared to other QDs studied here, part of the $NPTZ^{+\bullet}$ PA band is convoluted with the XB tail. Data deconvolution was performed in the wavelength region of 625-735 nm. The data shown here were measured at $\langle N_0 \rangle \sim 19$ with a pump pulse energy of 1.27 μJ. A_0 is the linear absorbance measured by UV-Vis at the first excitonic absorption center.

were qualitatively different for QDs with or without NPTZ ligands due to the altered nature of hole trapping states.

For NPTZ-capped QDs, the oxidation of NPTZ ligands by hole transfer gives rise to the new absorption band in the region from 550-670 nm (green shaded area in Figure 5.2B). This PA band is assigned to the transiently generated $NPTZ^{+\bullet}$ radical, and the extinction coefficient of the PA peak at 650 nm was estimated from steady-state oxidation titrations. Compared to the phenothiazine molecule, the amine group and the bromine atom on the aromatic ring of NPTZ shifted the radical absorption peak from 520 nm to 650 nm. For the CdSe and the core/shell QDs studied here, the shifted peak allows the radical PA signal to be resolved from the tails of the XB signal, which is larger in amplitude by orders of magnitude. For CdSe QDs larger than $d = 3.5$ nm or CdSe/CdS QDs larger than the one studied here, the XB signal would redshift enough to severely interfere with the $NPTZ^{+\bullet}$ radical signal. The signal of the $NPTZ^{+\bullet}$ radical and the broad signal of trapped holes can be de-convoluted from each other by a fitting protocol [169, 176]. The de-convoluted PA amplitude of $NPTZ^{+\bullet}$ at 650 nm directly tracks the average number of holes transferred per QD, $\langle N_{\mathrm{HT}} \rangle$, which was calculated by the ratio of the concentration of the $NPTZ^{+\bullet}$ radical to the concentration of QDs.

To deepen our mechanistic understanding of the hole transfer process, we developed a kinetic model of the dynamics of the hole populations on both the native QDs and QDs with NPTZ hole acceptors. As discussed below for Figure 5.9, the kinetic model incorporates three hole populations: valence band holes, trapped holes, and holes transferred to NPTZ ligands. The population of trapped holes can be tracked with the broad PA signal at 710 nm, and the population of holes transferred to NPTZ ligands can be monitored by the 650 nm $NPTZ^{+\bullet}$ absorption band. While the population of valence band holes cannot be measured directly in the optical range of our experiments, it can be inferred from the initial excitation conditions. The processes of trapping, de-trapping, AR, and hole transfer connect these hole states and give rise to the complex dynamic behaviors we observe and simulate within our kinetic model.

5.3 Determination of Auger Recombination Channels and Rates

5.3.1 Theoretical Modeling of AR Channels

To identify AR channels in the presence of hole trapping states, AR lifetimes were computed and compared for two types of initial biexcitonic states: i) two electrons in the CB and two holes in the VB; ii) two electrons in the CB, one hole in the VB, and one hole in a surface trapping state. CdSe QDs are chosen as a model system, and calculations were performed on CdSe QDs of different sizes. First, nanostructure configurations for CdSe QDs were obtained by cleaving a sufficiently large wurtzite crystal with a lattice constant

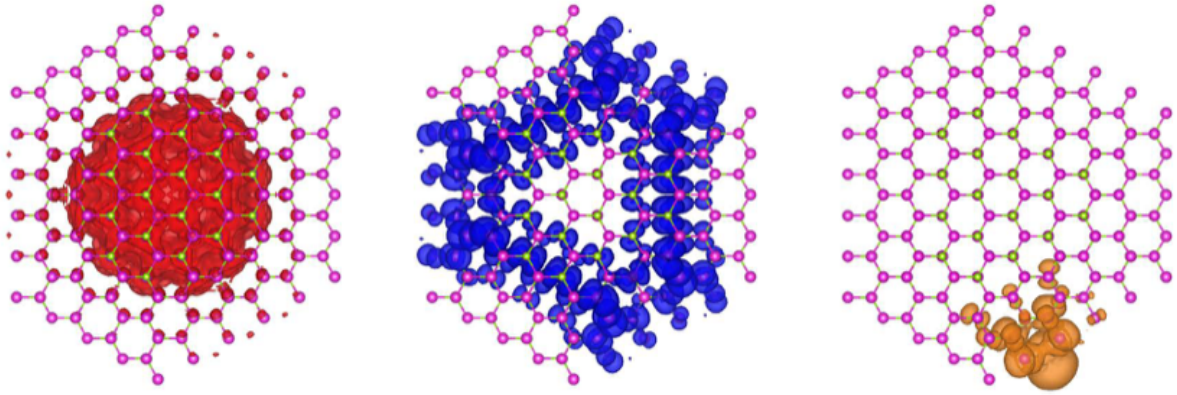

Figure 5.5: Single-particle charge carrier densities for the conduction band edge (red), valence band edge (blue), and hole trap (orange) states of the 3.86 nm CdSe QD.

of bulk wurtzite CdSe ($a = 4.30$Å$, c = a\sqrt{\frac{8}{3}}$) such that all atoms are bonded to at least two other atoms. This structure was then optimized via the conjugate gradient minimization algorithm implemented in LAMMPS [181] using Stillinger-Weber interatomic potentials [83]. The outermost layer of atoms was removed and then the subsequent monolayer was replaced with ligand potentials, representing the passivation layer, where each Cd (Se) atom was replaced by a ligand potential for Se (Cd). Surface hole traps were modeled by the removal of a passivation ligand from a Se atom on the surface, which creates a localized trap state about 500-750 meV above the VB maximum. Four structures were modeled and studied here: $Cd_{93}Se_{93}$ ($d = 2.15$ nm); $Cd_{222}Se_{222}$ ($d = 3.00$ nm); $Cd_{435}Se_{435}$ ($d = 3.86$ nm); $Cd_{753}Se_{753}$ ($d = 4.71$ nm).

All calculations were performed within the semi-empirical pseudopotential method for CdSe structures [31] implemented on real-space grids with spacing less than 0.8 a.u., which is sufficient to converge results. The filter-diagonalization technique was applied to obtain quasiparticle states $\phi(r_e)$ and $\phi(r_h)$ at the valence and conduction band edges, respectively. This process involves filtering states at target energies near the LUMO and HOMO energies using an interpolation polynomial of length $N_c \approx 2048$. The states obtained from filter-diagonalization are eigenstates of the single-particle Hamiltonian. The charge carrier densities for the conduction band edge (red), valence band edge (blue), and a hole trap (orange) states of the 3.86 nm CdSe QD obtained from filter diagonalization are illustrated below in Figure 5.5.

These single-particle states were used as input to the Bethe-Salpeter equation (BSE), which solves for the coefficients ($c_{a,i}$) used to describe correlated electron-hole pair (i.e. excitonic) states as a linear combination of non-interacting electron-hole pairs:

$$\psi(\boldsymbol{r}_e, \boldsymbol{r}_h) = \sum_{a,i} c_{a,i} \phi_a(\boldsymbol{r}_e) \phi_i(\boldsymbol{r}_h) \tag{5.1}$$

where a refers to electron states and i refers to hole states. The number of single-particle states used in the BSE was 120-200, with larger numbers of single-particle states needed for larger systems. The exciton energies and AR lifetimes are converged with the number of single-particle states used. The electron-hole kernel in the Bethe-Salpeter equation includes both the screened direct Coulomb attraction and exchange-like repulsive term. This is discussed in detail in Chapters 2 and 4.

The biexcitonic AR lifetime ($\tau_{\mathrm{AR},2}$) was computed using Fermi's golden rule, where we average over thermally distributed initial biexcitonic states ($|\mathrm{B}\rangle$) and sum over all final decay channels into single excitonic states ($|\mathrm{S}\rangle$), which are coupled by the Coulomb scattering ($\hat{V}$):

$$\tau_{\mathrm{AR},2}^{-1} = \sum_{\mathrm{B}} \frac{e^{-\beta E_{\mathrm{B}}}}{Z_{\mathrm{B}}} \left[\frac{2\pi}{\hbar} \sum_{\mathrm{S}} \left| \langle \mathrm{B} | \, \hat{V} \, | \mathrm{S} \rangle \right|^2 \delta(E_{\mathrm{B}} - E_{\mathrm{S}}) \right] \tag{5.2}$$

where $Z_{\mathrm{B}} = \sum_{\mathrm{B}} e^{-\beta E_{\mathrm{B}}}$ is the partition function for the biexcitonic states and $\beta = \frac{1}{k_B T}$ at $T = 298\mathrm{K}$.

The initial biexcitonic state and final single excitonic states are given, respectively, by:

$$|\mathrm{B}\rangle = \sum_{b,j} \sum_{c,k} c_{b,j}^{\mathrm{B}} c_{c,k}^{\mathrm{B}} \phi_b(\boldsymbol{r}_e) \phi_c(\boldsymbol{r}'_e) \phi_j(\boldsymbol{r}_h) \phi_k(\boldsymbol{r}'_h) \tag{5.3}$$

$$|\mathrm{S}\rangle = \phi_a(\boldsymbol{r}_e) \phi_i(\boldsymbol{r}_h) \tag{5.4}$$

The indices $a, b, c, \ldots$ refer to electron (unoccupied) states and the indices $i, j, k, \ldots$ refer to hole (occupied) states with corresponding energies ϵ_a and ϵ_i. The interacting electron-hole pair (excitonic) states obtained from BSE were used in the initial biexcitonic states, while the final excitonic states were obtained using filter-diagonalization calculations with target energies resonant with the initial biexcitonic state. A longer interpolation polynomial length of $N_c \approx 8192$ was used for those filter calculation, reflecting the greater density of single-particle states at energies high above the band edge. The initial biexcitonic state includes correlations within electron-hole pairs but ignores them between the two excitons [64]. The correlations in the final electron-hole pair are also ignored.

Therefore, the AR lifetime was computed as

$$\tau_{\mathrm{AR},2}^{-1} = \sum_{\mathrm{B}} \frac{2\pi e^{-\beta E_{\mathrm{B}}}}{\hbar Z_{\mathrm{B}}} \sum_{a,i} \left| \sum_{b,c,k} c_{b,i}^{\mathrm{B}} c_{c,k}^{\mathrm{B}} V_{abck} \right|^2 \delta(E_{\mathrm{B}} - \epsilon_a + \epsilon_i) \tag{5.5}$$

$$+ \sum_{\mathrm{B}} \frac{2\pi e^{-\beta E_{\mathrm{B}}}}{\hbar Z_{\mathrm{B}}} \sum_{a,i} \left| \sum_{j,c,k} c_{a,j}^{\mathrm{B}} c_{c,k}^{\mathrm{B}} V_{ijck} \right|^2 \delta(E_{\mathrm{B}} - \epsilon_a + \epsilon_i) \tag{5.6}$$

where the first term represents the electron channel (final electron-hole pair involves a hot electron) and the second term represents the hole channel (final electron-hole pair involves a hot hole). The Coulomb coupling V_{rsut} is given by

$$V_{rsut} = \iint \frac{\phi_r^*(\boldsymbol{r}) \phi_s(\boldsymbol{r}) \phi_u(\boldsymbol{r}') \phi_t^*(\boldsymbol{r}')}{|\boldsymbol{r} - \boldsymbol{r}'|} d^3\boldsymbol{r} d^3\boldsymbol{r}' \tag{5.7}$$

The initial biexcitonic states including a trapped hole are composed of one exciton with a trap coefficient (c_{tr}) of approximately 1 ($c_{\mathrm{tr}} = \sum_a |c_{a,\mathrm{tr}}|^2$) and another exciton with a trap coefficient of approximately 0, where $c_{a,\mathrm{tr}}$ refers to the coefficient of an noninteracting electron-hole pair with the hole in the single-particle trap state. The calculated AR rates were Boltzmann-averaged over five different trap locations that were evenly distributed across the surface of the nanostructure.

As discussed above and depicted in Figure 5.6 below, AR can occur through different negative trion pathways (electron channels) and positive trion pathways (hole channels), leading to different final single electron-hole pair configurations. Channels A and C are the VB AR pathway shown in Figure 5.9B, and channel B is the VB-trap AR pathway in Figure 5.9B. While Figure 5.6 shows trion decay channels, the calculation performed here use biexcitonic initial states, so the initial and final state configurations also include a spectator ion that does not participate in AR. For channel A and D, the final state is a hot electron and a spectator hole in VB or trap. For channels B and C, the final state is a hot hole and a spectator electron. The rate of each of these channels was determined by examining the partial sum over final states just corresponding to that channel. For example, the rate of channel A is given by the sum over final states that correspond to the configuration shown in Figure 5.6 (with the appropriate spectator ion):

$$\tau_{\mathrm{AR},2}^{-1} = \sum_{\mathrm{B}} \frac{e^{-\beta E_{\mathrm{B}}}}{Z_{\mathrm{B}}} \left[\frac{2\pi}{\hbar} \sum_{\mathrm{S}\in\mathrm{A}} \left| \langle \mathrm{B}| \hat{V} |\mathrm{S}\rangle \right|^2 \delta(E_{\mathrm{B}} - E_{\mathrm{S}}) \right] \tag{5.8}$$

The total rate for a given biexcitonic state is a sum of the rates of all the channels. For the biexcitonic state with two electrons in the CB and two holes in the VB, the channels only involve holes in the VB, and the summation is as follows:

$$\tau_{\mathrm{AR},2}^{-1} = \left(\tau_{\mathrm{AR},2}^{-1}\right)_{\mathrm{A}} + \left(\tau_{\mathrm{AR},2}^{-1}\right)_{\mathrm{C}} \tag{5.9}$$

While for the bi-excitonic state including a trapped hole (two electrons in the CB, one hole in the VB, and one hole in the trap), the channels involve both the VB hole and the trapped hole, and the summation is as follows:

$$\tau_{\mathrm{AR},2}^{-1} = \left(\tau_{\mathrm{AR},2}^{-1}\right)_{\mathrm{A}} + \left(\tau_{\mathrm{AR},2}^{-1}\right)_{\mathrm{B}} + \left(\tau_{\mathrm{AR},2}^{-1}\right)_{\mathrm{D}} \tag{5.10}$$

We found that the rates for channels A, B, and C are comparable, while the rate for channel D, however, is 3-4 orders of magnitude smaller than the others. Therefore, we conclude that recombination of an electron and trapped hole is slow, and AR through channel D (or AR of a biexciton with two trapped holes) is negligible. The summed biexcitonic AR lifetimes with or without the trapped hole are very similar, as collected in Table 5.1 below, illustrating that the surface-trapped holes do participate in AR on similar timescales as VB holes. For channel B, the Coulomb coupling that drives AR requires some overlap between the two holes in the initial biexciton, overlap between one hole and the conduction band-edge electron in the initial biexciton, and overlap between the other hole and the hot hole in

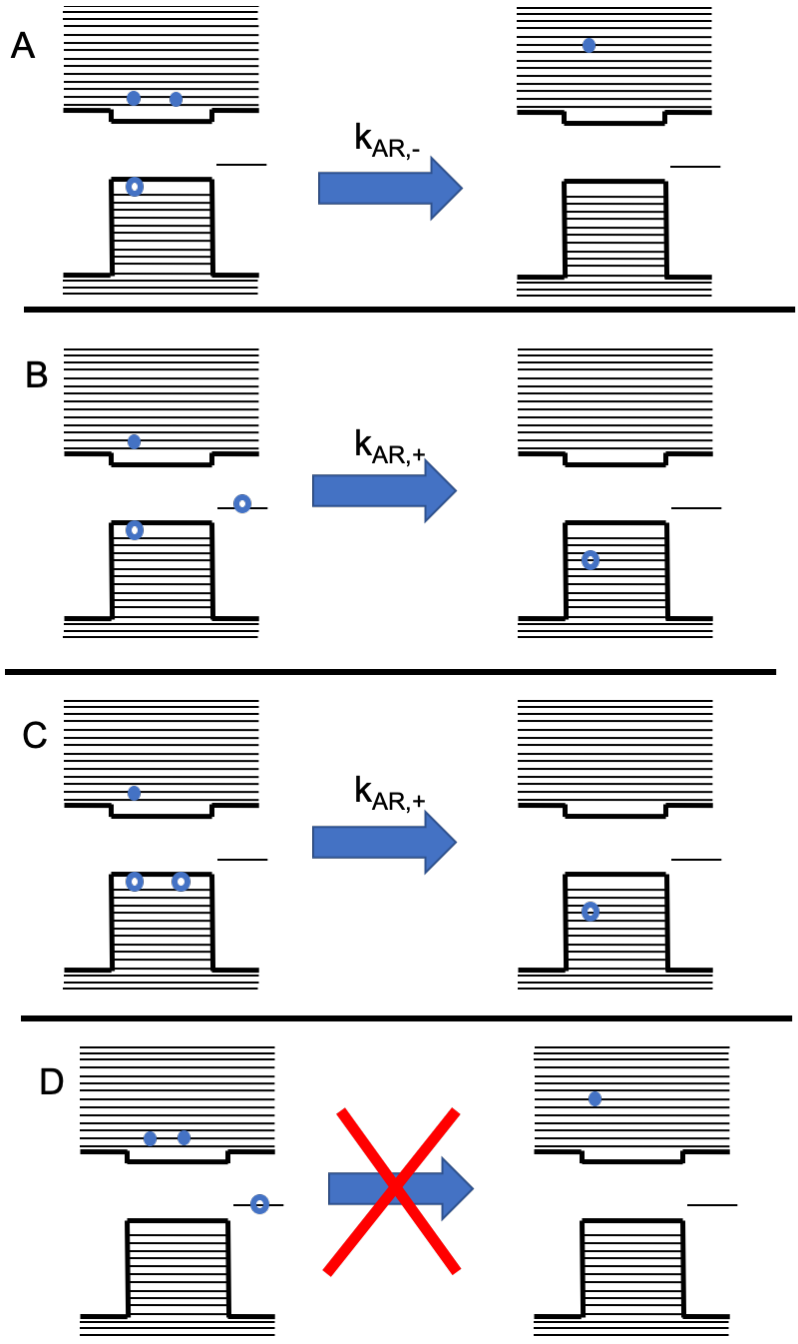

Figure 5.6: Different trion channels, identifiable by their initial and final states, for VB (A and C) and VB-trap (B) Auger recombination. The fourth "spectator ion" of the initial state is not illustrated, as its energy is unaffected by AR. Channels A-C have comparable rates, while the rate of channel D is $< (10\text{ ns})^{-1}$.

Table 5.1: Calculated AR lifetimes for an initial biexcitonic state with all carriers at the band-edge and for an initial biexcitonic state with three band-edge carriers and one hole localized at a surface trap state.

Diameter of CdSe NC (nm)	Band Edge $\tau_{AR,2}$ (ps)	Trap $\tau_{AR,2}$ (ps)
2.15	7.88	7.60
3.00	16.39	14.90
3.86	47.46	51.69
4.71	144.72	142.71

the final single exciton. Even though trapped holes are localized to the surface, there is still some wavefunction overlap with the holes at the VB edge, and there is favorable wavefunction overlap with hot hole states in the VB that have more oscillatory wavefunctions delocalized throughout the nanocrystal. Therefore, the rate of channel B can be comparable to that of A and C. The trion with two holes trapped at different sites, however, will not undergo AR as there is little to no overlap between those states. These findings are consistent with our previous calculations on the photoinduced transient absorption spectra of surface-trapped holes [34].

5.3.2 Fitting to Experimental Data

The experimental biexcitonic Auger recombination rates for the native CdS, CdSe, and CdSe/CdS core/shell QDs studied in this work were determined from the decay of the XB feature (Figure 5.7) measured using band edge excitation wavelength in TA experiments. The band edge excitation ensures that there are no more than two excitons per QD as there are only two optical excitons possible at that energy. For each QD sample, XB decays were measured at a high excitation fluence with $\langle N_0 \rangle \sim 2$, and a lower fluence with $\langle N_0 \rangle < 2$. The bi-excitonic AR rates can be extracted by simultaneously fitting the decay curves at the low and high fluences as described below. The native QD solutions contained in a 2 mm cuvette have an optical density of 0.8 at the first excitonic absorption peak center. The CdS QDs were excited at 450 nm with 350 nJ and 700 nJ per pulse; the CdSe QDs were excited at 510 nm with 600 nJ and 1250 nJ per pulse; and the CdSe/CdS were excited at 545 nm with 1000 nJ and 1800 nJ per pulse.

If absorption events are assumed to be statistically independent and equally probable with probability p, then the number of excitations per QD is binomially distributed. Therefore, immediately after photoexcitation, $\langle N_0 \rangle$ is $2p$. The initial peak value of the XB signal (ΔA_{max}) is proportional to $\langle N_0 \rangle$. At some intermediate time ($\sim$500 ps), when AR is assumed to be complete but radiative recombination is still not significant, all the particles that were initially doubly excited become only singly excited, so the average number of excitons per particle is $\langle N(t) \rangle = p^2 + 2p(1-p) = p(2-p)$. Taking the ratio of the optical signal at this intermediate time (ΔA_{int}) with the maximum bleach signal eliminates the constant of proportionality between the number of excitations and optical signal, and allows solving for

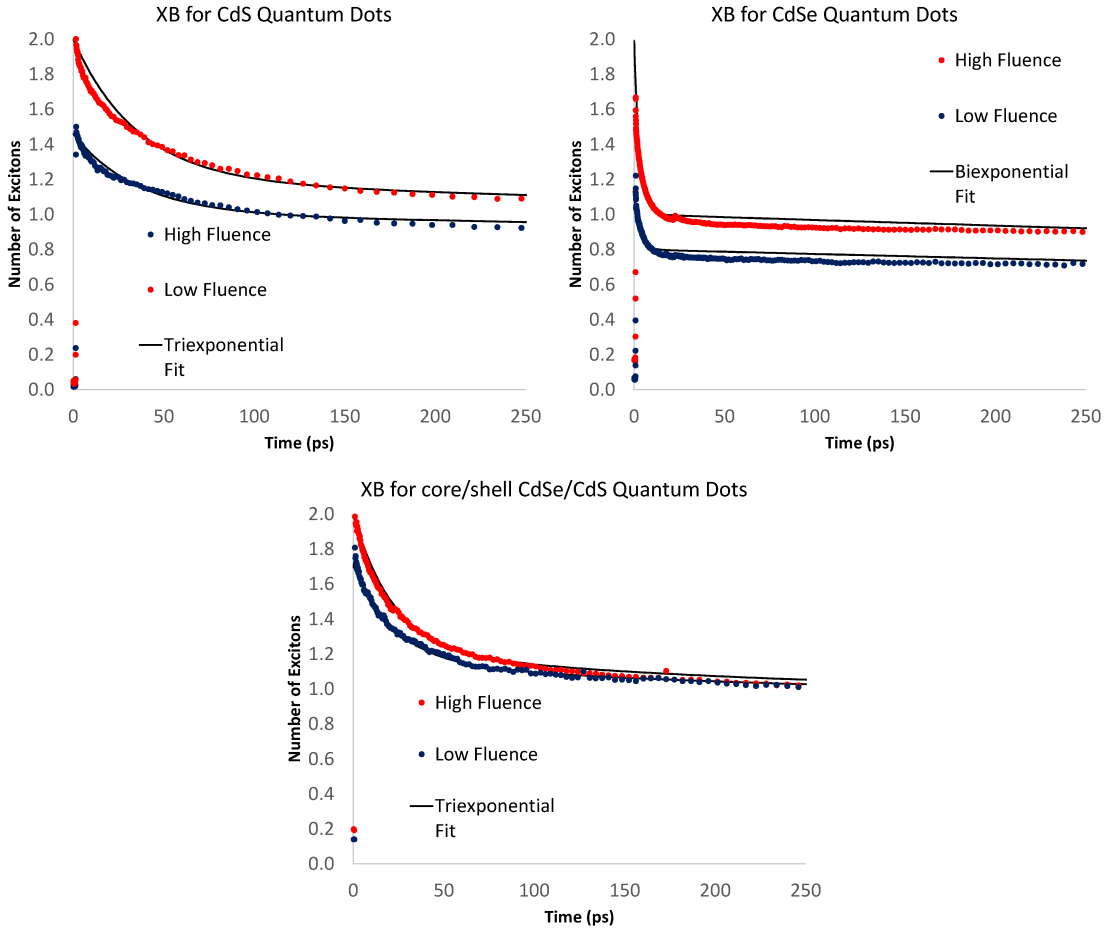

Figure 5.7: Fits of the experimental XB signals for CdS QDs (top), CdSe QDs (middle), and core/shell CdSe/CdS QDs (bottom).

the excitation probability $p = 2(1 - \frac{\Delta A_{\text{int}}}{\Delta A_{\text{max}}})$. From there, the constant of proportionality between the XB signal and $\langle N(t) \rangle$ can also be derived, allowing us to convert the measured kinetics to the decay of $\langle N(t) \rangle$ as a function of time in Figure 5.7.

For the systems studied here, all doubly excited particles rapidly (∼10-100 ps) undergo AR, resulting in an exponential recovery of the XB signal, until they are all singly excited. These singly excited states decay much more slowly (∼10 ns) via radiative recombination. The separation of timescales of AR and radiative recombination makes a bi-exponential model a good fit for these systems and excitation conditions. We took the average number of excitons per particle to be given by:

$$\langle N(t) \rangle = w_{\text{AR},2} e^{-t/\tau_{\text{AR},2}} + w_{\text{rad}} e^{-t/\tau_{\text{rad}}} \tag{5.11}$$

where $w_{\text{AR},2}$ and w_{rad} are the weights of the bi-excitonic Auger recombination and radiative

Table 5.2: Bi-excitonic decay parameters extracted from the exponential fits of the decay of the XB bleaching signal under band-edge excitation conditions.

System	$\tau_{AR,2}$ (ps)	τ_{resid} (ps)	τ_{rad} (ns)	High Fluence			Low Fluence		
				$w_{AR,2}$	w_{resid}	w_{rad}	$w_{AR,2}$	w_{resid}	w_{rad}
CdSe	3	-	~3	1	-	1	0.3	-	0.8
CdSe/CdS	22	200	~20	0.775	0.225	1	0.57	0.17	0.96
CdS	35	500	>20	0.800	0.200	1	0.45	0.11	0.9

recombination, respectively, and $\tau_{AR,2}$ and τ_{rad} are their respective lifetimes. The weights were determined by the initial conditions. The AR weight is the fraction of particles doubly excited $w_{AR,2} = p^2$, and the radiative weight is the number of particles that are at least singly excited $w_{rad} = p^2 + 2p(1-p)$. To fit the Auger and radiative recombination rates, the AR rate was estimated from those calculated within the semi-empirical pseudopotential method described above in Table 5.1 and the initial underestimate for radiative lifetime was taken to be 1 ns. The radiative lifetime was increased from there to give an approximate fit and then both rates were tuned until they simultaneously fit experimental data at low and high fluence conditions.

For core/shell CdSe/CdS and CdS QDs, a biexponential fit was unable to fully reproduce the experimental data, and a triexponential fit was used to include the weight and rate of a minor residual process:

$$N(t) = w_{AR,2}e^{-t/\tau_{AR,2}} + w_{rad}e^{-t/\tau_{rad}} + w_{resid}e^{-t/\tau_{resid}} \tag{5.12}$$

The sum of the Auger and residual weights is equal to the expected fraction of doubly excited particles. As the weight of this slower, residual process was relatively minor, the fastest timescale was taken as the AR lifetime. These AR rates are also consistent with the scaling laws of AR lifetimes [77]. The fitting parameters are listed in Table 5.2.

5.4 Understanding Hole Transfer through a Kinetic Model

5.4.1 Observation of Multi-Hole Transfer

In Figure 5.8A-C, the de-convoluted kinetics of $NPTZ^{+\bullet}$ at 650 nm are shown in the time range from 5 ps to 7 ns for the three QD systems studied here. For conditions with large $\langle N_0 \rangle$, the broad PA signal background from QDs measured prior to t = 5 ps has time-dependent slopes, which are difficult to analyze, so that data are not shown here. The pump pulse energies applied for each type of QD are in the interval between 0.07 μJ and 1.27 μJ per pulse. For CdS QDs and CdSe/CdS core/shell QDs, the excitation energies produce an $\langle N_0 \rangle$ ranging from ~2 to 19. Due to their smaller molar extinction coefficient at 415 nm, the $\langle N_0 \rangle$ for the CdSe QDs ranges from 0.5 to 4.4.

The kinetic plots in Figure 5.8A-C show that the photo-excited dynamics of a QD with NPTZ under multi-excitonic conditions take place on multiple timescales. In the first ∼10 ps, the CdS QDs (Figure 5.8A) display a very rapid initial increase in the $NPTZ^{+\bullet}$ signal, whereas the hole transfer signal of the other two QDs is insignificant in this time period. After ∼10 ps, all the QD systems exhibit an exponential increase in the $NPTZ^{+\bullet}$ signal over the next ∼100 ps. In the period from 1-7 ns, the hole transfer rate approaches zero for all QD systems. The population of transferred holes is generally stable with long charge-separation lifetimes. For the systems where multiple holes are transferred at high excitation fluences, the $NPTZ^{+\bullet}$ signals decay due to charge recombination between the radical and QDs on this long timescale, e.g., the pink trace of CdS in Figure 5.8A. For the CdS QDs, the transfer of multiple holes with $\langle N_{\mathrm{HT}} \rangle > 2$ was observed at the conditions of high $\langle N_0 \rangle$. For the CdSe and CdSe/CdS QDs, more holes were transferred as the excitation fluence was increased, but overall fewer than two holes were transferred from a QD to NPTZ molecules. The solid lines are modeling results, which will be discussed in the next section.

For efficient hole transfer to occur at short timescales and under multi-excitonic conditions, the hole transfer rate constant, k_{HT}, should be comparable to the AR rate constant, k_{AR} [158]. The bi-excitonic AR rates determined from native QDs are $(3.0\ \mathrm{ps})^{-1}$, $(22\ \mathrm{ps})^{-1}$, and $(35\ \mathrm{ps})^{-1}$ for the CdSe, CdSe/CdS, and CdS QDs, respectively (Table 5.2). Given the number of excitons per QD as N, k_{AR} scales as $N(N-1)$ for the larger CdSe/CdS and CdS QDs; k_{AR} scales as $N^2(N-1)$ for the strongly quantum confined 2.5 nm CdSe QDs [77, 158, 182]. Based on the scaling laws and biexciton AR rates, we can calculate that most of the charge carriers in multi-excitonic QDs will be consumed by AR mechanism within the first 10 ps the AR rate constants for just three excitons would be faster than $(10\ \mathrm{ps})^{-1}$ for all the QDs here.

We found here that only the CdS QDs have comparable rates of hole transfer and AR. In Figure 5.8A, for $\langle N_0 \rangle = 7$, 12, 19, we can see that the CdS QD is capable of transferring a significant number of holes to NPTZ within the first 10 ps. For $\langle N_0 \rangle = 19$, ∼2 holes can be transferred per CdS QD within 10 ps. In both the CdSe/CdS and the CdSe QDs, k_{AR} well outcompetes k_{HT}, and very few holes are transferred per QD within 10 ps, as seen in Figure 5.8B-C. For the CdSe QDs, the AR lifetime decreases to sub-picosecond level when $\langle N_0 \rangle > 2$ For the CdSe/CdS QD, k_{AR} is similar to that of the CdS QD, yet k_{HT} is much slower than $(10\ \mathrm{ps})^{-1}$ due to the presence of 3ML CdS shell, which forms an energy barrier for the hole to tunnel to the NPTZ ligands. Previously, it had been reported that the hot carriers produced by AR processes could efficiently promote ultrafast electron transfer across energy barriers [160, 161]. Here we did not find this mechanism acting efficiently for hole transfer in the CdSe/CdS QDs despite applying conditions with large $\langle N_0 \rangle$ values, presumably because the effective mass of a hole in the VB is much larger than the effective mass of electrons in the CB, and the cooling rate of hot holes is much faster than that of hot electrons.46 Comparing to the more efficient 5.1 nm CdS QD system, the 2.5 nm CdSe QD has similar hole transfer rates but much faster AR rates; the 3ML CdSe/CdS QD has similar AR rates but much slower hole transfer rates. Therefore, the CdSe and CdSe/CdS QDs investigated here are not able to transfer as many holes per QD as the CdS QDs under multi-excitonic

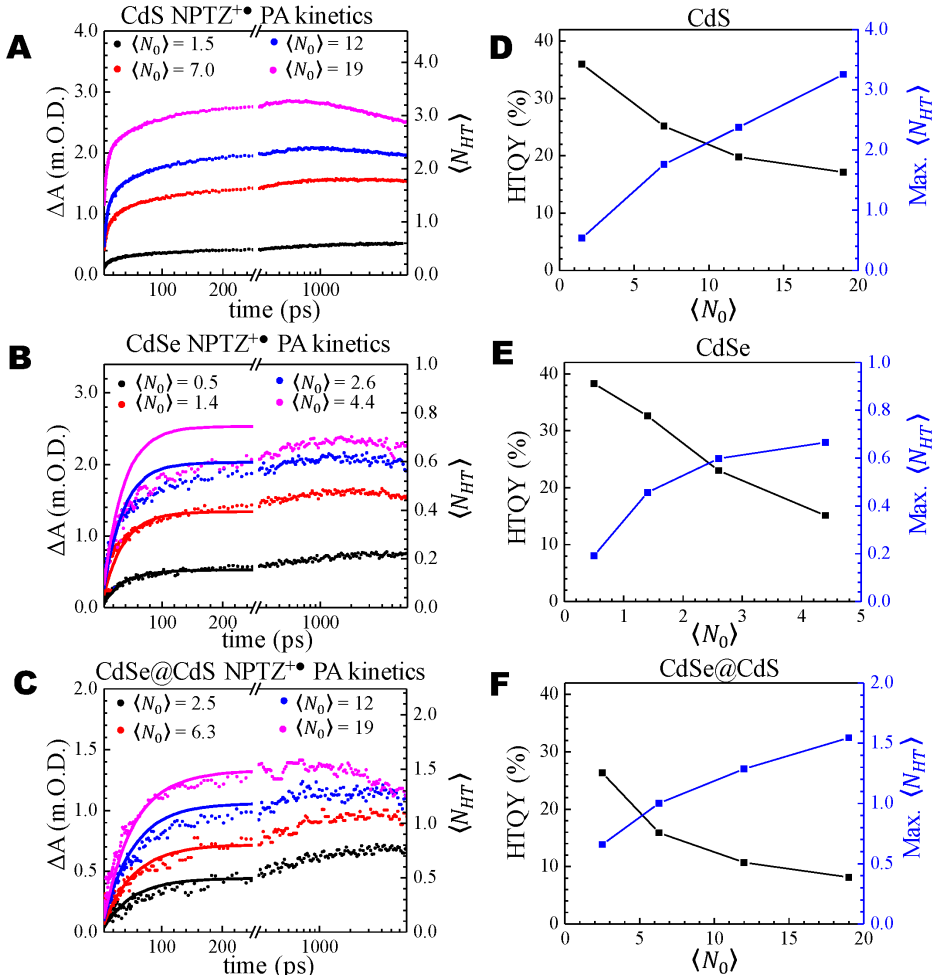

Figure 5.8: (A-C) TA kinetic traces of $NPTZ^{+\bullet}$ radical population monitored at 650 nm for the three types of QDs excited at various fluences and $\langle N_0 \rangle$. The amplitude of $NPTZ^{+\bullet}$ PA signal was de-convoluted to remove the contribution of the trapped hole PA signal. The left axis is associated with the PA signal amplitude, which is linearly related to the average number of holes transferred per QD, shown by the right axis. Solid lines are the results of the kinetic model with a decoupled trap population. (D-F) The hole transfer quantum yield (black) and the maximum number of holes transferred to NPTZ ligands per QD (blue) at each excitation power or $\langle N_0 \rangle$.

conditions.

The hole transfer quantum yield (HTQY) of the three types of QDs measured at each $\langle N_0 \rangle$ were plotted in Figure 5.8D-F. HTQY is defined as the percentage ratio between the maximum number of holes transferred per QD within the 7 ns observation period and the initial number of excitons $\langle N_0 \rangle$. At the lowest value of $\langle N_0 \rangle$ for each type of QD, the HTQY was measured as around 30∼40%. We observe the general trend in Figure 5.8D-F that the HTQY decreases as $\langle N_0 \rangle$ increases. Due to the very fast k_{AR} of 2.5 nm CdSe, the maximum number of holes transferred per QD has already started to saturate at an $\langle N_0 \rangle$ of 4.4. For the larger CdSe/CdS, the number of holes transferred per QD increases almost proportionally as $\langle N_0 \rangle$ increases but is consistently lower than that of the CdS QD at a similar value of $\langle N_0 \rangle$.

The above analysis based on the scaling law of k_{AR} indicates that the hole transfer rates during the period of 10-100 ps would be largely independent of excitation fluences for multi-excitonic QDs with large $\langle N_0 \rangle$ values. However, data for all the QDs in Figure 5.8A-C show that both the hole transfer rate and the number of holes transferred during the period of 10-100 ps increases as $\langle N_0 \rangle$ increases. Roughly 0.5-1.5 holes were transferred to NPTZ per QD transferred in the 10-100 ps period, depending on $\langle N_0 \rangle$. For CdSe and CdSe/CdS QDs, nearly all of hole transfer takes place in this period. For CdS QDs, because the hole transfer rate is competitive with the AR rate, both the holes transferred in the first 10 ps and the holes transferred in the 10-100 ps contribute significantly to the overall number of transferred holes. The observed fluence dependence indicates that multiple carriers must remain on these QDs for longer timescales than expected.

With the introduction of NPTZ ligands, we postulate that multi-exciton dissociation during AR events cause holes to populate surface trap states that are de-coupled from the native states of the QD (Figure 5.9A). These hole trapping states are likely formed as a result of the presence of hole accepting ligands and, thus, have much weaker electron-hole coupling as compared to the electron-hole pair forming an exciton or charges in shallow traps. The de-coupling of the new hole trapping states from native QD states, similar to a charge-separated state, can result in long carrier lifetimes since AR is suppressed. In this mechanism, though the hole transfer rate is generally slower than AR kinetics, holes can first accumulate in the de-coupled surface traps and then further transfer to NPTZ over longer time periods.

5.4.2 Kinetic Modeling and the Role of Hole Traps

To corroborate this mechanism, we developed a kinetic model to simulate the process of trap-mediated hole transfer. However, this first involved developing an understanding of the QDs without NPTZ ligands. A kinetic model was developed to describe trapping, de-trapping, AR, and radiative recombination in native QDs capped with oleate ligands. Hot carrier cooling was ignored, as that is known to be very fast (∼100 fs) relative to the timescales of the other processes considered [183]. The model described in this section was used to simulate the hole trap kinetics without NPTZ, which is shown in Fig. 5.11A-B.

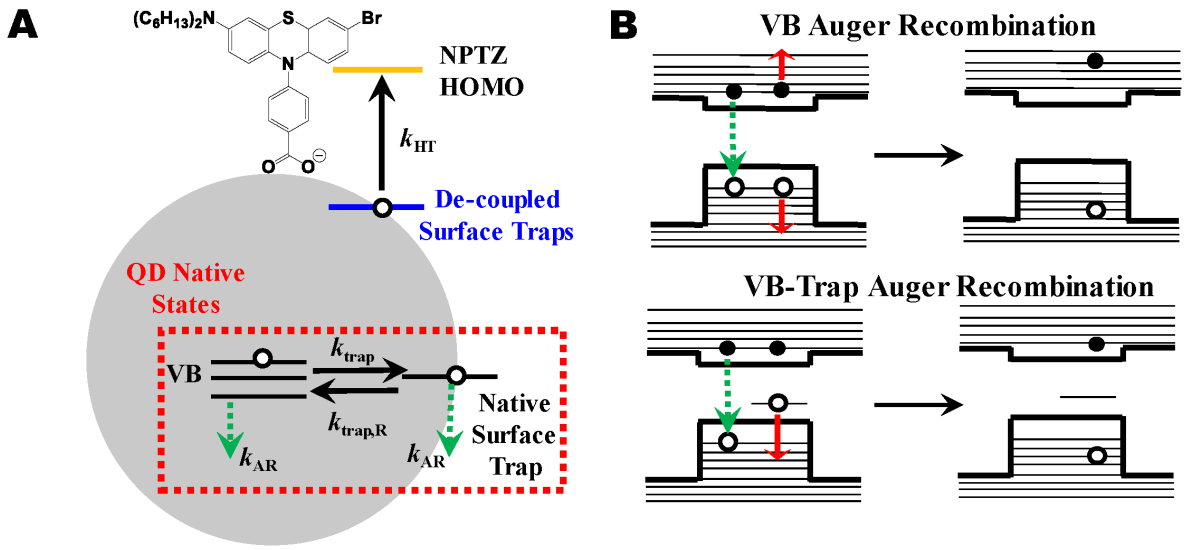

Figure 5.9: A) A schematic showing the energy levels involved in modeling the kinetics of hole transfer and hole trapping under multi-excitonic conditions. B) Auger channels considered for QDs with hole trapping states. The three red arrows are associated with three different trion channels.

In order to maintain a unified description between the strongly and weakly quantum confined regimes of the different QDs studied here, as described below, the kinetic model considers independent electrons and holes and represents AR processes in terms of the different trion pathways in Figure 5.6. The biexciton AR rates ($k_{\mathrm{AR},2}$) extracted from band edge excitation, as discussed in Section 5.3.2, are considered as the combination of channel A (two electrons and one hole, rate $k_{\mathrm{AR},-}$) and channel C (two holes and one electron, rate $k_{\mathrm{AR},+}$). For each non-interacting biexciton there are two possible negative trion channels and two possible positive trion channels, so the trion rates are related to the biexciton rate by $k_{\mathrm{AR},2} = 2k_{\mathrm{AR},+} + 2k_{\mathrm{AR},-}$. To keep the number of independent parameters in the model to a minimum, we made the assumption that the positive and negative trion rates are the same so $k_{\mathrm{AR},+} = k_{\mathrm{AR},-} = \frac{1}{4}k_{\mathrm{AR},2}$. Also, as shown above in Section 5.3.1 by AR calculations comparing VB and VB-trap AR, the rates of pathways involving two valence band holes are similar to those involving one valence band and one trapped hole. The three trion AR pathways, illustrated as A-C in Figure 5.6, were included in the kinetic model with the rate as $1/4k_{\mathrm{AR},2}$. Channel D involving two electrons and a trapped hole is significantly slower and was, therefore, neglected. Additionally, radiative recombination was only allowed for holes at the valence band, as the optical oscillator strengths for radiative recombination of trap states are known to be very weak [184].

Mathematically, the model consists of a set of coupled differential equations describing

the time-evolution of the number of valence band holes (n_{VB}) and the number of trapped holes (n_{trap}) in a QD:

$$\begin{aligned} \dot{n}_{\mathrm{VB}} &= k_{\mathrm{trap},R} n_{\mathrm{trap}} - k_{\mathrm{trap}} n_{\mathrm{VB}} - k_{\mathrm{AR},-} S_{\mathrm{A}} - k_{\mathrm{AR},+} S_{\mathrm{C}} - k_{\mathrm{rad}} n_{\mathrm{VB}} \\ \dot{n}_{\mathrm{trap}} &= -k_{\mathrm{trap},R} n_{\mathrm{trap}} + k_{\mathrm{trap}} n_{\mathrm{VB}} - k_{\mathrm{AR},+} S_{\mathrm{B}} \end{aligned} \tag{5.13}$$

where k_{trap} and $k_{\mathrm{trap},R}$ are the trapping and de-trapping rates, respectively, the $k_{\mathrm{AR},\pm}$ are the positive and negative trion rates referenced above, and S_{A},S_{B},S_{C} describe the non-linear scaling factors of the AR pathways A-C depicted in Figure 5.6.

The scaling factors of the AR processes depend on the type of QD. The smallest particles (2.5 nm CdSe QDs) are in the strongly confined regime, where the confinement energy is comparable to the exciton binding energy (∼300 meV), so electrons and holes are the fundamental quasiparticle in the kinetic model [64]. As there are three independent particles involved in each trion pathway, the scaling factor is a cubic function of the populations [158]. Note that due to charge neutrality, the number of electrons is equal to $n_{\mathrm{VB}} + n_{\mathrm{trap}}$. For pathway A, which involves two electrons and one VB hole,

$$S_{\mathrm{A,conf}} = \binom{n_{\mathrm{VB}} + n_{\mathrm{trap}}}{2} n_{\mathrm{VB}} \,, \tag{5.14}$$

where the first term is the binomial coefficient $\binom{n}{k} = \frac{n!}{k!(n-k)!}$. Pathway B involves one electron, one VB hole, and one trapped hole, so

$$S_{\mathrm{B,conf}} = (n_{\mathrm{VB}} + n_{\mathrm{trap}}) n_{\mathrm{VB}} n_{\mathrm{trap}} \,. \tag{5.15}$$

Finally, pathway C, which involves one electron and two VB holes, has a scaling factor of

$$S_{\mathrm{C,conf}} = (n_{\mathrm{VB}} + n_{\mathrm{trap}}) \binom{n_{\mathrm{VB}}}{2} \,. \tag{5.16}$$

For the larger particles, the electrons and holes form well-bound excitons and thus they do not interact independently. This changes the scaling factor of the AR pathways to be quadratic rather than cubic in the populations [158]. The scaling for pathways A and C is the number of ways to pick two valence band excitons,

$$S_{\mathrm{A}} = S_{\mathrm{C}} = \binom{n_{\mathrm{VB}}}{2} \,, \tag{5.17}$$

while the scaling for pathway B is the number of ways to pick one valence band and one trapped exciton:

$$S_{\mathrm{B}} = n_{\mathrm{VB}} n_{\mathrm{trap}} \,. \tag{5.18}$$

The coupled set of equations 5.13 was solved for a given set of initial conditions using the Gillespie algorithm, a trajectory-based Monte Carlo algorithm with variable time step [185].

An ensemble of N_{traj} =10,000 trajectories was initialized with an average VB population $\langle n_{\text{VB}}(0)\rangle$ and trapped hole population $\langle n_{\text{trap}}(0)\rangle$. The average total initial number of holes per particle $\langle n_{\text{VB}}(0)\rangle + \langle n_{\text{trap}}(0)\rangle$ was taken to correspond to experimental estimates of $\langle N_0\rangle$. Each initial population was distributed according to its respective Poisson distribution so that the number of trajectories with an initial population of m holes in the VB/trap was given by:

$$N_{\text{traj}}(n_{\text{VB/trap}}(0) = m) = N_{\text{traj}} \frac{\left\langle n_{\text{VB/trap}}(0)\right\rangle^m e^{-\langle n_{\text{VB/trap}}(0)\rangle}}{k!}\,. \tag{5.19}$$

On any given trajectory, the populations are always integer values and the dynamic processes are captured as discrete events. These events are chosen by a weighted stochastic process such that the average across all trajectories reproduces the solution to the differential equations. This average across all 10,000 trajectories was calculated as the output of the model and shows a smooth functional form with little to no remaining stochastic noise.

The results of the kinetic model were compared to the experimental kinetics of the broad PA feature at 710 nm via global fittings across a range of excitation fluences. As the time-resolved data from each fluence had slightly different time steps, the data were linearly interpolated to a set of consensus time steps that matched well with the actual time values. This process produced no visual change in the kinetic data and made comparisons and calculations significantly easier to implement. The broad PA signal at 710 nm allows the trap population to be directly probed, however, it also presents the challenge that the proportionality constant (α) between the average number of trapped holes per particle $\langle N_{\text{trap}}\rangle$ and the absorbance $\Delta A(t)$ at 710 nm is experimentally unknown. To fit the experimental data, the proportionality constant α was determined on the fly for each type of QD simulated. This was done by taking the value of $\Delta A(t)$ at an intermediate time (t = 250 ps in general) and finding the conversion to the number of trapped holes that minimized the mean square error between the simulated trajectory and the data across all fluences. This gave the conversion factor as simply the arithmetic mean across all fluences of the ratios between the modeled number of trapped holes per particle ($n_{\text{trap,model}}$) and the optical signal at the same time:

$$\alpha = \left\langle \frac{n_{\text{trap,model}}(t)}{\Delta A(t)} \right\rangle \tag{5.20}$$

The fitting process is shown graphically in Figure 5.10. We began with the extracted AR rates for the trion pathways, estimates of the trapping and de-trapping rates, and an estimate of the initial population of VB holes and trapped holes for each fluence. These parameters were used to generate candidate model kinetic traces for each fluence. The proportionality factor between the optical signal and the number of trapped holes, α, was calculated on the fly as described above. Comparison between the candidate simulated kinetics and the experimentally observed kinetics then informed an update of the initial conditions and trapping and detrapping rates. This update-and-comparison cycle was continued, conducting a search over reasonable parameter space, until a satisfactory fit was established. The final rates resulting from this procedure for each of the different particles are detailed in the Tables 5.3 below, with the associated initial hole population in VB and trap listed in Table 5.4.

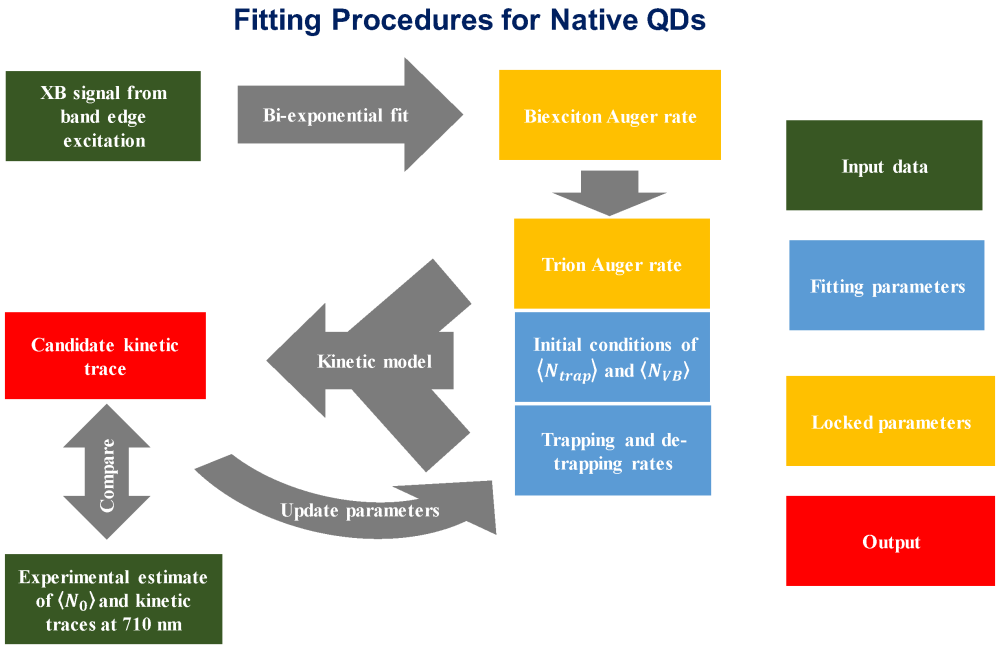

Figure 5.10: Fitting procedures of the native QD model

Table 5.3: Fitting rates for the native particle model

	k_{trap} (ps^{-1})	$k_{\text{trap,R}}$ (ps^{-1})	$k_{\text{AR,+}} = k_{\text{AR,-}}$ (ps^{-1})	k_{rad} (ps^{-1})
CdSe	1.4	1.25	0.0	0.00033
CdSe/CdS	0.15	1.25	0.01	0.00005

To eliminate the effects of cooling dynamics and other very short timescale processes, the fitting started with initial conditions at a pump-probe delay of 3 ps. The rising dynamics of the trap and valence band signals were not considered, but the rapid rise in the trap population suggests that the rates of trapping and de-trapping are quite fast to allow for rapid equilibration at ~3 ps. The initial population of holes in the trap states at 3 ps is meant to capture both direct cooling to the traps and the fast equilibration with the valence band. As shown in Table 5.4, the total number of holes in the initial conditions obtained from the model were found to match the estimates of $\langle N_0 \rangle$ given by experiments.

Figure 5.11 illustrates the PA signal at 710 nm of trapped holes in both native (panels A and B) and NPTZ functionalized quantum dots (panels C and D). The population of trapped holes in the native CdSe and CdSe/CdS QDs decays rapidly before converging to a long-lived plateau level, which represents the single-excitonic state. Most of the trapped holes are consumed within the first 10 ps on a timescale consistent with AR scaling laws and matching the CB bleaching kinetics (Figure 5.12). This observation indicates that these traps participate in AR. In contrast, for the QDs with the NPTZ hole acceptors, the population

Table 5.4: Initial hole population for the native QD model

CdSe			CdSe/CdS		
$\langle N_0 \rangle$	$\langle N_{\mathrm{VB}} \rangle$	$\langle N_{\mathrm{trap}} \rangle$	$\langle N_0 \rangle$	$\langle N_{\mathrm{VB}} \rangle$	$\langle N_{\mathrm{trap}} \rangle$
1.4	0.65	0.65	6.4	4.8	0.7
2.5	1.5	1.5	12	8.1	1.1
4.2	2.1	2.1	19	11.5	1.9

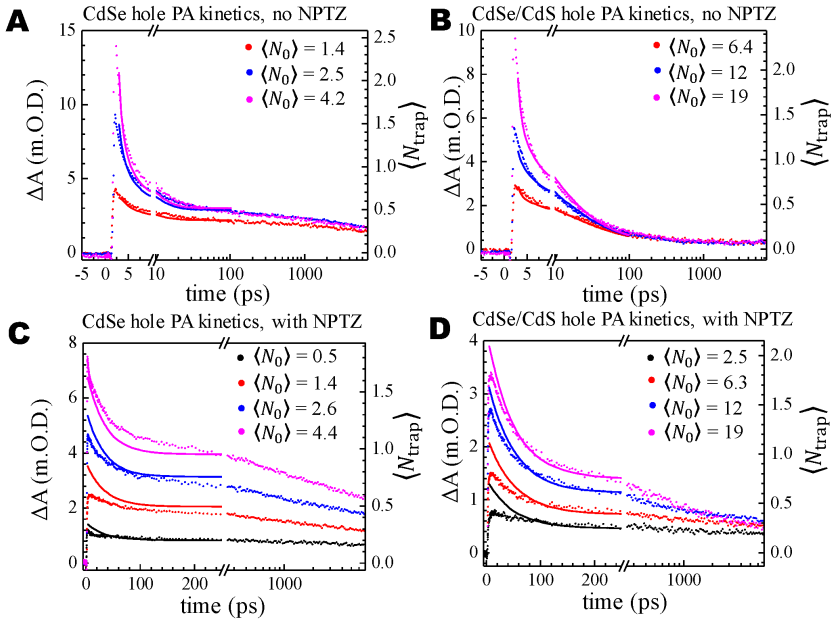

Figure 5.11: TA kinetic traces of the PA signals at 710 nm measured at a series of $\langle N_0 \rangle$ displayed for CdSe QDs with native oleate ligands (A), and with NPTZ ligands (C); CdSe/CdS QDs with native oleate ligands (B), and with NPTZ ligands (D). The modeled kinetics of trapped holes shown as solid lines through the data points of TA signal at 710 nm. The left axis refers to the measured PA signal amplitude, and the right axis refers to the estimated number of trapped holes associated with the optical signal.

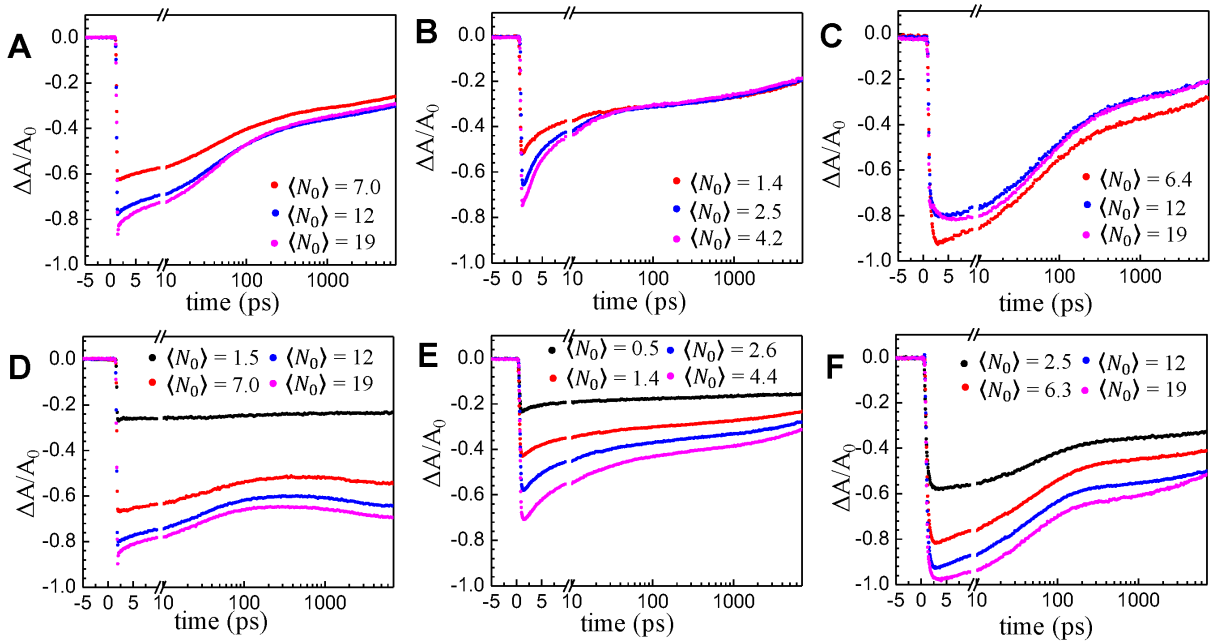

Figure 5.12: The XB decay kinetics of native CdS (A), CdSe (B), and CdSe/CdS (C) QDs show fast Auger recombination dynamics and converge to the single excitonic signal level within 10-100 ps. When NPTZ ligands are introduced, the XB signals of CdS (D), CdSe (E), and CdSe/CdS (F) QDs show fluence-dependent signal levels at long delay times greater than 100 ps due to hole trapping and hole transfer from QD to NPTZ ligands.

decay slows to timescales of 10s-100s ps, and the population plateaus at a level dependent on $\langle N_0 \rangle$. Compared to the kinetics in Figure 5.11A and B, the PA signals of QDs with NPTZ ligands also showed maxima at later times with different amplitudes. These comparisons indicate that the nature of the trapped holes is different from those in the native QDs. The decay curves measured at 710 nm for CdS QDs show similar contrasts between native QDs and QDs with NPTZ ligands.

For the native QDs, the shape of the simulated decay curve is largely governed by the trapping and de-trapping rates, as these rates control the distribution of total hole population into the VB and traps which determine the overall AR rates of the system. Literature results and the observed rapid rise of the trap signal informs that the hole trapping rate in the model should be set as faster than $(1 \text{ ps})^{-1}$ [176, 186]. To globally fit the experimental data across a range of $\langle N_0 \rangle$ and prevent excessive trapping to slow the simulated decay curves, the de-trapping rate has to be comparable to the trapping rate, allowing the trapped holes to establish a rapid equilibrium with the VB holes. In Figure 5.11A and B, the modeling results of the first 100 ps using parameters fit within these constraints agree well with experimental data. For CdSe QDs, the kinetic model estimates that the number of holes in the VB is

comparable to the number of trapped holes, $\langle N_{\text{trap}} \rangle$, represented by the TA signal amplitude at 710 nm. For CdSe/CdS QDs, the majority of holes remain on the VB while only a few holes were trapped, which is consistent with the disfavored energetics of trapping states on CdS surface versus the energy of the CdSe VB [170]. It is important to note here that the equilibrium model employed here focuses on the ultrafast multi-carrier dynamics on the picosecond timescale, and much slower non-radiative and radiative events on the nanosecond timescale are not included in the model. For a single-excitonic QD, the trapping could become irreversible at longer timescales and cause the photoluminescence quantum yield to decrease.

In Figure 5.11C and D, we can see that a fast equilibration between VB and trapped holes is not consistent with the trapped hole PA signals observed in QDs functionalized with NPTZ ligands. When the hole acceptors are present, the decay rates of trapped hole population decrease significantly. The kinetic model for QDs with NPTZ ligands needs to account for kinetic data of both the $NPTZ^{+\bullet}$ at 650 nm and trapped holes at 710 nm. The minimal modification of the native QD kinetic model (given in equation 5.13) needed to capture the dynamics of hole transfer would be the addition of an $NPTZ^{+\bullet}$ population (n_{HT}) as well as the process of hole transfer from the trap state to the NPTZ ligand (with a rate k_{HT}). This translates into a modified set of differential equations for the populations:

$$\begin{aligned} \dot{n}_{\text{VB}} &= k_{\text{trap},R} n_{\text{trap}} - k_{\text{trap}} n_{\text{VB}} - k_{\text{AR},-} S_{\text{A}} - k_{\text{AR},+} S_{\text{C}} - k_{\text{rad}} n_{\text{VB}} \\ \dot{n}_{\text{trap}} &= -k_{\text{trap},R} n_{\text{trap}} + k_{\text{trap}} n_{\text{VB}} - k_{\text{AR},+} S_{\text{B}} - k_{\text{HT}} n_{\text{trap}} \\ \dot{n}_{\text{HT}} &= k_{\text{HT}} n_{\text{trap}} \end{aligned} \tag{5.21}$$

However, the output trajectories of $\langle N_{\text{trap}} \rangle$ and $\langle N_{\text{HT}} \rangle$ from this coupled trap model failed to simultaneously account for the measured kinetic traces of trapped holes at 710 nm and $NPTZ^{+\bullet}$ at 650 nm, respectively. Examples of the simulated kinetics using this coupled trap model are illustrated in Figure 5.13. It is clear that the modeled trapped hole population decays much faster than observed in the experimental data for NPTZ modified QDs in Figure 5.11C-D due to fast AR and equilibration with the VB. If the VB and the traps rapidly equilibrate, as in the native QD model, then the QD will reach a single excitonic state on the timescale of AR. To slow down the decay of trapped hole population, we first considered modifying the parameters of coupled model so that the de-trapping rate is much slower than the fast trapping rate. While this modification prevented the fast loss of trapped hole population, it resulted in the trapping of almost all holes, and subsequently the transfer of all these holes (up to 19 in the case of CdSe/CdS core/shell QD) to the NPTZ ligands, which significantly exceeded the experimentally measured transfer.

Careful examination of how the trapping, de-trapping, and trap AR processes affect the modeled trap population and $NPTZ^{+\bullet}$ population suggested that the trap states and VB must be decoupled. This modification limited the number of holes that could trap, allowing for reasonable levels of hole transfer to the NPTZ ligands. Adjusting the model to incorporate this decoupling corresponds to setting the trapping rate k_{trap}, de-trapping rate $k_{\text{trap,R}}$, and the scaling of the trapped hole AR channel S_{B} all to zero. This decoupling allowed for

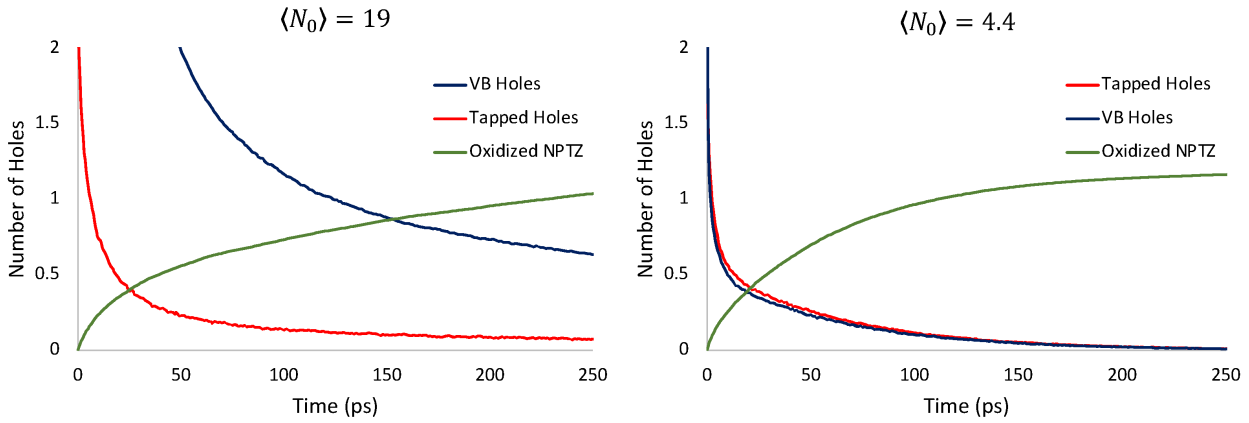

Figure 5.13: Simulated kinetics using the coupled trap model for hole transfer show a rapid decay in the population of trapped holes that is inconsistent with the timescales observed experimentally. Additionally, this model does not capture the plateau of the trapped hole population at a fluence-dependent value as seen experimentally. The initial conditions, trapping, and de-trapping rates for the simulated kinetics shown here were taken from the native QD model for the corresponding fluence, but the qualitative inconsistencies persist across a large range of parameters.

the mathematical elimination of the VB population from the equations that describe hole transfer.

In Figure 5.11C and D, the PA signal shows fluence-dependent plateau levels that last hundreds of ps. The plateau phenomena suggest that only a fraction of the trapped holes can be transferred to NPTZ acceptors. Therefore, the trapped hole population is further divided into 'active' holes which can transfer to NPTZ, and 'passive' holes which are unable to transfer during our observation time window due to kinetic barriers, such as the hole being localized at a trap state far from a NPTZ ligand. Since the surface coverage of NPTZ is only ∼20%, the holes trapped at sites which are not adjacent to a NPTZ ligand would need to undergo a series of slow hole hopping events to reach NPTZ ligands, which have been measured to occur over timescales longer than several nanoseconds [176, 187, 188]. The initial number of trapped holes, $\langle N_{\text{trap}} \rangle$, and the fraction of active traps are fitting parameters for the model. The fraction of active traps falls around 50%, and is held constant across excitation fluences to allow for the model to capture the plateau levels. The simplified equations that describe the populations in the decoupled hole transfer kinetic model are:

$$\begin{aligned} \dot{n}_{\text{trap,active}} &= -k_{\text{HT}} n_{\text{trap,active}} \\ \dot{n}_{\text{HT}} &= -k_{\text{HT}} n_{\text{trap,active}} \end{aligned} \tag{5.22}$$

These equations describe simple exponential transfer from the active trap sites to the NPTZ

Table 5.5: Initial hole populations for the decoupled trap hole transfer model

CdSe				CdSe/CdS			
$\langle N_0 \rangle$	$\langle N_{\text{trap,active}} \rangle$	$\langle N_{\text{trap,passive}} \rangle$	$\langle N_{\text{VB}} \rangle$	$\langle N_0 \rangle$	$\langle N_{\text{trap,active}} \rangle$	$\langle N_{\text{trap,passive}} \rangle$	$\langle N_{\text{VB}} \rangle$
0.5	0.12	0.19	0.19	2.5	0.45	0.25	1.80
1.4	0.34	0.50	0.56	6.3	0.72	0.40	5.18
2.6	0.51	0.75	1.34	12	1.07	0.60	10.33
4.4	0.64	0.94	2.82	19	1.35	0.75	16.90

molecules. $n_{\text{trap,active}}$ is the number of transferable holes in a QD. The sum of the number of passive holes, $n_{\text{trap,passive}}$, and $n_{\text{trap,active}}$ equals the total number of trapped holes, n_{trap}, in the decoupled model. The population in the hole traps could be populated at early time directly by cooling of hot holes or Auger-assisted trapping. The model does not consider the early time dynamics and starts to fit the deconvoluted kinetic data at t = 5 ps. The simultaneous fits of NPTZ and trapped hole populations shown in Figures 3 and 5 of the main text illustrate the general agreement between the timescale of hole transfer and the loss of trapped hole population. The modeled trap population, however, does deviate from experiment for lower fluences and early times. This is likely because this completely decoupled model simplifies the kinetics without considering any AR events involving hole traps or processes such as the continued trapping of AR-generated hot holes.

The procedure for fitting is shown graphically in Figure 5.14. The hole transfer rate constants from de-coupled surface trap states to the NPTZ ligand were extracted from the data of the first 100 ps of the lowest $\langle N_0 \rangle$ for each of the three types of QDs (black kinetic traces in Figure 5.8A-C) with a single exponential functional form. The obtained rate constants are (31±3 ps)$^{-1}$, (73±20 ps)$^{-1}$, and (27±2 ps)$^{-1}$ for CdSe, CdSe/CdS, and CdS QDs, respectively. The remaining fitting parameters were the initial populations of the active traps, $\langle N_{\text{trap,active}} \rangle$, and passive traps, $\langle N_{\text{trap,passive}} \rangle$. The sum of the two trapped hole populations is the total average number of trapped holes per QD, $\langle N_{\text{trap}} \rangle$. The difference between experimentally measured $\langle N_0 \rangle$ and the initial value of $\langle N_{\text{trap}} \rangle$ is assigned to the average initial number of holes in VB, $\langle N_{\text{VB}} \rangle$, which does not affect fittings in the decoupled model. The initial number (at $t = 5$ ps) of $\langle N_{\text{trap,active}} \rangle$ could be inferred to be approximately equal to the maximum of the observed $\langle N_{\text{HT}} \rangle$, the experimentally determined number of holes transferred per QD. Then the portion of holes in passive traps was adjusted such that the long-time plateaus in the hole PA signal matched the model. For the CdSe QDs 40% of trapped holes were allowed to transfer, while for the core/shell CdSe/CdS QDs 65% of trapped holes were allowed to transfer. These values were determined by adjusting the initial conditions until a satisfactory fit was found through an update-and-compare cycle similar to that described above for the native QDs. The output trajectories of $\langle N_{\text{trap}} \rangle$ and $\langle N_{\text{HT}} \rangle$ were simultaneously fit to the measured kinetic traces of trapped holes at 710 nm and NPTZ$^{+\bullet}$ at 650 nm, respectively, using conversion factor α determined on the fly. The initial populations of the model found by the fits are collected in Table 5.5.

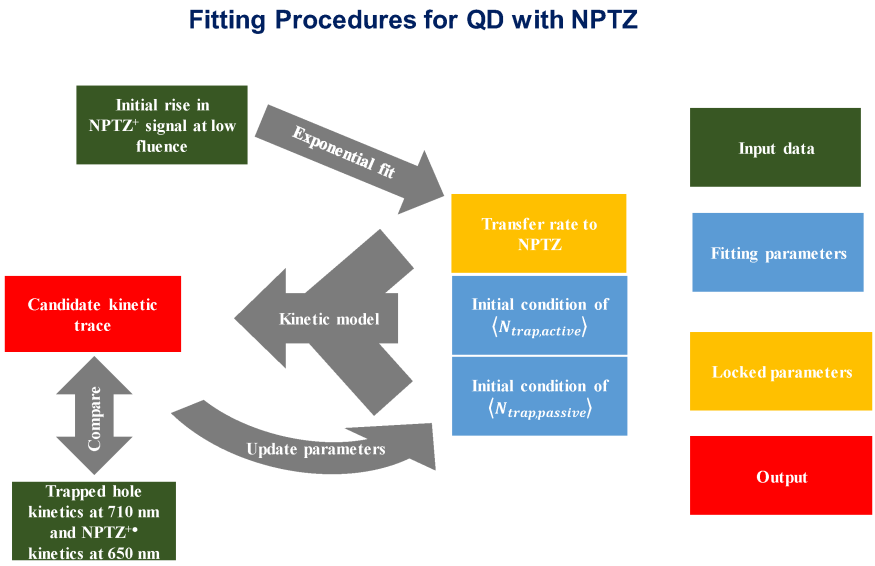

Figure 5.14: Fitting procedures of the hole transfer model of QD-NPTZ system

Simulating transfer using this model shows good agreement with the hole transfer dynamics on CdSe and CdSe/CdS QDs as short time transfer is not significant for these particles. The modeling of the CdS QDs is more difficult, because the significant contribution of short time transfer means that the trap-mediated mechanism cannot account for the full dynamics of hole transfer in this system and other pathways such as direct transfer from VB can also be important.

The long-lived charge carriers are important for improving the efficiency of multi-excitonic hole transfer. The overall results here demonstrate that, in general, QDs with longer AR lifetimes and faster hole transfer rates are preferred for promoting rapid hole transfer under multi-excitonic conditions. However, the observed fluence-dependence of intermediate timescale transfer suggests that the AR kinetics can be circumvented by the long-lived trapping of multiple holes. The failure of the coupled model indicates that the trapped holes in QDs with NPTZ ligands are kinetically de-coupled from the VB. It is possible that hole accepting ligands such as NPTZ alter the energy levels of trapping sites of native QDs or create new trapping sites as they replace the oleate ligands on QD surface. Previous work on hole accepting ligands has shown that their attachment to QDs can produce surface states that are localized toward these ligands [171]. These new trapping states could also be unable to participate in the VB-trap AR channel because their wave function becomes much more separated from carriers in CB and VB states than traps in native QDs, therefore effectively acting as a charge-separated state.

The fitting lines in Figure 5.8 and Figure 5.11, using fitting parameters consistent with both $NPTZ^{+\bullet}$ and trapped hole PA data, show that the decay of the trapped hole population

within the first 250 ps can be largely accounted for by the rise of the $NPTZ^{+\bullet}$ population across various excitation fluences. In the modeling of these NPTZ modified systems, the valence band and the traps are assumed to be completely decoupled. There may, however, still be some level of de-trapping or AR occurring at reduced rates compared to the native QDs, which may account for some of the discrepancies between model and experimental kinetics. For instance, in the case of CdSe with $\langle N_0 \rangle = 4.4$, the simulated decay of trapped holes in Figure 5.11C clearly causes the simulated growth of $NPTZ^{+\bullet}$ population in Figure 5.8B to largely miss the experimental trace, suggesting that some trapped holes could be annihilated by AR without transferring to the NPTZ. Nevertheless, the de-coupled nature of the simplified model captures the major features of the observed decay kinetics and shows large contrast to the coupled model that describes native QDs. This kinetic model allowed us to identify long-lived trapped holes as the reservoir of carrier responsible for the observed fluence dependent hole transfer at intermediate times. Trapping a large number of holes at early times can then be a key to achieving high HTQYs under multi-excitonic conditions, as the holes in these de-coupled trapping states have long lifetimes. In the CdSe and CdSe/CdS QDs studied here, the model suggests that the number of holes trapped is yet only a small fraction of $\langle N_0 \rangle$, resulting in the limited HTQY.

5.5 Conclusion

In summary, we have applied ultrafast TA spectroscopy to examine the hole transfer dynamics from three types of cadmium chalcogenide QDs to NPTZ ligands under multi-excitonic conditions. The results indicate that the transfer of multiple holes from QDs to molecular acceptors at short times is possible when the hole transfer rate and AR rate are comparable. Furthermore, the hole transfer mediated by trapping states occurs on the timescale of 10s-100s ps, much longer than the AR lifetimes of the QDs studied here. The determination of these AR lifetimes and channels through the semiemperical pseudopotential method informed the modeling of the kinetics data which suggested a two-stage transfer mechanism. First, holes can directly transfer to NPTZ ligands under the short lived multi-excitonic state. Next, multiple irreversibly trapped holes in the de-coupled trapping states with long AR lifetimes can gradually transfer charge to acceptors. The results here suggest that careful engineering of hole trap states both in number and kind is required in order to achieve effective hole transfer over non-radiative recombination events when QDs are operating in the multi-excitonic regime.

Chapter 6

Defects and Carrier Recombination in Black Phosphorous

While the preceding chapters have focused on developments using the semiempirical pseudopotential method to understand the atomistic details of nanomaterials, there is also a important place for ab-inito methods such a density functional theory (DFT) to contribute. In particular when the configuration of particular structural defect needs to be determined in detail, and the relevant structure is small enough to be computationally tractable, such an ab-inito method can replace the force fields used to determine the optimized structures such as in Chapters 4 and 5.

In this chapter we use ab-initio DFT calculations along with kinetic modeling to understand carrier recombination in few-layer black phosphorous (BP). Spectroscopy reveals that the mechanism of recombination in these materials evolves from excitionic-dominated to free carrier-dominated as the thickness of the material increases. The kinetic modeling reveals weak Auger recombination and surface recombination effects, and the DFT calculations confirm that this low surface recombination is due to the benign nature of oxygen defects on the surface of BP. Several types of oxygen defects are studied and are found to not create mid-gap trap states. This highlights the potential of BP materials in optoelectronic device applications. The content of this chapter is adapted with permission from Higashitarumizu, N., Uddin, S.Z., Weinberg, D. *et al.* Anomalous thickness dependence of photoluminescence quantum yield in black phosphorous. *Nat. Nanotechnol.* **2023** *18*, 507–513.

6.1 Introduction

Carrier recombination in very thin layers of van der Waals (vdW) semiconductors such as monolayers of transition metal dichalcogenides (TMDC) are excitonic due to reduced Coulomb screening and have been extensively studied [189, 190]. However, exciton to free-carrier transition in these semiconductors is difficult to study as they become indirect with increasing thickness [191]. In contrast, the dominant optical transition in black phosphorus

(BP) remains directat all thicknesses due to the strong interlayer electronic state coupling [192, 193]. Moreover, BP has shown tremendous technological potential in mid-infrared detection and emission [194–198]. BP therefore provides an ideal platform to explore how the recombination mechanism evolves from excitonic to free-carrier nature in a semiconductor. Here we explore the room temperature photoluminescence (PL) quantum yield (QY), a key metric of optoelectronic performance that directly dictates the maximum device efficiency, with BP thickness from monolayer to the bulk limit. We find that, at the same level of defect density, larger exciton binding energy leads to more light emission and monolayer BP has the highest PL QY. This corroborates past findings in monolayer TMDCs, where excitons can recombine completely radiatively [189, 199].We also observe that surface recombination velocity in black phosphorus is two orders of magnitude lower than passivated silicon; the most electrically inactive surface known to modern semiconductor industry [200]. Even when the surface is degraded by oxygen plasma, the surface recombination rate remains unchanged. From density functional theory calculations, we see that oxidation of BP surface does not produce defect levels inside the bandgap, consistent with our finding that the nonradiative surface recombination is independent of the quality of the surface.

Few layers of BP were mechanically exfoliated in nitrogen environment from bulk crystals onto quartz substrates. Optical contrast was used to identify flakes with desired thickness and atomic force microscopy was then used to measure layer thickness [197, 201]. Photoluminescence spectra shown in Figure 6.1A highlights a thickness-dependent optical bandgap ranging from 1.75eV for a monolayer to 0.3eV for bulk BP. A large change in optical bandgap is observed with thickness for up to six layers of BP(Figure 6.1B), beyond which the bandgap redshifts very slowly with thickness (Figure 6.1B inset). A similar dichotomy is also present in the exciton binding energy curated from the experimental and theoretical works in the literature (Figure 6.1C). Up to five layers the exciton binding energy is larger than the average room temperature thermal energy, and the photogenerated carriers will be excitons. Above five layers the binding energy falls below the thermal energy, so photogenerated electron-hole pairs will thermalize and relax as free carriers.

6.2 Steady State Modeling of Carrier Recombination

We first explore the radiative excitonic recombination in black phosphorus. PL spectra of monolayer BP is shown in Figure 6.2A with different generation rates. The PL peak positions for one to five layers of BP do not show any change with generation rate, indicating absence of photodegradation (Figure 6.2B). Calibrated PL QY of BP measured in nitrogen environment decreases drastically from monolayer to five layers at a generation rate of 3.6×10^{26} $cm^{-3}s^{-1}$ (Figure 6.2C). PL QY at different generation rates from monolayer to five layers are shown in Figure 6.2D. We note that the monolayer has the largest PL QY in this range. Large exciton binding energy in monolayers leads to strongly-bound, robust excitons in phosphorene which then recombine radiatively. We also do not observe any signature of exciton-exciton annihilation that plagues other excitonic materials, as illustrated

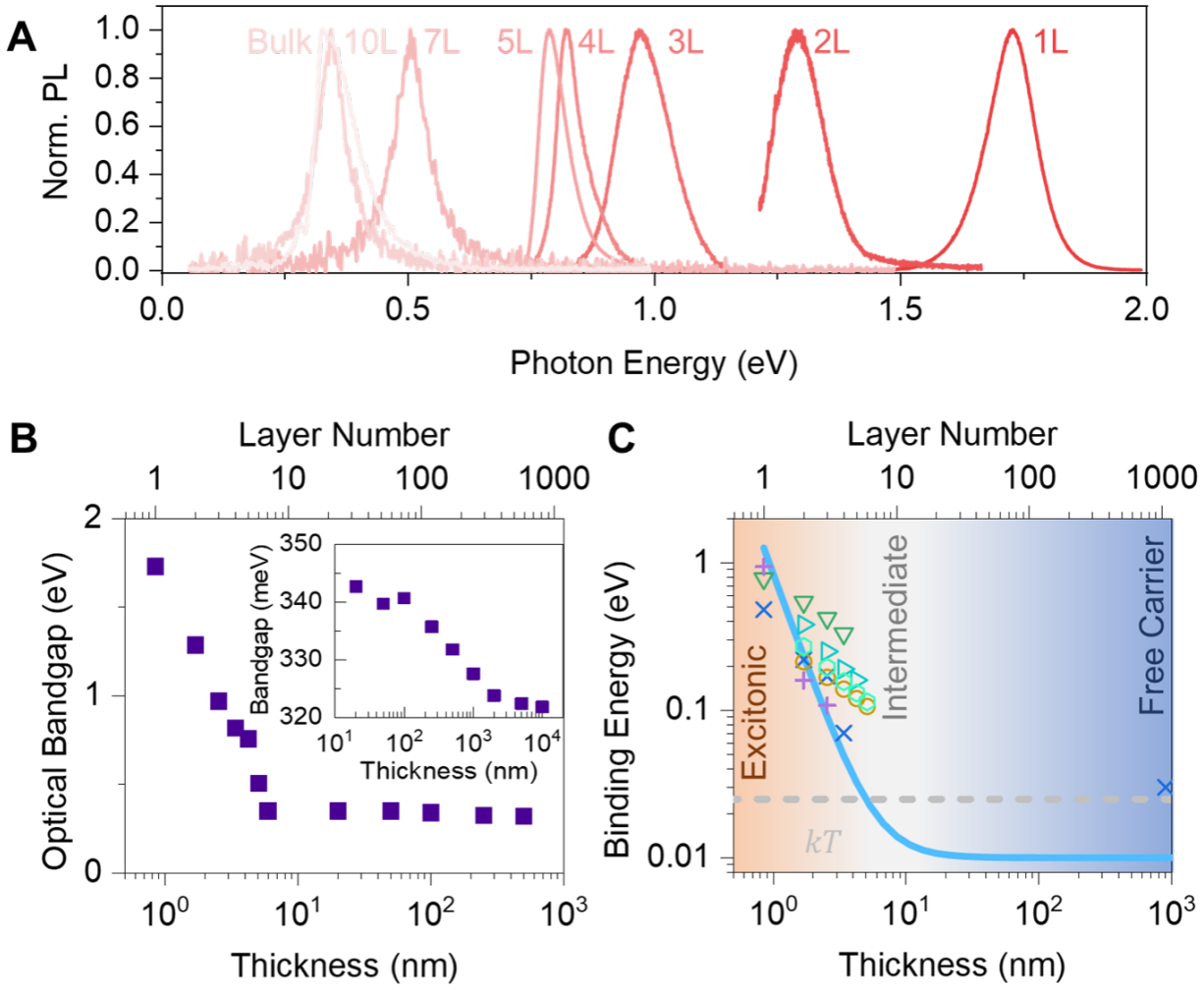

Figure 6.1: (A) Normalized photoluminescence spectra of black phosphorus from monolayer to bulk. (B) Optical Bandgap at different thicknesses, PL peak redshifts slightly with increasing thickness at large thicknesses too. (C) Excitonic binding energy at different thicknesses shows excitonic to free-carrier transition. Thermal energy kT at room temperature is shown where k is the Boltzmann's constant and T is the temperature.

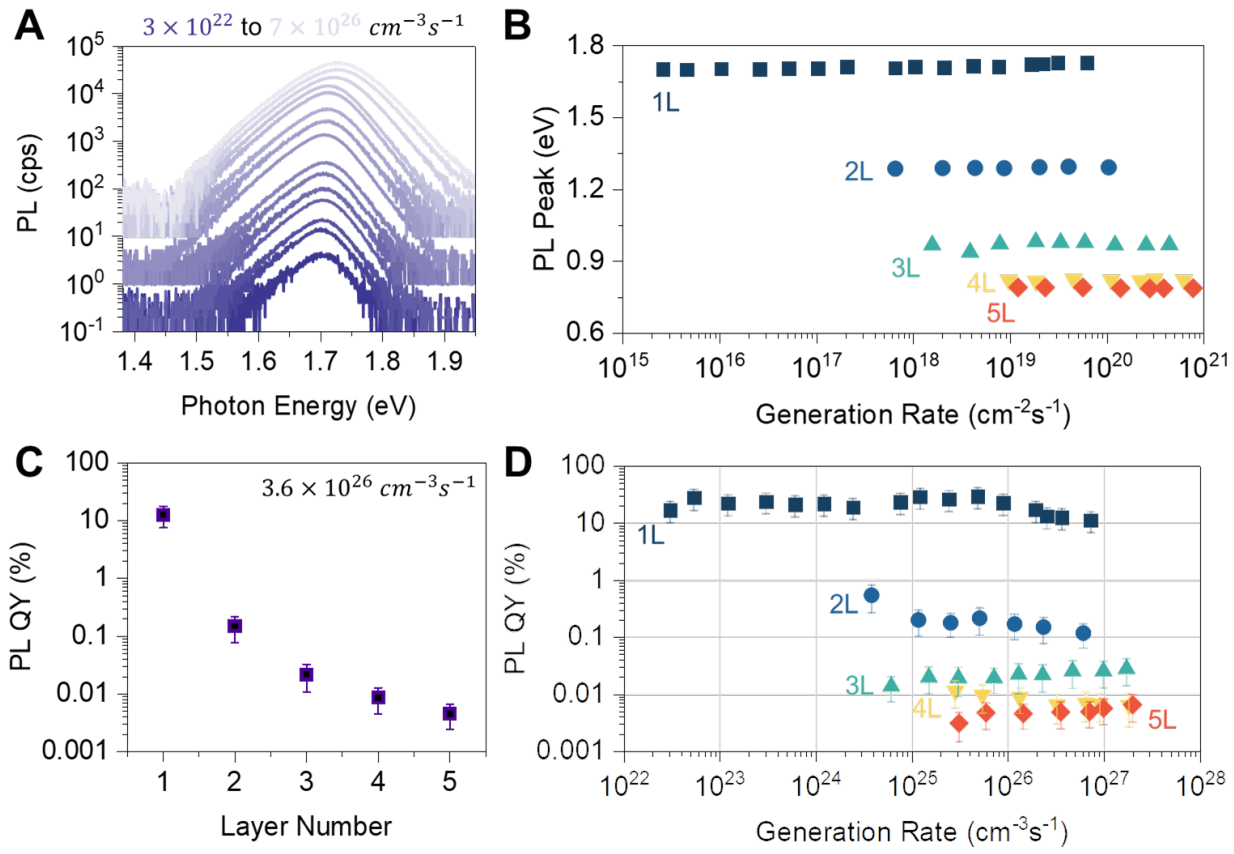

Figure 6.2: (A) PL spectra of monolayer black phosphorus at different generation rates. (B) PL peak position as a function of generation rate and thickness. (C) PL QY at a generation rate of $\sim 3.6 \times 10^{26}$ cm^{-3} s^{-1} for different thickness. (D) PL QY as a function of generation rate for different thicknesses.

in Figure 6.2B. Both facts are reminiscent of monolayers of transition metal dichalcogenides (TMDC), where strongly -bound excitons can recombine completely radiatively despite the presence of large native defect density [189, 194]. PL QY drastically decreases at all pump when BP thickness is increased (Figure 6.2D). Such decrease with thickness is also observed in semiconducting TMDC monolayers and generally has been attributed to the dominance of the indirect transition when thickness is increased beyond monolayer. However, BP remains a direct band gap material when thickness is increased, therefore the observed PL QY decrease with thickness arises from an increase in screening and the decrease in exciton binding energies. As all of these layers are sourced from the same bulk material, our results show that for the same level of defect density, increasing binding energies can lead to increasing radiative recombination.

Before we investigate radiative free-carrier recombination in black phosphorus we first

discuss carrier recombination in conventional free-carrier semiconductors. A nonequilibrium population of electron and holes can relax in a conventional semiconductor mainly through four different pathways: Shockley-Read-Hall (SRH), surface, bimolecular radiative, and Auger recombination. The generation rate G in steady state is balanced by the rates of all of all the recombination channels; for the case of a semiconductor with low background doping:

$$G = \left(A + \frac{2S}{d}\right)\frac{n^2 - n_i^2}{n} + B(n^2 - n_i^2) + 2Cn(n^2 - n_i^2)\,, \tag{6.1}$$

where n is the carrier concentration, n_i is the intrinsic carrier concentration, d is the semiconductor thickness, and A, B, C and S are the SRH, radiative and Auger recombination coefficients, and surface recombination velocity (SRV), respectively. Photoluminescence quantum yield (QY) is calculated according to a standard ABC recombination model as:

$$\mathrm{QY} = \frac{B(n^2 - n_i^2)}{G}\,. \tag{6.2}$$

Defect-mediated nonradiative SRH recombination, and surface recombination dominate at low generation rates and lowers the QY. Nonradiative Auger recombination dominates and lowers QY at high generation rates. The surface recombination rate depends inversely on the semiconductor thickness. Contrary to the excitonic regime, PL QY of BP increases when thickness is increased in the free-carrier regime (Fig. 6.3A). We do not observe a common QY roll-off at all thicknesses at low generation rates, so the SRH process is negligible ($A \approx 0$). We note a thickness dependent QY roll-off at low generation rates, which is indicative of surface recombination ($S \neq 0$). A thickness independent QY roll-off is observed at high generation rates, therefore the Auger process in thick BP is insensitive to the thickness ($C \neq 0, \frac{\partial C}{\partial d} \approx 0$). The radiative bimolecular recombination coefficient B of BP was experimentally measured employing the Shockley-van Roosbroeck relation and is comparable to other reports in the literature. The surface recombination velocity and Auger coefficient are fitted with the available data using the theoretical expression of QY (Figure 6.3B). Note that, the experimental data of all different thicknesses form an overdetermined overcomplete system for two thickness-independent parameters: C and S, and no other combination of values leads to a fit.

Now we can summarize carrier recombination in BP (Fig. 6.3C). At the monolayer limit, excitonic recombination leads to bright luminescence. At the intermediate thickness, QY is low due to surface recombination. At large thicknesses, only Auger recombination limits the QY. Our model can be further modified to include excitons. As excitons are formed from and dissociate into electron and holes, the exciton and carrier concentration are related by:

$$\frac{n_X}{n^2} = K_X e^{E_b/kT} \tag{6.3}$$

where E_b is the exciton binding energy and K_X is the pre-exponential Arrhenius factor. The generation rate can be written as

$$G = \left(A + \frac{2S}{d}\right)\frac{n^2 - n_i^2}{n} + B(n^2 - n_i^2) + B_X e^{E_b/kT} n^2 + 2Cn(n^2 - n_i^2) \tag{6.4}$$

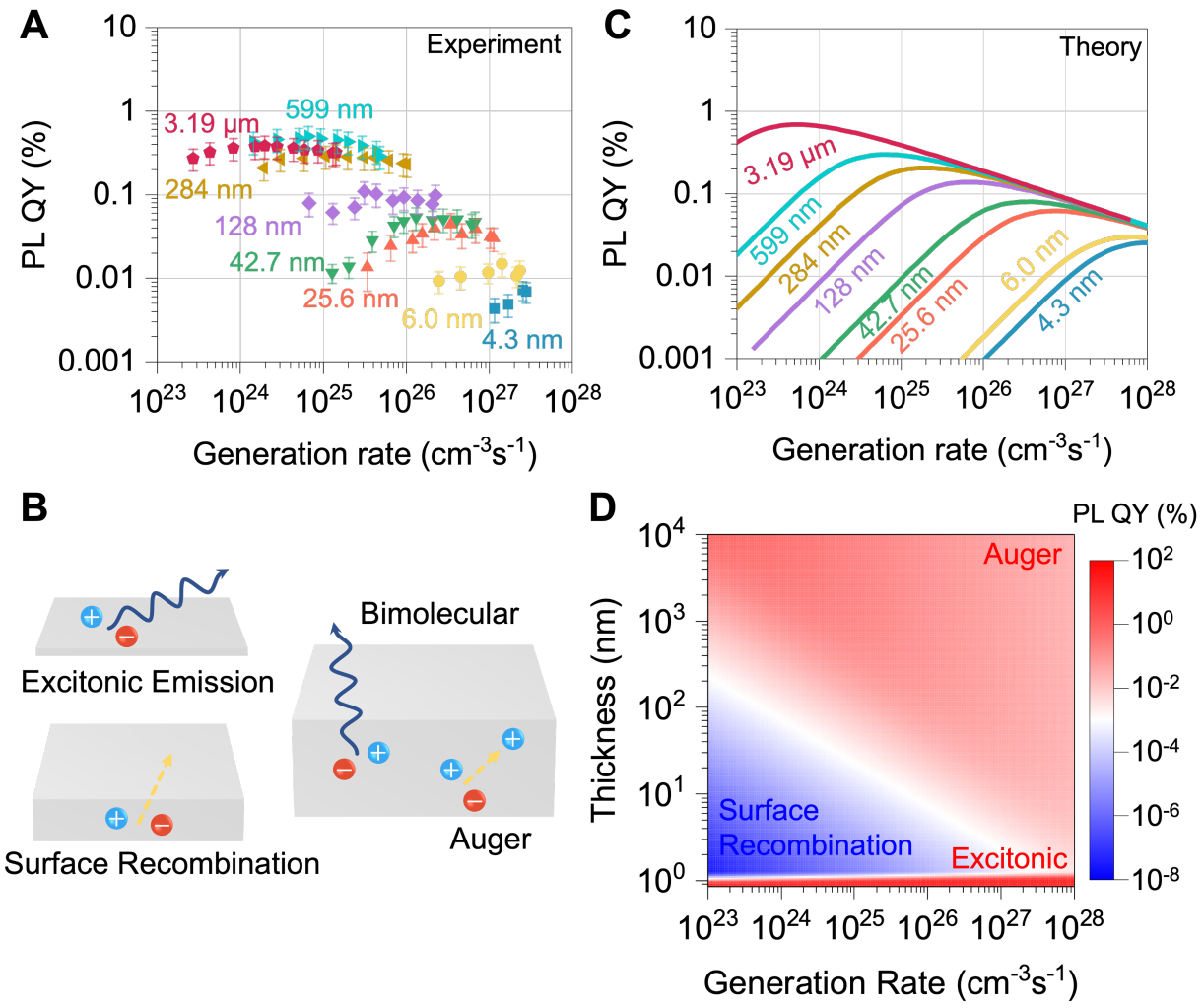

Figure 6.3: (A) Experimental PL QY vs generation rate for different thickness black phosphorus. (B) Dominant recombination pathways active in black phosphorus with different thickness. (C and D) PL QY as a function of generation rate for select and all thicknesses from theoretical model.

The simulated QY vs. generation rate at all thicknesses are shown in Fig. 6.3D which captures the essential features observed in the experiment.

6.3 Modeling Surface Defects

We observed a surface recombination velocity of $(7 \pm 2) \times 10^{-3}$ cm/s and an Auger coefficient of $(6 \pm 1) \times 10^{-43}$ cm^6/s for BP. The Auger coefficient is consistent with other reports on the literature [202], although no work has reported the surface recombination velocity. The observed SRV is two orders of magnitude lower than passivated silicon: the most electrically inactive surface known to modern semiconductor industry (Fig. 6.4A). Such extraordinarily low SRV indicates that BP surface is naturally passivated as far as nonradiative recombination is concerned and could originate from the BP oxide that forms on the BP surface or its van Der Waals nature. Generally, in covalently bonded semiconductors dangling bonds at the surface introduce electronic energy levels inside the normally forbidden gap, referred to as surface or interface states. Such states greatly enhance nonradiative electron–hole recombination at the surface by acting as steppingstones for transitions between the conduction and valence bands. Since each recombination event at the surface requires precisely one electron and one hole, as well as an interface state, surface passivation in conventional semiconductors have two fundamental avenues: either reduce the number of interface surface states, or reduce the concentration of one or other carrier at the surface.

Ab initio density functional theory (DFT) calculations support the conclusion that the BP surface is naturally passivated and resistant to the formation of in-gap defect states from surface oxidation. DFT calculations were carried out using the Quantum Espresso [135–137] package, using the PBE form of the general gradient approximation to the exchange-correlation energy [203] with Grimme-D2 [204] dispersion corrections, which have been shown to sufficiently describe oxygen defects in black phosphorous systems [205]. Core electrons for both oxygen and phosphorous were described using the optimized norm-conserving Vanderbilt pseudopotentials [206] obtained from pseudoDojo [207]. The wavefunctions and electron densities were represented in a plane-wave basis with cutoffs of 65Ry and 520Ry, respectively and the Brillion zone was sampled using a 4x3x1 Monkhorst-Pack (MP) grid [208]. Optimized geometries and lattice parameters for pristine black phosphorous as well as black phosphorous with bridging and terminal oxygen defects were obtained for monolayer through 4 layer systems consisting of a 3x3x1 supercell with over 2nm of vacuum in the out-of-plane direction to avoid interactions with periodic replicas. Forces were minimized to less than 0.001 eV/Åand pressures to less than 0.5 kbar. Using the converged densities at the optimal geometries, band structures were calculated along the path connecting the high symmetry points Gamma-X-M-Y-Gamma. The density of states was calculated using the tetrahedron method [209] using a finer 16x12x1 MP grid. Our calculations examine bridging and terminal oxygen defects on the surface of few-layer black phosphorous (Fig. 6.4B and 6.5A-C), which past work has shown to be the thermodynamically stable oxygen defects in phosphorene. [205] The calculated densities of states show, consistent with other studies [205, 210], that

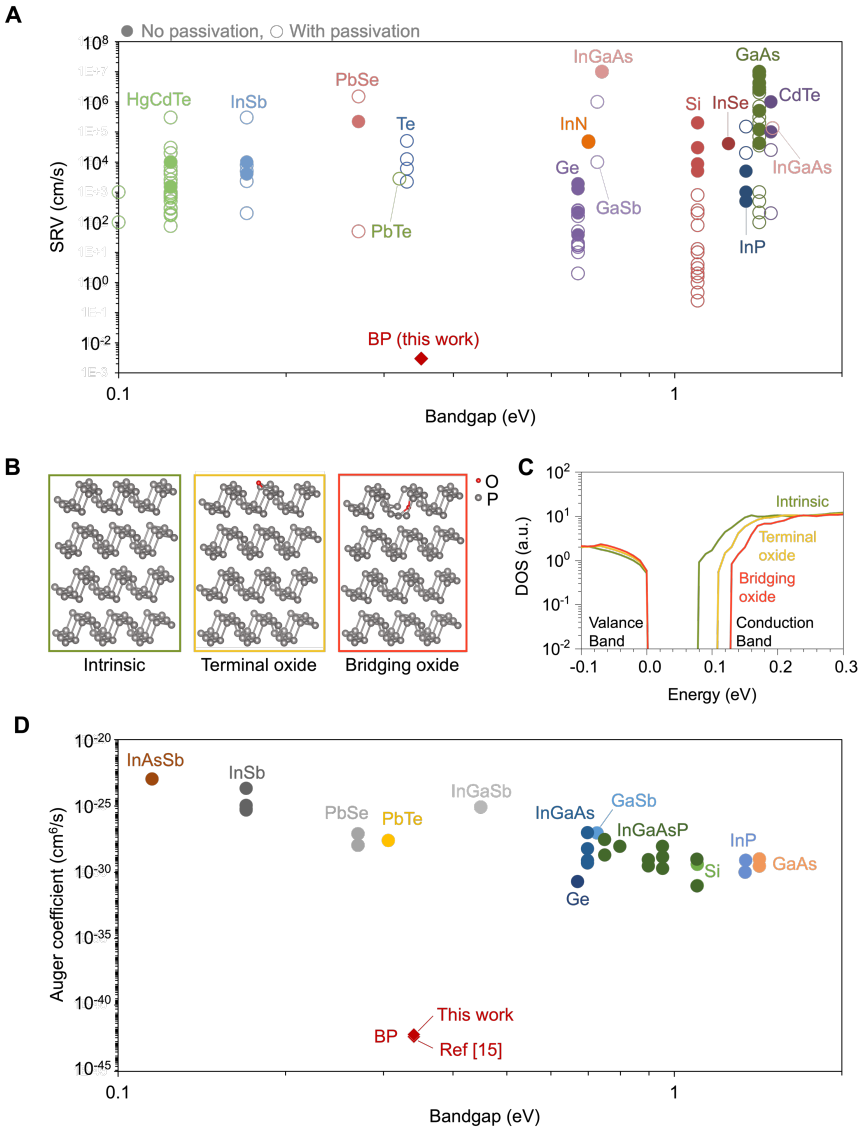

Figure 6.4: (A) Surface recombination velocities (SRV) of different semiconductors with bandgap. (B and C) Schematic crystal structure and DOS for four layer BP: intrinsic, and with a terminal oxide and bridging oxide atom. (D) Auger coefficient of different semiconductors with bandgap.

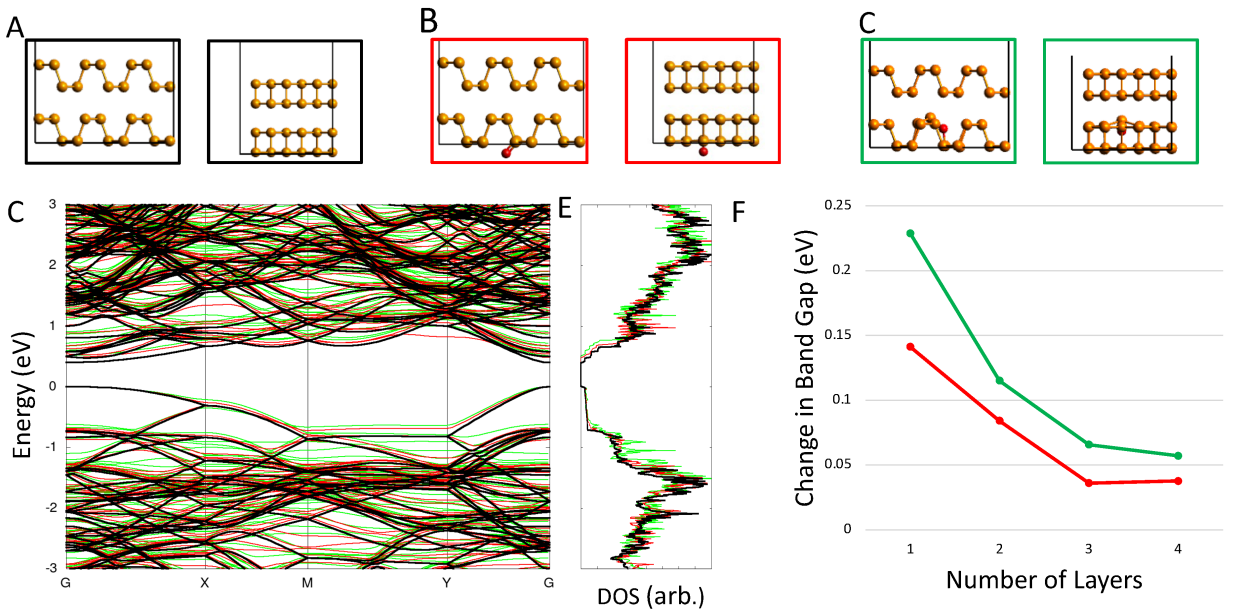

Figure 6.5: Band structures were calculated for pristine black phosphorous (a), black phosphorous with a terminal oxygen defect (b) and black phosphorous with a bridging defect (c) for a number of layers n=1,2,3,4. Shown are the DFT band structures (d) and electronic density of states (e) for the optimized atomic positions for the native system (black), the terminal oxide (red), and the bridging oxide (green) for n=2. These reveal a slight opening of the band gap but no significant modification of the bands or electronic density of states. This band gap modification becomes less pronounced with additional layers (f).

these defects do not form electronic states within the bandgap (Fig. 6.5D) and that a slight broadening opening of the bandgap occurs with oxidation (Fig. 6.4C). This opening of the bandgap is seen to decrease with the number of layers. (Fig. 6.5F). The small energy scale of this band opening, and the fact that any oxide layer is spatially much thinner than the electron Bohr radius, lead us to conclude that the primary reason of low SRV must be from the lack of interface surface electronic states and not due to the exclusion of carriers from the from wide wider bandgap oxide at the surface.

Auger recombination is typically pronounced in small bandgap semiconductors, however in BP the observed Auger coefficient is also low compared to other semiconductors (Fig. 6.4D). This originates from the relationship between the empirical ratio of the Auger lifetime (τ_a) to the radiative lifetime (τ_r) and the bandgap (E_g), which is given by:

$$\frac{\tau_a}{\tau_r} \propto \exp\left(\frac{m_e^*}{m_h^* + m_e^*}\frac{E_g}{kT}\right), \tag{6.5}$$

where m_e^* and m_h^* are the effective masses of electrons and holes, respectively. As electrons

and holes have similar effective masses in BP, the effective mass ratio is much higher than that of other small-bandgap semiconductors and results in suppressed Auger recombination. The effect of low Auger recombination is readily observed experimentally comparing electroluminescence and photoluminescence of BP with that of other small-bandgap semiconductors in the high-injection regime. Note that, the expression for Auger lifetime above is overly simplistic and further calculations that consider the total band structures are necessary. As a consequence of BP oxide being inactive for carrier recombination, the surface can be intentionally damaged without sacrificing optoelectronic quality. We used atomic force microscope (AFM) amplitude and phase maps to examine a 54.2 nm thick BP surface after exfoliation, three, and ten seconds of O_2 plasma. As cleaved surface shows atomically flat surface. The AFM phase contrast depends on the tip–sample energy dissipation, which can change with surface properties [211, 212], thus the uniform phase image guarantee the pristine BP feature. Just in three seconds, small islands were formed indicating a localized oxidation on BP surface. Above ten seconds the surface morphology becomes smooth again suggesting a complete surface oxidation. Although we can see partial and complete oxidation of the surface after plasma treatment, we do not see any effect on the PL QY. Such insensitivity of surface recombination to the surface quality in a nanometer thick flake is indeed striking. Even with the harsh oxidation with plasma treatment, the interface between BP and BP oxide can be steep due to a layer-by-layer oxidation as reported before [213]. We also have observed this insensitivity on other thicknesses.

6.4 Conclusion

In conclusion, we have explored radiative recombination in BP when the nature of recombination varies from excitonic to free carrier. We found that at similar defect density excitonic BP has the highest luminescence efficiency. We also observed lowest surface recombination velocity in BP due to oxidation not creating defect levels inside the bandgap, an observation confirmed by ab-initio DFT calculations. In the future, photonic patterning of BP surface to enhance light outcoupling and integration with photonic circuits becomes possible as surface quality does not determine optoelectronic quality. By expanding upon our approach, surface recombination in other van der Waals system could also be explored.

Chapter 7

Summary

In this dissertation we explored the optical and electronic properties of a wide variety of semiconductor nanomaterials in atomistic detail. We expanded the semiempirical pseudopotential method the lead halide perovskite materials, incorporating the effects of spin-orbit coupling and lattice distortion. We additionally use these atomistic methods to understand the excited state dynamics of diverse nanomaterial systems including core/shell quantum dots and 2D black phosphorous.

We developed a formulation of the semiempirical pseudopotential method that includes the effects of spin-orbit coupling and other non-local terms in the potential. We showed how using a separable form for these non-local terms reduces the computational cost while making a small controlled approximation. This was crucial to our ability to study nanomaterials of experimentally relevant sizes. We applied this method to lead halide perovskite nanocrystals, promising materials for LEDs, quantum light sources, and other diverse aplications that are known for their strong spin-orbit coupling. The atomistic study of these systems allowed for an understanding of how distortion of the nanocrystal structure impacted the exciton fine structure, determining that contrary to some suggestions the ground state exciton is a dark state.

The results of atomistic electronic structure methods also aided in developing kinetic models of excited state species in a variety of nanomaterials. The dynamics of the transfer of holes from muti-excitonic CdSe and CdS NCs was explored as a competition between transfer, trapping, and non-radiative Auger recombination (AR). Pseudopotential calculations provided crucial insight in the AR rates and how those were impacted by the presence of trapped species. A similar kinetic model describing carrier recombination in few-layer black phosphorous was informed by density functional theory calculations of surface oxygen defects which revealed a remarkable insensitivity to surface oxidization.

This dissertation shows both the expansion of the semiemperical pseudopotential method and the application of the method among others to inform studies of material properties and design principles. The combination of theoretical development and experimental collaboration shows the utility of these models to solve practical problems of scientific import. By expanding the applicability of these methods to new materials, these detail atomistic

calculations can now be applied to even more experimentally relevant systems.

Future work on this topic might expand on the perovskite model by better incorporating the effects of the lattice. In this work we focus on static lattice distortion in a single minimized configuration, however this does not fully capture the impact of the perovskite lattice. Electronic excitation will couple to the lattice causing significant polaronic effects. Incorporating those into the model will require expanding on the work of Jasrasaria on exciton-phonon coupling in nanomaterials [54]. This may be complicated as the perovskite structures fluctuate much further from their equilibrium positions than the III-V or II-VI semiconductors do.

A model of exciton-phonon coupling in perovskites could also allow for the resolution of the questions around the temperature dependence of the radiative rates that led to the proposition of a bright excitonic ground state. The rate at which the exctions cool to their ground states, and the temperature dependent structure of the NCs may pay important roles which our current model is unable to resolve. Future work in this direction will require a more sophisticated model of how the pseudopotential should vary with lattice distortion which may require parameterization from a large dataset of *ab initio* calculations at various geometries, including defects. Uncovering the atomistic dynamics of excitations in these systems may pave the route towards more fully understanding the incredible defect tolerance of perovskites.

Bibliography

(1) Alivisatos, A. P. Semiconductor clusters, nanocrystals, and quantum dots. *Science* **1996**, *271*, 933–937.

(2) Scholes, G. D.; Rumbles, G. Excitons in nanoscale systems. *Nat. Mater.* **2006**, *5*, 683–696.

(3) Klimov, V. I. Multicarrier interactions in semiconductor nanocrystals in relation to the phenomena of Auger recombination and carrier multiplication. *Annu. Rev. Condens. Matter Phys.* **2014**, *5*, 285–316.

(4) Efros, A. L.; Brus, L. E. Nanocrystal quantum dots: From discovery to modern development. *ACS Nano* **2021**, *15*, 6192–6210.

(5) Melnychuk, C.; Guyot-Sionnest, P. Multicarrier dynamics in quantum dots. *Chem. Rev.* **2021**, *121*, 2325–2372.

(6) Kagan, C. R.; Bassett, L. C.; Murray, C. B.; Thompson, S. M. Colloidal quantum dots as platforms for quantum information science. *Chem. Rev.* **2021**, *121*, 3186–3233.

(7) Jasrasaria, D.; Weinberg, D.; Philbin, J. P.; Rabani, E. Simulations of nonradiative processes in semiconductor nanocrystals. *J. Chem. Phys.* **2022**, *157*, 020901.

(8) Efros, A.; Efros, A. Interband light absorption in semiconductor spheres. *Sov. Phys. Semicond.* **1982**, *16*, 772–775.

(9) Murray, C. B.; Norris, D. J.; Bawendi, M. G. Synthesis and characterization of nearly monodisperse CdE (E = S, Se, Te) semiconductor nanocrystallites. *J. Am. Chem. Soc.* **1993**, *115*, 8706–8715.

(10) Wang, L. W.; Zunger, A. Electronic Structure Pseudopotential Calculations of Large ($\sim$ 1000 Atoms) Si Quantum Dots. *J. Phys. Chem.* **1994**, *98*, 2158–2165.

(11) Dabbousi, B. O.; Rodriguez-Viejo, J.; Mikulec, F. V.; Heine, J. R.; Mattoussi, H.; Ober, R.; Jensen, K. F.; Bawendi, M. G. (CdSe)ZnS core-shell quantum dots: Synthesis and characterization of a size series of highly luminescent nanocrystallites. *J. Phys. Chem. B* **1997**, *101*, 9463–9475.

(12) Efros, A. L.; Rosen, M. The electronic structure of semiconductor nanocrystals. *Annu. Rev. Mater. Sci.* **2000**, *30*, 475–521.

(13) Rabani, E.; Baer, R. Theory of multiexciton generation in semiconductor nanocrystals. *Chem. Phys. Lett.* **2010**, *496*, 227–235.

(14) Boles, M. A.; Engel, M.; Talapin, D. V. Self-assembly of colloidal nanocrystals: From intricate structures to functional materials. *Chem. Rev.* **2016**, *116*, 11220–11289.

(15) Weiss, E. A. Influence of shape anisotropy on the emission of low-dimensional semiconductors. *ACS Nano* **2021**, *15*, 3568–3577.

(16) Rossetti, R.; Nakahara, S.; Brus, L. E. Quantum size effects in the redox potentials, resonance Raman spectra, and electronic spectra of CdS crystallites in aqueous solution. *J. Chem. Phys.* **1983**, *79*, 1086–1088.

(17) Ekimov, A. I.; Hache, F.; Schanne-Klein, M. C.; Ricard, D.; Flytzanis, C.; Kudryavtsev, I. A.; Yazeva, T. V.; Rodina, A. V.; Efros, A. L. Absorption and intensity-independent photoluminescence measurements on CdSe quantum dots: Assignment of the first electronic transitions. *J. Opt. Soc. Am. B* **1993**, *10*, 100–107.

(18) Norris, D. J.; Sacra, A.; Murray, C. B.; Bawendi, M. G. Measurement of the size dependent hole spectrum in CdSe quantum dots. *Phys. Rev. Lett.* **1994**, *72*, 2612–2615.

(19) Norris, D. J.; Bawendi, M. G. Measurement and assignment of the size-dependent optical spectrum in CdSe quantum dots. *Phys. Rev. B* **1996**, *53*, 16338–16346.

(20) Nirmal, M.; Murray, C. B.; Bawendi, M. G. Fluorescence-line narrowing in CdSe quantum dots: Surface localization of the photogenerated exciton. *Phys. Rev. B* **1994**, *50*, 2293–2300.

(21) Nirmal, M.; Norris, D. J.; Kuno, M.; Bawendi, M. G.; Efros, A. L.; Rosen, M. Observation of the "Dark Exciton" in CdSe Quantum Dots. *Phys. Rev. Lett.* **1995**, *75*, 3728–3731.

(22) Norris, D. J.; Efros, A. L.; Rosen, M.; Bawendi, M. G. Size dependence of exciton fine structure in CdSe quantum dots. *Phys. Rev. B* **1996**, *53*, 16347–16354.

(23) Efros, A. L.; Rosen, M.; Kuno, M.; Nirmal, M.; Norris, D. J.; Bawendi, M. Band-edge exciton in quantum dots of semiconductors with a degenerate valence band: Dark and bright exciton states. *Phys. Rev. B* **1996**, *54*, 4843–4856.

(24) Brus, L. E. A simple model for the ionization potential, electron affinity, and aqueous redox potentials of small semiconductor crystallites. *The Journal of Chemical Physics* **1983**, *79*, 5566–5571.

(25) Ekimov, A.; Efros, A.; Onushchenko, A. Quantum size effect in semiconductor microcrystals. *Solid State Communications* **1985**, *56*, 921–924.

(26) Pidgeon, C. R.; Brown, R. N. Interband Magneto-Absorption and Faraday Rotation in InSb. *Phys. Rev.* **1966**, *146*, 575–583.

(27) Sercel, P. C.; Efros, A. L. Band-Edge Exciton in CdSe and Other II-VI and III-V Compound Semiconductor Nanocrystals - Revisited. *Nano Lett.* **2018**, *18*, 4061–4068.

(28) Cohen, M. L.; Bergstresser, T. K. Band structures and pseudopotential form factors for fourteen semiconductors of the diamond and zinc-blende structures. *Phys. Rev.* **1966**, *141*, 789–796.

(29) Rama Krishna, M. V.; Friesner, R. A. Exciton spectra of semiconductor clusters. *Phys. Rev. Lett.* **1991**, *67*, 629–632.

(30) Wang, L.-W.; Zunger, A. Pseudopotential calculations of nanoscale CdSe quantum dots. *Phys. Rev. B* **1996**, *53*, 9579–9582.

(31) Rabani, E.; Hetenyi, B.; Berne, B. J.; Brus, L. E. Electronic properties of CdSe nanocrystals in the absence and presence of a dielectric medium. *J. Chem. Phys.* **1999**, *110*, 5355–5369.

(32) Sewall, S. L.; Cooney, R. R.; Kambhampati, P. Experimental tests of effective mass and atomistic approaches to quantum dot electronic structure: Ordering of electronic states. *Appl. Phys. Lett.* **2009**, *94*, 243116.

(33) Califano, M.; Franceschetti, A.; Zunger, A. Temperature dependence of excitonic radiative decay in CdSe quantum dots: The role of surface hole traps. *Nano Lett.* **2005**, *5*, 2360–2364.

(34) Jasrasaria, D.; Philbin, J. P.; Yan, C.; Weinberg, D.; Alivisatos, A. P.; Rabani, E. Sub-bandgap photoinduced transient absorption features in CdSe nanostructures: The role of trapped holes. *J. Phys. Chem. C* **2020**, *124*, 17372–17378.

(35) Wang, L.-W.; Kim, J.; Zunger, A. Electronic structures of [110]-faceted self-assembled pyramidal InAs/GaAs quantum dots. *Phys. Rev. B* **1999**, *59*, 5678–5687.

(36) Mattila, T.; Wang, L.-W.; Zunger, A. Electronic consequences of lateral composition modulation in semiconductor alloys. *Phys. Rev. B* **1999**, *59*, 15270–15284.

(37) Kim, J.; Wang, L.-W.; Zunger, A. Comparison of the electronic structure of InAs/GaAs pyramidal quantum dots with different facet orientations. *Phys. Rev. B* **1998**, *57*, R9408–R9411.

(38) Schlüter, M.; Chelikowsky, J. R.; Louie, S. G.; Cohen, M. L. Self-consistent pseudopotential calculations for Si (111) surfaces: Unreconstructed (1×1) and reconstructed (2×1) model structures. *Phys. Rev. B* **1975**, *12*, 4200–4214.

(39) Wang, L.-W.; Zunger, A. Local-density-derived semiempirical pseudopotentials. *Phys. Rev. B* **1995**, *51*, 17398–17416.

(40) Fu, H.; Zunger, A. Local-density-derived semiempirical nonlocal pseudopotentials for InP with applications to large quantum dots. *Phys. Rev. B* **1997**, *55*, 1642–1653.

(41) Wang, L.-W.; Zunger, A. High-energy excitonic transitions in CdSe quantum dots. *J. Phys. Chem. B* **1998**, *102*, 6449–6454.

(42) Williamson, A.; Zunger, A. Pseudopotential study of electron-hole excitations in colloidal free-standing InAs quantum dots. *Phys. Rev. B* **2000**, *61*, 1978–1991.

(43) Fu, H.; Wang, L.-W.; Zunger, A. Applicability of the $\mathbf{k} \cdot \mathbf{p}$ method to the electronic structure of quantum dots. *Phys. Rev. B* **1998**, *57*, 9971–9987.

(44) Wang, L. W.; Williamson, A. J.; Zunger, A.; Jiang, H.; Singh, J. Comparison of the $k \cdot p$ and direct diagonalization approaches to the electronic structure of InAs/GaAs quantum dots. *Applied Physics Letters* **2000**, *76*, 339–341.

(45) Wang, H.-C.; Bao, Z.; Tsai, H.-Y.; Tang, A.-C.; Liu, R.-S. Perovskite Quantum Dots and Their Application in Light-Emitting Diodes. *Small* **2018**, *14*, 1702433.

(46) Dirin, D. N.; Protesescu, L.; Trummer, D.; Kochetygov, I. V.; Yakunin, S.; Krumeich, F.; Stadie, N. P.; Kovalenko, M. V. Harnessing Defect-Tolerance at the Nanoscale: Highly Luminescent Lead Halide Perovskite Nanocrystals in Mesoporous Silica Matrixes. *Nano Letters* **2016**, *16*, PMID: 27550860, 5866–5874.

(47) Swarnkar, A.; Marshall, A. R.; Sanehira, E. M.; Chernomordik, B. D.; Moore, D. T.; Christians, J. A.; Chakrabarti, T.; Luther, J. M. Quantum dot-induced phase stabilization of $CsPbI_3$ perovskite for high-efficiency photovoltaics. *Science* **2016**, *354*, 92–95.

(48) Aharonovich, I.; Englund, D.; Toth, M. Solid-state single-photon emitters. *Nature Photonics* **2016**, *10*, 631–641.

(49) Park, Y.-S.; Guo, S.; Makarov, N. S.; Klimov, V. I. Room Temperature Single-Photon Emission from Individual Perovskite Quantum Dots. *ACS Nano* **2015**, *9*, PMID: 26312994, 10386–10393.

(50) Utzat, H.; Sun, W.; Kaplan, A. E. K.; Krieg, F.; Ginterseder, M.; Spokoyny, B.; Klein, N. D.; Shulenberger, K. E.; Perkinson, C. F.; Kovalenko, M. V.; Bawendi, M. G. Coherent single-photon emission from colloidal lead halide perovskite quantum dots. *Science* **2019**, *363*, 1068–1072.

(51) Lv, Y.; Yin, C.; Zhang, C.; Yu, W. W.; Wang, X.; Zhang, Y.; Xiao, M. Quantum Interference in a Single Perovskite Nanocrystal. *Nano Letters* **2019**, *19*, PMID: 31185175, 4442–4447.

(52) Dastidar, S.; Hawley, C. J.; Dillon, A. D.; Gutierrez-Perez, A. D.; Spanier, J. E.; Fafarman, A. T. Quantitative Phase-Change Thermodynamics and Metastability of Perovskite-Phase Cesium Lead Iodide. *The Journal of Physical Chemistry Letters* **2017**, *8*, PMID: 28256139, 1278–1282.

(53) Quarti, C.; Mosconi, E.; Ball, J. M.; D'Innocenzo, V.; Tao, C.; Pathak, S.; Snaith, H. J.; Petrozza, A.; De Angelis, F. Structural and optical properties of methylammonium lead iodide across the tetragonal to cubic phase transition: implications for perovskite solar cells. *Energy Environ. Sci.* **2016**, *9*, 155–163.

(54) Jasrasaria, D.; Rabani, E. Interplay of surface and interior modes in exciton-phonon coupling at the nanoscale. *Nano Lett.* **2021**, *21*, 8741–8748.

(55) Chelikowsky, J. R.; Kronik, L.; Vasiliev, I. Time-dependent density-functional calculations for the optical spectra of molecules, clusters, and nanocrystals. *J. Phys. Condens. Matter* **2003**, *15*, R1517–R1547.

(56) Shulenberger, K. E.; Coppieters 't Wallant, S. C.; Klein, M. D.; McIsaac, A. R.; Goldzak, T.; Berkinsky, D. B.; Utzat, H.; Barotov, U.; Van Voorhis, T.; Bawendi, M. G. Resolving the triexciton recombination pathway in CdSe/CdS nanocrystals through state-specific correlation measurements. *Nano Lett.* **2021**, *21*, 7457–7464.

(57) Song, Y.; Liu, R.; Wang, Z.; Xu, H.; Ma, Y.; Fan, F.; Voznyy, O.; Du, J. Enhanced emission directivity from asymmetrically strained colloidal quantum dots. *Sci. Adv.* **2022**, *8*, eabl8219.

(58) Degoli, E.; Guerra, R.; Iori, F.; Magri, R.; Marri, I.; Pulci, O.; Bisi, O.; Ossicini, S. Ab initio calculations of luminescence and optical gain properties in silicon nanostructures. *C. R. Phys.* **2009**, *10*, 575–586.

(59) Friesner, R. A. Ab initio quantum chemistry: Methodology and applications. *Proc. Natl. Acad. Sci. U.S.A.* **2005**, *102*, 6648–6653.

(60) Voznyy, O.; Mokkath, J. H.; Jain, A.; Sargent, E. H.; Schwingenschlögl, U. Computational study of magic-size CdSe clusters with complementary passivation by carboxylic and amine ligands. *J. Phys. Chem. C* **2016**, *120*, 10015–10019.

(61) Wall, M. R.; Neuhauser, D. Extraction, through filter-diagonalization, of general quantum eigenvalues or classical normal mode frequencies from a small number of residues or a short-time segment of a signal. I. Theory and application to a quantum-dynamics model. *J. Chem. Phys.* **1995**, *102*, 8011–8022.

(62) Toledo, S.; Rabani, E. Verly large electronic structure calculations using an out-of-core filter-diagonalization method. *J. Comput. Phys.* **2002**, *180*, 256–269.

(63) Rohlfing, M.; Louie, S. G. Electron-hole excitations and optical spectra from first principles. *Phys. Rev. B* **2000**, *62*, 4927–4944.

(64) Philbin, J. P.; Rabani, E. Electron-hole correlations govern Auger recombination in nanostructures. *Nano Lett.* **2018**, *18*, 7889–7895.

(65) Becker, M. A.; Vaxenburg, R.; Nedelcu, G.; Sercel, P. C.; Shabaev, A.; Mehl, M. J.; Michopoulos, J. G.; Lambrakos, S. G.; Bernstein, N.; Lyons, J. L.; Stöferle, T.; Mahrt, R. F.; Kovalenko, M. V.; Norris, D. J.; Rainò, G.; Efros, A. L. Bright triplet excitons in caesium lead halide perovskites. *Nature* **2018**, *553*, 189–193.

(66) Sercel, P. C.; Lyons, J. L.; Wickramaratne, D.; Vaxenburg, R.; Bernstein, N.; Efros, A. L. Exciton Fine Structure in Perovskite Nanocrystals. *Nano Letters* **2019**, *19*, 4068–4077.

(67) Biffi, G.; Cho, Y.; Krahne, R.; Berkelbach, T. C. Excitons and Their Fine Structure in Lead Halide Perovskite Nanocrystals from Atomistic GW/BSE Calculations. *The Journal of Physical Chemistry C* **2023**, *127*, 1891–1898.

(68) Weinberg, D.; Park, Y.; Limmer, D. T.; Rabani, E. Size-Dependent Lattice Symmetry Breaking Determines the Exciton Fine Structure of Perovskite Nanocrystals. *Nano Letters* **2023**, *23*, 4997–5003.

(69) Hybertsen, M. S.; Louie, S. G. Spin-orbit splitting in semiconductors and insulators from the ab initio pseudopotential. *Phys. Rev. B* **1986**, *34*, 2920–2922.

(70) Bester, G.; Nair, S.; Zunger, A. Pseudopotential calculation of the excitonic fine structure of million-atom self-assembled $In_{1-x}Ga_xAs/GaAs$ quantum dots. *Phys. Rev. B* **2003**, *67*, 161306.

(71) Cao, Y. W.; Banin, U. Growth and properties of semiconductor core/shell nanocrystals with InAs cores. *J. Am. Chem. Sci.* **2000**, *122*, 9692–9702.

(72) Reiss, P.; Protière, M.; Li, L. Core/shell semiconductor nanocrystals. *Small* **2009**, *5*, 154–168.

(73) Wuister, S. F.; de Mello Donegá, C.; Meijerink, A. Influence of thiol capping on the exciton luminescence and decay kinetics of CdTe and CdSe quantum dots. *J. Phys. Chem. B* **2004**, *108*, 17393–17397.

(74) Guzelturk, B.; Cotts, B. L.; Jasrasaria, D.; Philbin, J. P.; Hanifi, D. A.; Koscher, B. A.; Balan, A. D.; Curling, E.; Zajac, M.; Park, S.; Yazdani, N.; Nyby, C.; Kamysbayev, V.; Fischer, S.; Nett, Z.; Shen, X.; Kozina, M. E.; Lin, M. F.; Reid, A. H.; Weathersby, S. P.; Schaller, R. D.; Wood, V.; Wang, X.; Dionne, J. A.; Talapin, D. V.; Alivisatos, A. P.; Salleo, A.; Rabani, E.; Lindenberg, A. M. Dynamic lattice distortions driven by surface trapping in semiconductor nanocrystals. *Nat. Commun.* **2021**, *12*, 1–9.

(75) Enright, M. J.; Jasrasaria, D.; Hanchard, M. M.; Needell, D. R.; Phelan, M. E.; Weinberg, D.; McDowell, B. E.; Hsiao, H.-W.; Akbari, H.; Kottwitz, M.; Potter, M. M.; Wong, J.; Zuo, J.-M.; Atwater, H. A.; Rabani, E.; Nuzzo, R. G. Role of the atomic structure on exciton dynamics and photoluminescence in NIR emissive InAs/InP/ZnSe quantum dots. *J. Phys. Chem. C* **2022**, *126*, 7576–7587.

(76) Ekimov, A. I.; Efros, A. L.; Onushchenko, A. A. Quantum size effect in semiconductor microcrystals. *Solid State Commun.* **1985**, *56*, 921–924.

(77) Philbin, J. P.; Rabani, E. Auger recombination lifetime scaling for type-I and quasi-type-II core/shell quantum dots. *J. Phys. Chem. Lett.* **2020**, *11*, 5132–5138.

(78) Ondry, J. C.; Philbin, J. P.; Lostica, M.; Rabani, E.; Alivisatos, A. P. Resilient pathways to atomic attachment of quantum dot dimers and artificial solids from faceted CdSe quantum dot building blocks. *ACS Nano* **2019**, *13*, 12322–12344.

(79) Cui, J.; Panfil, Y. E.; Koley, S.; Shamalia, D.; Waiskopf, N.; Remennik, S.; Popov, I.; Oded, M.; Banin, U. Colloidal quantum dot molecules manifesting quantum coupling at room temperature. *Nat. Commun.* **2019**, *10*, 5401.

(80) Zunger, A. Nonlocal pseudopotential calculations of the electronic properties of relaxed GaAs(110) surface. *Phys. Rev. B* **1980**, *22*, 959–969.

(81) Bergstresser, T. K.; Cohen, M. L. Electronic structure and optical properties of hexagonal CdSe, CdS, and ZnS. *Phys. Rev.* **1967**, *164*, 1069–1080.

(82) Öğüt, S.; Chelikowsky, J. R.; Louie, S. G. Quantum confinement and optical gaps in Si nanocrystals. *Phys. Rev. Lett.* **1997**, *79*, 1770–1773.

(83) Zhou, X. W.; Ward, D. K.; Martin, J. E.; Van Swol, F. B.; Cruz-Campa, J. L.; Zubia, D. Stillinger-Weber potential for the II-VI elements Zn-Cd-Hg-S-Se-Te. *Phys. Rev. B* **2013**, *88*, 085309.

(84) Han, P.; Bester, G. Interatomic potentials for the vibrational properties of III-V semiconductor nanostructures. *Phys. Rev. B* **2011**, *83*, 174304.

(85) Kelley, A. M. Comparison of three empirical force fields for phonon calculations in CdSe quantum dots. *J. Chem. Phys.* **2016**, *144*, 214702.

(86) Grünwald, M.; Lutker, K.; Alivisatos, A. P.; Rabani, E.; Geissler, P. L. Metastability in pressure-induced structural transformations of CdSe/ZnS core/shell nanocrystals. *Nano Lett.* **2013**, *13*, 1367–1372.

(87) Hazarika, A.; Fedin, I.; Hong, L.; Guo, J.; Srivastava, V.; Cho, W.; Coropceanu, I.; Portner, J.; Diroll, B. T.; Philbin, J. P.; Rabani, E.; Klie, R.; Talapin, D. V. Colloidal atomic layer deposition with stationary reactant phases enables precise synthesis of "digital" II-VI nano-heterostructures with exquisite control of confinement and strain. *J. Am. Chem. Soc.* **2019**, *141*, 13487–13496.

(88) Fan, K.; Liao, C.; Xu, R.; Zhang, H.; Cui, Y.; Zhang, J. Effect of shell thickness on electrochemical property of wurtzite CdSe/CdS core/shell nanocrystals. *Chem. Phys. Lett.* **2015**, *633*, 1–5.

(89) Yu, W. W.; Qu, L.; Guo, W.; Peng, X. Experimental determination of the extinction coefficient of CdTe, CdSe, and CdS nanocrystals. *Chem. Mater.* **2003**, *15*, 2854–2860.

(90) Franceschetti, A.; Zunger, A. Direct pseudopotential calculation of exciton Coulomb and exchange energies in semiconductor quantum dots. *Phys. Rev. Lett.* **1997**, *78*, 915–918.

(91) Banin, U.; Cao, Y.; Katz, D.; Millo, O. Identification of atomic-like electronic states in indium arsenide nanocrystal quantum dots. *Nature* **1999**, *400*, 542–544.

(92) Guzelian, A. A.; Banin, U.; Kadavanich, A. V.; Peng, X.; Alivisatos, A. P. Colloidal chemical synthesis and characterization of InAs nanocrystal quantum dots. *Appl. Phys. Lett.* **1996**, *69*, 1432–1434.

(93) Franceschetti, A.; Zunger, A. Pseudopotential calculations of electron and hole addition spectra of InAs, InP, and Si quantum dots. *Phys. Rev. B* **2000**, *62*, 2614–2623.

(94) Eshet, H.; Grünwald, M.; Rabani, E. The electronic structure of CdSe/CdS Core/shell seeded nanorods: Type-I or quasi-type-II? *Nano Lett.* **2013**, *13*, 5880–5885.

(95) Brumberg, A.; Harvey, S. M.; Philbin, J. P.; Diroll, B. T.; Crooker, S. A.; Wasielewski, M. R.; Rabani, E.; Schaller, R. D. Determination of the in-plane exciton radius in 2D CdSe nanoplatelets via magneto-optical spectroscopy. *ACS Nano* **2019**, *13*, 8589–8596.

(96) Hadar, I.; Philbin, J. P.; Panfil, Y. E.; Neyshtadt, S.; Lieberman, I.; Eshet, H.; Lazar, S.; Rabani, E.; Banin, U. Semiconductor seeded nanorods with graded composition exhibiting high quantum-yield, high polarization, and minimal blinking. *Nano Lett.* **2017**, *17*, 2524–2531.

(97) Philbin, J. P.; Brumberg, A.; Diroll, B. T.; Cho, W.; Talapin, D. V.; Schaller, R. D.; Rabani, E. Area and thickness dependence of Auger recombination in nanoplatelets. *J. Chem. Phys.* **2020**, *153*, 054104.

(98) Hemstreet, L. A.; Fong, C. Y.; Cohen, M. L. Calculation of the Band Structure and Optical Constants of Diamond Using the Nonlocal-Pseudopotential Method. *Phys. Rev. B* **1970**, *2*, 2054–2063.

(99) Chelikowsky, J. R.; Cohen, M. L. Nonlocal pseudopotential calculations for the electronic structure of eleven diamond and zinc-blende semiconductors. *Phys. Rev. B* **1976**, *14*, 556–582.

(100) Hamann, D. R.; Schlüter, M.; Chiang, C. Norm-Conserving Pseudopotentials. *Phys. Rev. Lett.* **1979**, *43*, 1494–1497.

(101) Phillips, J. C.; Kleinman, L. New Method for Calculating Wave Functions in Crystals and Molecules. *Phys. Rev.* **1959**, *116*, 287–294.

(102) Weisz, G. Band Structure and Fermi Surface of White Tin. *Phys. Rev.* **1966**, *149*, 504–518.

(103) Kleinman, L.; Bylander, D. M. Efficacious Form for Model Pseudopotentials. *Phys. Rev. Lett.* **1982**, *48*, 1425–1428.

(104) Blöchl, P. E. Generalized separable potentials for electronic-structure calculations. *Phys. Rev. B* **1990**, *41*, 5414–5416.

(105) King-Smith, R. D.; Payne, M. C.; Lin, J. S. Real-space implementation of nonlocal pseudopotentials for first-principles total-energy calculations. *Phys. Rev. B* **1991**, *44*, 13063–13066.

(106) Williamson, A. J.; Zunger, A. Pseudopotential study of electron-hole excitations in colloidal free-standing InAs quantum dots. *Phys. Rev. B* **2000**, *61*, 1978–1991.

(107) Wei, S. H.; Zunger, A. Calculated natural band offsets of all II-VI and III-V semiconductors: Chemical trends and the role of cation *d* orbitals. *Appl. Phys. Lett.* **1998**, *72*, 2011.

(108) Gong, M.; Duan, K.; Li, C. F.; Magri, R.; Narvaez, G. A.; He, L. Electronic structure of self-assembled InAs InP quantum dots: Comparison with self-assembled InAs GaAs quantum dots. *Phys. Rev. B* **2008**, *77*, 045326.

(109) Kovalenko, M. V.; Protesescu, L.; Bodnarchuk, M. I. Properties and potential optoelectronic applications of lead halide perovskite nanocrystals. *Science* **2017**, *358*, 745–750.

(110) Protesescu, L.; Yakunin, S.; Bodnarchuk, M. I.; Krieg, F.; Caputo, R.; Hendon, C. H.; Yang, R. X.; Walsh, A.; Kovalenko, M. V. Nanocrystals of Cesium Lead Halide Perovskites (CsPbX3, X = Cl, Br, and I): Novel Optoelectronic Materials Showing Bright Emission with Wide Color Gamut. *Nano Letters* **2015**, *15*, PMID: 25633588, 3692–3696.

(111) Schmidt, L. C.; Pertegás, A.; González-Carrero, S.; Malinkiewicz, O.; Agouram, S.; Mínguez Espallargas, G.; Bolink, H. J.; Galian, R. E.; Pérez-Prieto, J. Nontemplate Synthesis of CH3NH3PbBr3 Perovskite Nanoparticles. *Journal of the American Chemical Society* **2014**, *136*, PMID: 24387158, 850–853.

(112) Canneson, D.; Shornikova, E. V.; Yakovlev, D. R.; Rogge, T.; Mitioglu, A. A.; Ballottin, M. V.; Christianen, P. C. M.; Lhuillier, E.; Bayer, M.; Biadala, L. Negatively Charged and Dark Excitons in CsPbBr3 Perovskite Nanocrystals Revealed by High Magnetic Fields. *Nano Letters* **2017**, *17*, PMID: 28820601, 6177–6183.

(113) Chen, L.; Li, B.; Zhang, C.; Huang, X.; Wang, X.; Xiao, M. Composition-Dependent Energy Splitting between Bright and Dark Excitons in Lead Halide Perovskite Nanocrystals. *Nano Letters* **2018**, *18*, PMID: 29464960, 2074–2080.

(114) Tamarat, P.; Bodnarchuk, M. I.; Trebbia, J.-B.; Erni, R.; Kovalenko, M. V.; Even, J.; Lounis, B. The ground exciton state of formamidinium lead bromide perovskite nanocrystals is a singlet dark state. *Nature Materials* **2019**, *18*, 717–724.

(115) Xu, K.; Vliem, J. F.; Meijerink, A. Long-Lived Dark Exciton Emission in Mn-Doped CsPbCl3 Perovskite Nanocrystals. *The Journal of Physical Chemistry C* **2019**, *123*, PMID: 30873253, 979–984.

(116) Rossi, D.; Liu, X.; Lee, Y.; Khurana, M.; Puthenpurayil, J.; Kim, K.; Akimov, A. V.; Cheon, J.; Son, D. H. Intense Dark Exciton Emission from Strongly Quantum-Confined CsPbBr3 Nanocrystals. *Nano Letters* **2020**, *20*, 7321–7326.

(117) Rossi, D.; Qiao, T.; Liu, X.; Khurana, M.; Akimov, A. V.; Cheon, J.; Son, D. H. Size-dependent dark exciton properties in cesium lead halide perovskite quantum dots. *The Journal of Chemical Physics* **2020**, *153*, 184703.

(118) Scholes, G. D.; Rumbles, G. Excitons in nanoscale systems. *Nature Materials* **2006**, *5*, 683–696.

(119) Park, Y.; Obliger, A.; Limmer, D. T. Nonlocal screening dictates the radiative lifetimes of excitations in lead halide perovskites. *Nano Letters* **2022**, *22*, 2398–2404.

(120) Park, Y.; Limmer, D. T. Renormalization of excitonic properties by polar phonons. *The Journal of Chemical Physics* **2022**, *157*, 104116.

(121) Schilcher, M. J.; Robinson, P. J.; Abramovitch, D. J.; Tan, L. Z.; Rappe, A. M.; Reichman, D. R.; Egger, D. A. The significance of polarons and dynamic disorder in halide perovskites. *ACS Energy Letters* **2021**, *6*, 2162–2173.

(122) Mayers, M. Z.; Tan, L. Z.; Egger, D. A.; Rappe, A. M.; Reichman, D. R. How Lattice and Charge Fluctuations Control Carrier Dynamics in Halide Perovskites. *Nano Letters* **2018**, *18*, PMID: 30387614, 8041–8046.

(123) Brivio, F.; Butler, K. T.; Walsh, A.; van Schilfgaarde, M. Relativistic quasiparticle self-consistent electronic structure of hybrid halide perovskite photovoltaic absorbers. *Phys. Rev. B* **2014**, *89*, 155204.

(124) Han, Y.; Liang, W.; Lin, X.; Li, Y.; Sun, F.; Zhang, F.; Sercel, P. C.; Wu, K. Lattice distortion inducing exciton splitting and coherent quantum beating in CsPbI3 perovskite quantum dots. *Nature Materials* **2022**, *21*, 1282–1289.

(125) Tamarat, P.; Hou, L.; Trebbia, J.-B.; Swarnkar, A.; Biadala, L.; Louyer, Y.; Bodnarchuk, M. I.; Kovalenko, M. V.; Even, J.; Lounis, B. The dark exciton ground state promotes photon-pair emission in individual perovskite nanocrystals. *Nature Communications* **2020**, *11*, 6001.

(126) Rashba, E. I.; Sheka, V. Symmetry of Energy Bands in Crystals of Wurtzite Type II. Symmetry of Bands with Spin-Orbit Interaction Included. *Fiz. Tverd. Tela: Collected Papers 2* **1959**, 162–76.

(127) Hou, L.; Tamarat, P.; Lounis, B. Revealing the Exciton Fine Structure in Lead Halide Perovskite Nanocrystals. *Nanomaterials* **2021**, *11*, 1058.

(128) Sercel, P. C.; Lyons, J. L.; Bernstein, N.; Efros, A. L. Quasicubic model for metal halide perovskite nanocrystals. *The Journal of Chemical Physics* **2019**, *151*, 234106.

(129) Swift, M. W.; Lyons, J. L.; Efros, A. L.; Sercel, P. C. Rashba exciton in a 2D perovskite quantum dot. *Nanoscale* **2021**, *13*, 16769–16780.

(130) Quarti, C.; Giorgi, G.; Katan, C.; Even, J.; Palummo, M. Exciton Ground State Fine Structure and Excited States Landscape in Layered Halide Perovskites from Combined BSE Simulations and Symmetry Analysis. *Advanced Optical Materials* **2023**, 2202801.

(131) Bischak, C. G.; Lai, M.; Fan, Z.; Lu, D.; David, P.; Dong, D.; Chen, H.; Etman, A. S.; Lei, T.; Sun, J.; Grünwald, M.; Limmer, D. T.; Yang, P.; Ginsberg, N. S. Liquid-like Interfaces Mediate Structural Phase Transitions in Lead Halide Perovskites. *Matter* **2020**, *3*, 534–545.

(132) Quan, L. N.; Park, Y.; Guo, P.; Gao, M.; Jin, J.; Huang, J.; Copper, J. K.; Schwartzberg, A.; Schaller, R.; Limmer, D. T., et al. Vibrational relaxation dynamics in layered perovskite quantum wells. *Proceedings of the National Academy of Sciences* **2021**, *118*, e2104425118.

(133) Limmer, D. T.; Ginsberg, N. S. Photoinduced phase separation in the lead halides is a polaronic effect. *The Journal of chemical physics* **2020**, *152*, 230901.

(134) Thompson, A. P.; Aktulga, H. M.; Berger, R.; Bolintineanu, D. S.; Brown, W. M.; Crozier, P. S.; in 't Veld, P. J.; Kohlmeyer, A.; Moore, S. G.; Nguyen, T. D.; Shan, R.; Stevens, M. J.; Tranchida, J.; Trott, C.; Plimpton, S. J. LAMMPS - a flexible simulation tool for particle-based materials modeling at the atomic, meso, and continuum scales. *Comp. Phys. Comm.* **2022**, *271*, 108171.

(135) Giannozzi, P.; Baroni, S.; Bonini, N.; Calandra, M.; Car, R.; Cavazzoni, C.; Ceresoli, D.; Chiarotti, G. L.; Cococcioni, M.; Dabo, I.; Corso, A. D.; de Gironcoli, S.; Fabris, S.; Fratesi, G.; Gebauer, R.; Gerstmann, U.; Gougoussis, C.; Kokalj, A.; Lazzeri, M.; Martin-Samos, L.; Marzari, N.; Mauri, F.; Mazzarello, R.; Paolini, S.; Pasquarello, A.; Paulatto, L.; Sbraccia, C.; Scandolo, S.; Sclauzero, G.; Seitsonen, A. P.; Smogunov, A.; Umari, P.; Wentzcovitch, R. M. QUANTUM ESPRESSO: a modular and open-source software project for quantum simulations of materials. *Journal of Physics: Condensed Matter* **2009**, *21*, 395502.

(136) Giannozzi, P.; Andreussi, O.; Brumme, T.; Bunau, O.; Nardelli, M. B.; Calandra, M.; Car, R.; Cavazzoni, C.; Ceresoli, D.; Cococcioni, M.; Colonna, N.; Carnimeo, I.; Corso, A. D.; de Gironcoli, S.; Delugas, P.; DiStasio, R. A.; Ferretti, A.; Floris, A.; Fratesi, G.; Fugallo, G.; Gebauer, R.; Gerstmann, U.; Giustino, F.; Gorni, T.; Jia, J.; Kawamura, M.; Ko, H.-Y.; Kokalj, A.; Küçükbenli, E.; Lazzeri, M.; Marsili, M.; Marzari, N.; Mauri, F.; Nguyen, N. L.; Nguyen, H.-V.; Otero-de-la-Roza, A.; Paulatto, L.; Poncé, S.; Rocca, D.; Sabatini, R.; Santra, B.; Schlipf, M.; Seitsonen, A. P.; Smogunov, A.; Timrov, I.; Thonhauser, T.; Umari, P.; Vast, N.; Wu, X.; Baroni, S. Advanced capabilities for materials modelling with Quantum ESPRESSO. *Journal of Physics: Condensed Matter* **2017**, *29*, 465901.

(137) Giannozzi, P.; Baseggio, O.; Bonfà, P.; Brunato, D.; Car, R.; Carnimeo, I.; Cavazzoni, C.; de Gironcoli, S.; Delugas, P.; Ferrari Ruffino, F.; Ferretti, A.; Marzari, N.; Timrov, I.; Urru, A.; Baroni, S. Quantum ESPRESSO toward the exascale. *The Journal of Chemical Physics* **2020**, *152*, 154105.

(138) Zhao, Q.; Hazarika, A.; Schelhas, L. T.; Liu, J.; Gaulding, E. A.; Li, G.; Zhang, M.; Toney, M. F.; Sercel, P. C.; Luther, J. M. Size-Dependent Lattice Structure and Confinement Properties in CsPbI3 Perovskite Nanocrystals: Negative Surface Energy for Stabilization. *ACS Energy Letters* **2020**, *5*, 238–247.

(139) Yang, R. X.; Tan, L. Z. Understanding size dependence of phase stability and band gap in CsPbI3 perovskite nanocrystals. *The Journal of Chemical Physics* **2020**, *152*, 034702.

(140) Kleinman, L.; Bylander, D. M. Efficacious Form for Model Pseudopotentials. *Phys. Rev. Lett.* **1982**, *48*, 1425–1428.

(141) Sutton, R. J.; Filip, M. R.; Haghighirad, A. A.; Sakai, N.; Wenger, B.; Giustino, F.; Snaith, H. J. Cubic or Orthorhombic? Revealing the Crystal Structure of Metastable Black-Phase CsPbI3 by Theory and Experiment. *ACS Energy Letters* **2018**, *3*, 1787–1794.

(142) Cho, Y.; Berkelbach, T. C. Optical Properties of Layered Hybrid Organic–Inorganic Halide Perovskites: A Tight-Binding GW-BSE Study. *The Journal of Physical Chemistry Letters* **2019**, *10*, PMID: 31560556, 6189–6196.

(143) Franceschetti, A.; Wang, L. W.; Fu, H.; Zunger, A. Short-range versus long-range electron-hole exchange interactions in semiconductor quantum dots. *Phys. Rev. B* **1998**, *58*, R13367–R13370.

(144) Qiao, T.; Liu, X.; Rossi, D.; Khurana, M.; Lin, Y.; Wen, J.; Cheon, J.; Akimov, A. V.; Son, D. H. Magnetic Effect of Dopants on Bright and Dark Excitons in Strongly Confined Mn-Doped CsPbI3 Quantum Dots. *Nano Letters* **2021**, *21*, 9543–9550.

(145) Shang, Q.; Kaledin, A. L.; Li, Q.; Lian, T. Size dependent charge separation and recombination in CsPbI3 perovskite quantum dots. *The Journal of Chemical Physics* **2019**, *151*, 074705.

(146) Yao, J.-S.; Ge, J.; Wang, K.-H.; Zhang, G.; Zhu, B.-S.; Chen, C.; Zhang, Q.; Luo, Y.; Yu, S.-H.; Yao, H.-B. Few-Nanometer-Sized α-CsPbI3 Quantum Dots Enabled by Strontium Substitution and Iodide Passivation for Efficient Red-Light Emitting Diodes. *Journal of the American Chemical Society* **2019**, *141*, 2069–2079.

(147) Guvenc, C. M.; Yalcinkaya, Y.; Ozen, S.; Sahin, H.; Demir, M. M. Gd^{3+}-Doped α-CsPbI3 Nanocrystals with Better Phase Stability and Optical Properties. *The Journal of Physical Chemistry C* **2019**, *123*, 24865–24872.

(148) Paul, S.; Samanta, A. Phase-Stable and Highly Luminescent CsPbI3 Perovskite Nanocrystals with Suppressed Photoluminescence Blinking. *The Journal of Physical Chemistry Letters* **2022**, *13*, 5742–5750.

(149) Franceschetti, A.; Zunger, A. Pseudopotential calculations of electron and hole addition spectra of InAs, InP, and Si quantum dots. *Physical Review B* **2000**, *62*, 2614.

(150) Cho, Y.; Berkelbach, T. C. Environmentally sensitive theory of electronic and optical transitions in atomically thin semiconductors. *Physical Review B* **2018**, *97*, 041409.

(151) Yin, C.; Chen, L.; Song, N.; Lv, Y.; Hu, F.; Sun, C.; Yu, W. W.; Zhang, C.; Wang, X.; Zhang, Y.; Xiao, M. Bright-Exciton Fine-Structure Splittings in Single Perovskite Nanocrystals. *Phys. Rev. Lett.* **2017**, *119*, 026401.

(152) Nestoklon, M. O.; Goupalov, S. V.; Dzhioev, R. I.; Ken, O. S.; Korenev, V. L.; Kusrayev, Y. G.; Sapega, V. F.; de Weerd, C.; Gomez, L.; Gregorkiewicz, T.; Lin, J.; Suenaga, K.; Fujiwara, Y.; Matyushkin, L. B.; Yassievich, I. N. Optical orientation and alignment of excitons in ensembles of inorganic perovskite nanocrystals. *Phys. Rev. B* **2018**, *97*, 235304.

(153) Yan, F.; Demir, H. V. LEDs using halide perovskite nanocrystal emitters. *Nanoscale* **2019**, *11*, 11402–11412.

(154) Kang, J.; Wang, L.-W. High Defect Tolerance in Lead Halide Perovskite CsPbBr3. *The Journal of Physical Chemistry Letters* **2017**, *8*, PMID: 28071911, 489–493.

(155) Fu, M.; Tamarat, P.; Huang, H.; Even, J.; Rogach, A. L.; Lounis, B. Neutral and Charged Exciton Fine Structure in Single Lead Halide Perovskite Nanocrystals Revealed by Magneto-optical Spectroscopy. *Nano Letters* **2017**, *17*, 2895–2901.

(156) Ramade, J.; Andriambariarijaona, L. M.; Steinmetz, V.; Goubet, N.; Legrand, L.; Barisien, T.; Bernardot, F.; Testelin, C.; Lhuillier, E.; Bramati, A.; Chamarro, M. Fine structure of excitons and electron–hole exchange energy in polymorphic CsPbBr3 single nanocrystals. *Nanoscale* **2018**, *10*, 6393–6401.

(157) Klimov, V. I. Spectral and dynamical properties of multiexcitons in semiconductor nanocrystals. *Annu. Rev. Phys. Chem.* **2007**, *58*, 635.

(158) Zhu, H.; Yang, Y.; Lian, T. Multiexciton annihilation and dissociation in quantum confined semiconductor nanocrystals. *Acc. Chem. Res.* **2013**, *46*, 1270.

(159) Zhu, H.; Song, N.; Rodríguez-Córdoba, W.; Lian, T. Wave function engineering for efficient extraction of up to nineteen electrons from one CdSe/CdS quasi-type II quantum dot. *J. Am. Chem. Soc.* **2012**, *134*, 4250.

(160) Ben-Shahar, Y.; Philbin, J. P.; Scotognella, F.; Ganzar, L.; Cerullo, G.; Rabani, E.; Banin, U. Charge carrier dynamics in photocatalytic hybrid semiconductor-metal nanorods: crossover from Auger recombination to charge transfer. *Nano Lett.* **2018**, *18*, 5211–5216.

(161) Gao, J.; Kidon, L.; Rabani, E.; Alivisatos, A. P. Ultrahigh hot carrier transient photocurrent in nanocrystal arrays by Auger recombination. *Nano Lett.* **2019**, *19*, 4804.

(162) Young, R. M.; Jensen, S. C.; Edme, K.; Wu, Y.; Krzyaniak, M. D.; Vermeulen, N. A.; Dale, E. J.; Stoddart, J. F.; Weiss, E. A.; Wasielewski, M. R.; Co, D. T. Ultrafast Two-Electron Transfer in a CdS Quantum Dot-Extended-Viologen Cyclophane Complex. *J. Am. Chem. Soc.* **2016**, *138*, 6163.

(163) Matylitsky, V. V.; Dworak, L.; Breus, V. V.; Basche, T.; Wachtveitl, J. Ultrafast Charge Separation in Multiexcited CdSe Quantum Dots Mediated by Adsorbed Electron Acceptors. *J. Am. Chem. Soc.* **2009**, *131*, 2424.

(164) Huang, J.; Huang, Z.; Yang, Y.; Zhu, H.; Lian, T. Multiple Exciton Dissociation in CdSe Quantum Dots by Ultrafast Electron Transfer to Adsorbed Methylene Blue. *J. Am. Chem. Soc.* **2010**, *132*, 4858.

(165) Luo, X.; Liang, G.; Wang, J.; Liu, X.; Wu, K. Picosecond Multi-Hole Transfer and Microsecond Charge-Separated States at the Perovskite Nanocrystal/Tetracene Interface. *Chem. Sci.* **2019**, *10*, 2459.

(166) Olshansky, J. H.; Ding, T. X.; Lee, Y. V.; Leone, S. R.; Alivisatos, A. P. Hole Transfer from Photoexcited Quantum Dots: The Relationship between Driving Force and Rate. *J. Am. Chem. Soc.* **2015**, *137*, 15567–15575.

(167) Aldana, J.; Wang, Y. A.; Peng, X. Photochemical Instability of CdSe Nanocrystals Coated by Hydrophilic Thiols. *J. Am. Chem. Soc.* **2001**, *123*, 8844.

(168) Giansante, C.; Infante, I. Surface traps in colloidal quantum dots: A combined experimental and theoretical perspective. *J. Phys. Chem. Lett.* **2017**, *8*, 5209–5215.

(169) Lian, S.; Weinberg, D. J.; Harris, R. D.; Kodaimati, M. S.; Weiss, E. A. Subpicosecond photoinduced hole transfer from a CdS quantum dot to a molecular acceptor bound through an exciton-delocalizing ligand. *ACS Nano* **2016**, *10*, 6372.

(170) Olshansky, J. H.; Balan, A. D.; Ding, T. X.; Fu, X.; Lee, Y. V.; Alivisatos, A. P. Temperature-dependent hole transfer from photoexcited quantum dots to molecular species: Evidence for trap-mediated transfer. *ACS Nano* **2017**, *11*, 8346.

(171) Tarafder, K.; Surendranath, Y.; Olshansky, J. H.; Alivisatos, A. P.; Wang, L.-W. Hole transfer dynamics from a CdSe/CdS quantum rod to a tethered ferrocene derivative. *J. Am. Chem. Soc.* **2014**, *136*, 5121.

(172) Tyagi, P.; Kambhampati, P. False multiple exciton recombination and multiple exciton generation signals in semiconductor quantum dots arise from surface charge trapping. *J. Chem. Phys.* **2011**, *134*, 094706.

(173) Walsh, B. R.; Saari, J. I.; Krause, M. M.; Nick, R.; Coe-Sullivan, S.; Kambhampati, P. Surface and interface effects on non-radiative exciton recombination and relaxation dynamics in CdSe/Cd,Zn, S nanocrystals. *Chem. Phys.* **2016**, *471*, 11.

(174) He, Y.; Hu, S.; Han, T.; Chen, X.; Yu, Y.; Li, T.; Zhu, W.; Ouyang, G. Suppression of the Auger recombination process in CdSe/CdS core/shell nanocrystals. *ACS Omega* **2019**, *4*, 9198.

(175) Lian, S.; Christensen, J. A.; Kodaimati, M. S.; Rogers, C. R.; Wasielewski, M. R.; Weiss, E. A. Oxidation of a molecule by the biexcitonic state of a CdS quantum dot. *J. Phys. Chem. C* **2019**, *123*, 5923.

(176) Wu, K.; Du, Y.; Tang, H.; Chen, Z.; Lian, T. Efficient extraction of trapped holes from colloidal CdS nanorods. *J. Am. Chem. Soc.* **2015**, *137*, 10224.

(177) Frantsuzov, P.; Kuno, M.; Jankó, B.; Marcus, R. A. Universal emission intermittency in quantum dots, nanorods and nanowires. *Nat. Phys.* **2008**, *4*, 519.

(178) Efros, A. L.; Rosen, M. Random telegraph signal in the photoluminescence intensity of a single quantum dot. *Phys. Rev. Lett.* **1997**, *78*, 1110.

(179) Sitt, A.; Sala, F. D.; Menagen, G.; Banin, U. Multiexciton Engineering in Seeded Core/Shell Nanorods: Transfer from Type-I to Quasi-Type-II Regimes. *Nano Lett.* **2009**, *9*, 3470.

(180) Schnitzenbaumer, K. J.; Labrador, T.; Dukovic, G. Impact of chalcogenide ligands on excited state dynamics in CdSe quantum dots. *J. Phys. Chem. C* **2015**, *119*, 13314.

(181) Plimpton, S. Fast parallel algorithms for short-range molecular dynamics. *J. Comput. Phys.* **1995**, *117*, 1–19.

(182) Klimov, V. I.; Ivanov, S. S. a.; Nanda, J.; Achermann, M.; Bezel, I.; McGuire, J. a. J.; Piryatinski, A. Single-exciton optical gain in semiconductor nanocrystals. *Nature* **2007**, *447*, 441–446.

(183) Klimov, V. I.; McBranch, D. W.; Leatherdale, C. A.; Bawendi, M. G. Electron and hole relaxation pathways in semiconductor quantum dots. *Phys. Rev. B* **1999**, *60*, 13740–13749.

(184) Frenzel, J.; Joswig, J.-O.; Seifert, G. Optical Excitations in Cadmium Sulfide Nanoparticles. *The Journal of Physical Chemistry C* **2007**, *111*, 10761–10770.

(185) Gillespie, D. T. Exact stochastic simulation of coupled chemical reactions. *J. Phys. Chem.* **1977**, *81*, 2340–2361.

(186) McArthur, E. A.; Morris-Cohen, A. J.; Knowles, K. E.; Weiss, E. A. Charge carrier resolved relaxation of the first excitonic state in CdSe quantum dots probed with near-infrared transient absorption spectroscopy. *J. Phys. Chem. B* **2010**, *114*, 14514–14520.

(187) Utterback, J. K.; Hamby, H.; Pearce, O. M.; Eaves, J. D.; Dukovic, G. Trapped-Hole Diffusion in Photoexcited CdSe Nanorods. *J. Phys. Chem. C* **2018**, *122*, 16974.

(188) Utterback, J. K.; Grennell, A. N.; Wilker, M. B.; Pearce, O. M.; Eaves, J. D.; Dukovic, G. Observation of trapped-hole diffusion on the surfaces of CdS nanorods. *Nat. Chem.* **2016**, *8*, 1061–1066.

(189) Lien, D.-H.; Uddin, S. Z.; Yeh, M.; Amani, M.; Kim, H.; Ager, J. W.; Yablonovitch, E.; Javey, A. Electrical suppression of all nonradiative recombination pathways in monolayer semiconductors. *Science* **2019**, *364*, 468–471.

(190) Wang, H.; Zhang, C.; Rana, F. Ultrafast Dynamics of Defect-Assisted Electron–Hole Recombination in Monolayer MoS2. *Nano Letters* **2015**, *15*, 339–345.

(191) Splendiani, A.; Sun, L.; Zhang, Y.; Li, T.; Kim, J.; Chim, C.-Y.; Galli, G.; Wang, F. Emerging Photoluminescence in Monolayer MoS2. *Nano Letters* **2010**, *10*, 1271–1275.

(192) Qiao, J.; Kong, X.; Hu, Z.-X.; Yang, F.; Ji, W. High-mobility transport anisotropy and linear dichroism in few-layer black phosphorus. *Nature Communications* **2014**, *5*, 4475.

(193) Tran, V.; Soklaski, R.; Liang, Y.; Yang, L. Layer-controlled band gap and anisotropic excitons in few-layer black phosphorus. *Phys. Rev. B* **2014**, *89*, 235319.

(194) Kim, H.; Uddin, S. Z.; Lien, D.-H.; Yeh, M.; Azar, N. S.; Balendhran, S.; Kim, T.; Gupta, N.; Rho, Y.; Grigoropoulos, C. P.; Crozier, K. B.; Javey, A. Actively variable-spectrum optoelectronics with black phosphorus. *Nature* **2021**, *596*, 232–237.

(195) Engel, M.; Steiner, M.; Avouris, P. Black Phosphorus Photodetector for Multispectral, High-Resolution Imaging. *Nano Letters* **2014**, *14*, 6414–6417.

(196) Youngblood, N.; Chen, C.; Koester, S. J.; Li, M. Waveguide-integrated black phosphorus photodetector with high responsivity and low dark current. *Nature Photonics* **2015**, *9*, 247–252.

(197) Chen, X.; Lu, X.; Deng, B.; Sinai, O.; Shao, Y.; Li, C.; Yuan, S.; Tran, V.; Watanabe, K.; Taniguchi, T.; Naveh, D.; Yang, L.; Xia, F. Widely tunable black phosphorus mid-infrared photodetector. *Nature Communications* **2017**, *8*, 1672.

(198) Yuan, H.; Liu, X.; Afshinmanesh, F.; Li, W.; Xu, G.; Sun, J.; Lian, B.; Curto, A. G.; Ye, G.; Hikita, Y.; Shen, Z.; Zhang, S.-C.; Chen, X.; Brongersma, M.; Hwang, H. Y.; Cui, Y. Polarization-sensitive broadband photodetector using a black phosphorus vertical p–n junction. *Nature Nanotechnology* **2015**, *10*, 707–713.

(199) Kim, H.; Uddin, S. Z.; Higashitarumizu, N.; Rabani, E.; Javey, A. Inhibited non-radiative decay at all exciton densities in monolayer semiconductors. *Science* **2021**, *373*, 448–452.

(200) Yablonovitch, E.; Allara, D. L.; Chang, C. C.; Gmitter, T.; Bright, T. B. Unusually Low Surface-Recombination Velocity on Silicon and Germanium Surfaces. *Phys. Rev. Lett.* **1986**, *57*, 249–252.

(201) Yang, J.; Xu, R.; Pei, J.; Myint, Y. W.; Wang, F.; Wang, Z.; Zhang, S.; Yu, Z.; Lu, Y. Optical tuning of exciton and trion emissions in monolayer phosphorene. *Light: Science & Applications* **2015**, *4*, e312–e312.

(202) Ge, S.; Li, C.; Zhang, Z.; Zhang, C.; Zhang, Y.; Qiu, J.; Wang, Q.; Liu, J.; Jia, S.; Feng, J.; Sun, D. Dynamical Evolution of Anisotropic Response in Black Phosphorus under Ultrafast Photoexcitation. *Nano Letters* **2015**, *15*, 4650–4656.

(203) Perdew, J. P.; Burke, K.; Ernzerhof, M. Generalized Gradient Approximation Made Simple. *Phys. Rev. Lett.* **1996**, *77*, 3865–3868.

(204) Grimme, S.; Hansen, A.; Brandenburg, J. G.; Bannwarth, C. Dispersion-Corrected Mean-Field Electronic Structure Methods. *Chemical Reviews* **2016**, *116*, 5105–5154.

(205) Ziletti, A.; Carvalho, A.; Campbell, D. K.; Coker, D. F.; Castro Neto, A. H. Oxygen Defects in Phosphorene. *Phys. Rev. Lett.* **2015**, *114*, 046801.

(206) Hamann, D. R. Optimized norm-conserving Vanderbilt pseudopotentials. *Phys. Rev. B* **2013**, *88*, 085117.

(207) van Setten, M.; Giantomassi, M.; Bousquet, E.; Verstraete, M.; Hamann, D.; Gonze, X.; Rignanese, G.-M. The PseudoDojo: Training and grading a 85 element optimized norm-conserving pseudopotential table. *Computer Physics Communications* **2018**, *226*, 39–54.

(208) Monkhorst, H. J.; Pack, J. D. Special points for Brillouin-zone integrations. *Phys. Rev. B* **1976**, *13*, 5188–5192.

(209) Blöchl, P. E.; Jepsen, O.; Andersen, O. K. Improved tetrahedron method for Brillouin-zone integrations. *Phys. Rev. B* **1994**, *49*, 16223–16233.

(210) Ziletti, A.; Carvalho, A.; Trevisanutto, P. E.; Campbell, D. K.; Coker, D. F.; Castro Neto, A. H. Phosphorene oxides: Bandgap engineering of phosphorene by oxidation. *Phys. Rev. B* **2015**, *91*, 085407.

(211) Cleveland, J. P.; Anczykowski, B.; Schmid, A. E.; Elings, V. B. Energy dissipation in tapping-mode atomic force microscopy. *Applied Physics Letters* **1998**, *72*, 2613–2615.

(212) Wood, J. D.; Wells, S. A.; Jariwala, D.; Chen, K.-S.; Cho, E.; Sangwan, V. K.; Liu, X.; Lauhon, L. J.; Marks, T. J.; Hersam, M. C. Effective Passivation of Exfoliated Black Phosphorus Transistors against Ambient Degradation. *Nano Letters* **2014**, *14*, 6964–6970.

(213) Pei, J.; Gai, X.; Yang, J.; Wang, X.; Yu, Z.; Choi, D.-Y.; Luther-Davies, B.; Lu, Y. Producing air-stable monolayers of phosphorene and their defect engineering. *Nature Communications* **2016**, *7*, 10450.